

The Structure of ^{33}Si , ^{35}S and the magicity of the $N = 20$ gap at $Z = 14, 16$

by

Sandile Jongile

*Dissertation presented for the degree of Doctor of Philosophy in Physics in the Faculty
of Science at Stellenbosch University*

Department of Physics,
University of Stellenbosch,
Private Bag XI, Matieland 7602,
South Africa.



Supervisor(s) :

Prof M. Wiedeking, *Dept. of Subatomic Physics iThemba LABS, School of Physics
University of Witwatersrand.*

Prof S. Wyngaart, *Dept. of Physics, University of Stellenbosch*

Dr. O. Sorlin, *Grand Accélérateur National d'Ions Lourds (GANIL)*

Dr. A. Lemasson, *Grand Accélérateur National d'Ions Lourds (GANIL)*

Prof P. Papka, *Dept. of Physics, University of Stellenbosch*

**This work is based on the research supported in part by the National
Research Foundation of South Africa**

December 2021

Declaration

By submitting this dissertation electronically, I declare that the entirety of the work contained therein is my own, original work, that I am the sole author thereof (save to the extent explicitly otherwise stated), that reproduction and publication thereof by Stellenbosch University will not infringe any third party rights and that I have not previously in its entirety or in part submitted it for obtaining any qualification.

December 2021

Copyright © 2021 Stellenbosch University
All rights reserved

Abstract

Nuclei along $N = 20$ provide an excellent region to investigate nuclear structure and interactions, with their evolution from the doubly magic nucleus ^{40}Ca through the $Z = 16$ and $Z = 14$ nuclei ^{36}S and ^{34}Si , respectively, to ^{32}Mg with a deformed $2p - 2h$ intruder ground state.

This study is motivated by and focuses on:

i) The robustness of the $N = 20$ shell gap from ^{40}Ca (studied previously by Matoba *et al.*, [1]) to ^{36}S and ^{34}Si , after removing 4 and 6 protons, respectively. A strong sd -shell closure would lead to a fully occupied neutron $d_{3/2}$ orbital and no, or little occupancy, neutrons in the $p_{3/2}$ and $f_{7/2}$ orbitals located above $N = 20$. With the deformed ^{32}Mg having only 2 protons removed from ^{34}Si it is an interesting question if the magicity is somewhat gradually or abruptly eroded below $Z = 14$.

ii) A significant reduction of the neutron $1d_{5/2}$ and $1d_{3/2}$ spin-orbit splitting between ^{40}Ca and ^{36}S , as protons are removed from the $1d_{3/2}$ orbital, would be indicative of the effect of proton-neutron tensor force. By comparing the neutron $1d_{5/2}$ hole strength between these nuclei, the strength of the tensor force can be probed in an unprecedented manner.

Two separate studies were carried out to address the aforementioned motivations. Firstly, an inverse kinematics experiment with the ${}^9\text{Be}({}^{34}\text{Si}, {}^{33}\text{Si} + \gamma)\text{X}$ and ${}^9\text{Be}({}^{36}\text{S}, {}^{35}\text{S} + \gamma)\text{X}$ reactions which was performed at the National Superconducting Cyclotron Laboratory (NSCL) with 98.5 MeV/u ${}^{34}\text{Si}$ and 88 MeV/u ${}^{36}\text{S}$ secondary beams produced in the fragmentation of a ${}^{48}\text{Ca}$ primary beam has been reanalysed. Reaction products were detected with the Gamma-Ray Energy Tracking In-beam Nuclear Array (GRETINA) coupled to the S800 magnetic spectrometer. This measurement focused on probing the Fermi surface in ${}^{34}\text{Si}$ and ${}^{36}\text{S}$, and locating the strength of the neutron $d_{5/2}$ orbital. From the spectroscopic factor values, which are derived from observed γ -ray decays, the neutron $1d_{3/2}$ appears to be fully occupied, while some fraction of the $1d_{5/2}$ orbital is observed only as the states lie above the neutron emission energy threshold.

Secondly, the ${}^{36}\text{S}(p, d){}^{35}\text{S}$ reaction is a useful tool to probe the change in neutron spin-orbit splitting between ${}^{34}\text{Si}$ and ${}^{36}\text{S}$. The ${}^{36}\text{S}(p, d){}^{35}\text{S}$ reaction allows for an investigation into the ${}^{36}\text{S}$ Fermi surface stiffness and the neutron $d_{3/2} - d_{5/2}$ spin-orbit reduction. It also serves to probe the magicity of ${}^{36}\text{S}$ through its Fermi surface, complementary to the (d, p) reaction previously performed, reported in Ref. [2]. Of course all this depends on the availability of a reliable ${}^{36}\text{S}$ target. This was achieved by specifically developing a new target system at iThemba LABS which allows for a cost effective ${}^{36}\text{S}$ target without heavy contaminants to be used. This novel target, which is in motion and encapsulates sulfur between two Mylar foils, has been shown to be an effective way to produce targets with a significant amount of material (0.5-1 mg/cm²) [3]. Using the developed moving ${}^{36}\text{S}$ target system with 66 MeV incident protons, states in ${}^{35}\text{S}$ were populated and studied with the K600 magnetic spectrometer at iThemba LABS. States up to 9 MeV are observed, identifying the neutron single-particle strength below and above the Fermi surface using the detection of the deuterons at the focal plane of the K600 spectrometer with an energy resolution of approximately FWHM = 30 keV in the center of mass.

Opsomming

Kerne in die $N = 20$ isotoon bied vrugbare grond vir kernstruktuur en kernreaksie studies aangesien dit toegang verleen tot 'n verskeidenheid van verskynsels, vanaf die ^{40}Ca kern met tower getalle vir beide protone en neutrone, die $Z = 16$ ^{36}S en die $Z = 14$ ^{34}Si kerne tot by ^{32}Mg met sy vervormde $2p - 2h$ indringer grondtoestand.

In hierdie studie word daar op die volgende aspekte gefokus:

i) Die karakter van die $N = 20$ skilmodel gaping met verandering van proton getal vanaf ^{40}Ca (vantevore bestudeer deur Matoba *et al.*) tot by ^{36}S en ^{34}Si , soos wat 4 en 6 protone respektiewelik verwyder word uit die kern. In die geval van 'n robuuste sd -skil afsluiting moet die neutron $d_{3/2}$ orbitaal heeltemal gevul wees, en behoort die $p_{3/2}$ en $f_{7/2}$ orbitale bokant $N = 20$ feitlike leeg te wees. Aangesien die vervormde ^{32}Mg kern verskil van ^{34}Si slegs deur die verwydering van twee protone, sal dit interessant wees om vas te stel of die verandering in voorkeurgetal eienskappe van die kern geleidelik of skielik verander benewens $Z = 14$.

ii) 'n Beduidende verlaging van die neutron $1d_{5/2}$ en $1d_{3/2}$ spinbaan splyting in ^{36}S in vergelyking met die ^{40}Ca kern, soos wat protone verwyder word uit die $1d_{3/2}$ orbitaal, kan dui op die impak van die proton-neutron tensor wisselwerking. Inligting aangaande die

sterkte van die tensor wisselwerking kan verkry word deur vergelykings te maak tussen die neutron $1d_{5/2}$ holte sterkte van hierdie kerne.

Twee onafhanklike experimente is onderneem ten einde bogenoemde aspekte te ondersoek. Eerstens is die $^{34}\text{Si}(-1n)^{33}\text{Si}$ en $^{36}\text{S}(-1n)^{35}\text{S}$ reaksies eksperimenteel ondersoek by die National Superconducting Cyclotron Laboratory (NSCL). In hierdie inverse kinematiese metings was die 98.5 MeV/u ^{34}Si en 88 MeV/u ^{36}S sekondêre bundels verkry deur die fragmentasie van 'n primêre ^{48}Ca bundel, waarna reaksieprodukte waargeneem is met behulp van die Gamma-Ray Energy Tracking In-beam Nuclear Array (GRETINA) tesame die S800 magnetiese spektrometer. Hierdie meting het ten doel gehad om die Fermi oppervlakte van die ^{34}Si en ^{36}S kerne te ondersoek, en om vas te stel wat die posisie van die neutron $d_{5/2}$ orbitaal is. Met behulp van die geassosieerde spektroskopiese faktore, soos bepaal deur middel van metings van γ verval met GRETINA, is dit bepaal dat die neutron $1d_{3/2}$ orbitaal volledig gevul is. Verder is ook vasgestel dat slegs 'n gedeelte van die $1d_{5/2}$ orbitaal waargeneem, aangesien die toestand geleë is bokant die neutron emissie drempel.

Tweedens is $^{36}\text{S}(p,d)^{35}\text{S}$ reaksie benut om die verandering in die spinbaan splyting tussen ^{34}Si en ^{36}S te ondersoek. Hierdie reaksie kan verder gebruik word om die ^{36}S Fermi oppervlak styfheid te ondersoek, asook die voorkeurgetal karakter van ^{36}S , komplementê tot die resultate van die (d,p) reaksie wat vantevore ondersoek is. Vanselfsprekend kan hierdie ondersoek slegs gedoen word indien 'n betroubare ^{36}S teiken beskikbaar is. 'n Nuwe, unieke en koste effektiewe teiken meganisme is ontwerp by iThemba LABS spesifiek vir die doel van hierdie studie. Hierdie bewegende teiken bestaan uit twee Mylar foelies wat die swaai omhul, en het die voordeel dat dit geen swaar kerne as kontaminante bevat nie. Dit is verder bewys dat hierdie proses suksesvol gebruik kan word om swaai teikens te maak wat 0.5-1 mg/cm² dik is. So 'n bewegende ^{36}S teiken was gebruik tesame met 'n 66 MeV proton bundel om kerntoestande in ^{35}S te ondersoek met behulp van die K600 magnetiese spektrometer by iThemba LABS. Tydens die eksperiment is deutrone

waargeneem in die fokale vlak van die spektrometer met energie resolusie van die meting ongeveer 30 keV (FWHM). Opgewekte toestande tot en met 9 MeV is waargeneem, wat dit moontlik maak om neutron enkeleeltjie sterkte aan beide kante van die Fermi oppervlakte te ondersoek.

Acknowledgements

Vulnerability is not winning or losing,
it's having the courage to show up
when you cannot control the outcome.

Brene Brown

It goes without saying that there is quite a number of people who have offered a helping hand during the course of this project. I clearly have failed to mention everyone, but let it be noted I am truly grateful.

Firstly, I would like to express my most sincere gratitude to my supervisors Dr O. Sorlin, Dr A. Lemasson, Prof M Wiedeking, Prof P. Papka and Prof S Wyngaart. I am grateful for all the insightful comments and knowledge of physics I have received from you. I am aware of the level of experience and superior physics knowledge you have acquired over the years, but despite that you have been willing to accept my input as equally important. To Dr O Sorlin thank you for investing so much time and effort in ensuring I produce quality results. I am particularly very grateful for the great deal of physics knowledge you have taught me and the passion you have for physics which is indeed inspiring. To Prof M. Wiedeking, I am grateful for your support, guidance and constantly “putting out fires” whenever required. I am aware it was not always easy to work with me but you

remained supportive. I am very grateful to Dr A Lemasson for his patience in teaching me the technical skills required for the data analysis. You were very patient with me particularly in helping me master the GRETINA-S800 data analysis as well as ROOT. To Prof P Papka who always had a solution for everything and played a huge role in developing the ^{36}S target system, I am highly appreciative of your help. I am deeply humbled and feel privileged to have worked with such supportive supervisors.

A special mention has to go to Dr R. Neveling from iThemba LABS, for the enormous support with the K600 data analysis and being very understanding. I have learnt a lot from you and hope in future I can help people the way you do. You played the role of a supervisor in so many different aspects.

I would like to thank Freddy Flavingy, Nicholas Keely and Vittorio Soma for performing the theoretical calculations required for the analysis of the K600 data.

Not forgetting to mention Dr. L. Donaldson and Dr P Adsley for always offering a helping hand with the data analysis. I am also grateful for your constant “check ups” to make sure I was doing alright.

To the students and physicists that took part in the GRETINA-S800 experiment and the iThemba experiment, your help was very much appreciated.

I would like to thank my father Mr H. Jongile, for always believing in me and offering words of encouragement. You have supported me emotionally and financially and I hope this work makes you proud. To my mother thank you for your strength and kindness this is for you as well. To my siblings Thamsanqa, Mmeli, Vuyelwa and Nomalanga, thank you for all your love and support that carried me through challenging times. I am grateful to Fhumulani Nemulodi for the unwavering support, I could not have made it through some challenging times without your support. To my best friend, Zenzele

Ndlovu, we both embarked on a PhD journey almost at the same time. You have carried me through trying times and I am sincerely grateful.

I am thankful to the National Research Foundation of South Africa (NRF) for the financial assistance that helped make this project a success.

Contents

List of Figures	xiv
List of Tables	xxiii
I PART I: Introduction and Motivations	2
1 Introduction	3
1.1 The nucleon-nucleon interaction	4
1.1.1 One-pion exchange potential	5
1.1.2 Components of the nucleon-nucleon interaction	7
1.2 Physics Motivations	8
1.2.1 Shell evolution due to tensor force	8
1.2.2 Fermi surface as a probe to characterize magicity	12
2 Theoretical background	15
2.1 Theoretical cross-sections	15
2.2 Momentum distributions	18
2.3 Spectroscopic factors	19
3 Reaction Model: Transfer Reactions	22
3.1 Shell Model	23

Contents	xi
3.2 Scattering Theory	25
3.2.1 Distorted Wave Born Approximation (DWBA)	29
II PART II: The GRETINA-S800 $^{34}\text{Si}, ^{36}\text{S}(-1n)$ knockout Experiment and Results	31
4 Experimental Details: the $^{34}\text{Si}, ^{36}\text{S}(-1n)$ knockout reactions	32
4.1 Radioactive Beam Production	33
4.2 The S800 spectrograph	35
4.3 Particle identification	37
4.3.1 Incoming and transmitted residue identification	37
4.4 Momentum reconstruction	38
4.5 The Gamma-Ray Energy Tracking In-beam Nuclear Array (GRETINA)	39
4.5.1 Principle of operation	40
4.5.2 Signal Decomposition and γ -ray Tracking	42
5 Analysis	44
5.0.1 Particle identification	44
5.1 Relative γ -ray efficiency	45
5.2 Nearest-neighbor addback procedure	48
5.3 Energy resolution	50
5.4 Population fraction	54
5.5 Inclusive Cross section	54
5.5.1 Least squares fit of parallel momentum distributions	55
6 Results and Interpretation	57
6.1 $^9\text{Be}(^{34}\text{Si}, ^{33}\text{Si}+\gamma)\text{X}$	57
6.1.1 Inclusive cross sections to all bound states	57
6.1.2 Number of incident nuclei	58
6.1.3 Level scheme	59

Contents	xii
6.1.4 Evaluation of least squares in fitting theoretical distributions . . .	66
6.1.5 Spectroscopic Factors	68
6.2 ${}^9\text{Be}({}^{36}\text{S}, {}^{35}\text{S}+\gamma)\text{X}$	69
6.2.1 Inclusive Cross section	69
6.2.2 Level Scheme	71
6.2.3 Momentum distributions	71
III PART III: The iThemba LABS ${}^{36}\text{S}(\text{p},\text{d})$ Experiment	78
7 Experimental Details	79
7.1 Beam Production	79
7.2 K600 magnetic spectrometer Overview	81
7.2.1 Focal Plane Detector Packages	83
7.3 ${}^{36}\text{S}$ Target	84
7.3.1 Production of ${}^{36}\text{S}$ targets	86
7.3.2 Method of Production	86
7.3.3 Elastic backscattering spectrometry (EBS) characterization	88
7.3.4 ${}^{36}\text{S}$ target in K600 scattering chamber.	90
8 Analysis	94
8.1 Focal-Plane Particle Identification	94
8.2 VDC operation	96
8.3 Calculation of Focal Plane Coordinates	97
8.4 Horizontal Angle Calibration	103
8.5 Improving energy resolution	104
8.6 Energy Calibration	106
8.7 Differential Cross section	110
8.7.1 Target thickness normalization	113

Contents	xiii
9 Results	117
9.1 Identification of ^{35}S states	117
9.2 Cross section extraction	121
9.3 j^π assignments	126
9.4 $^{40}\text{Ca}(p,d)^{39}\text{Ca}$ Analysis	143
10 Discussion	147
10.1 Single hole states in ^{39}Ca	147
10.2 Single hole states in ^{35}S populated from the $^{36}\text{S}(p,d)$ reaction	149
10.3 Shell evolution in the $N = 19$ isotones	153
10.3.1 Comparison between the $(-1n)$ knockout and (p,d) transfer reactions.	154
10.4 Ab-initio calculations	156
10.5 $N=20$ Fermi surfaces	160
10.5.1 Fermi surface analysis from the $^{34}\text{Si},^{36}\text{S}(-1n)$ knockout reactions . .	160
10.5.1.1 Rigidity of $N=20$ shell gap	162
10.5.2 Fermi surface analysis from the $^{36}\text{S}, ^{40}\text{Ca}(p,d)$ reactions	164
11 Conclusion	166
Appendices	169
A Publications stemming from this study	170
A.1 Peer Reviewed Journal	170
A.2 Conference proceeding	170
Bibliography	171

List of Figures

1.1	Schematic illustration of the nucleon-nucleon interaction as a result of pion exchange.	5
1.2	Three examples of the nucleon-nucleon interaction as a result of meson exchange, figure adapted from [12].	6
1.3	Schematic illustration of the monopole part of the tensor interaction as neutrons are added to the $f_{7/2}$ orbit. The ESPEs are affected accordingly depending on whether the tensor force is attractive (red wavy line) or repulsive (purple wavy line).	9
1.4	Evolution of the reduced spin-orbit splitting as a function of mass number derived from Ref. [18] and taken from [19]. The formula $2\frac{\Delta_{SO}}{2\ell+1}$ represents the reduced spin orbit splitting and n is the number of nodes. As can be seen from the systematic, the experimental data (solid circles) for the ^{133}Sn , and ^{131}Sn Refs [20, 21, 22] agrees well with the theoretical prediction represented by the curve. The first observed deviation is seen from the change in spin-orbit splitting in ^{35}Si as indicated by the arrow [2].	11
1.5	Various Channels available for study and some published already from the GRETINA-S800 experiment performed for the PhD of Mutschler <i>et al.</i> , [23].	12

1.6	Fermi surface plots indicating the occupation probability of neutrons in the valence shells of ^{48}Ca and ^{40}Ca [25, 26].	14
2.1	Illustration from Ref [32] containing a compilation of data from different knockout reactions, indicating the dependence of reduction factors R_s on the binding energy.	21
3.1	Quantum mechanical illustration of scattering [40].	28
4.1	Schematic representation of the layout of the K500, K1200 cyclotrons and the S800 spectrometer adapted from [45]. (a) is the time-of-flight (TOF) setup to measure mass. (b) Shows the photo-multiplier and scintillators used for TOF measurements providing stop and start signals at the A1900 fragment separator and S800 focal plane. (c) Shows the setup for the rigidity measurement at the target position of the S800, where the green arrows indicates the beam after fragmentation.	35
4.2	S800 focal plane showing the two CRDCs, ion chamber and scintillators [47].	37
4.3	Schematic illustration of the S800 Spectrograph showing different sections in the analysis line and spectrograph [23].	38
4.4	GRETINA array, showing ten detector modules (40 crystals) mounted in a close-packed configuration. In this work only 7 modules were used 4 being at forward angles with respect to the beam axis at 58° and 3 were placed at 90° [50].	40
4.5	A schematic view of one GRETINA module [49].	41
4.6	Schematic representation indicating the segmentation in a GRETINA module, the two types of crystals (A and B) are shown [49].	41
5.1	Incoming beam identification using time of flight between the OBJ and XFP scintillators for the (-1n) knockout setting from ^{34}Si beam shown in 5.1a and for ^{36}S beam shown in 5.1b.	46

5.2	Particle identification plots to identify the knockout residues for the 1n settings. The TOF depends on the ratio of mass of the knockout residues to charge A/q while the energy loss depends on the nucleus's atomic charge Z^2 . Using this principle the knockout residues can be separated and have a definite loci as shown in the plot above where the colors indicate the intensity on a logarithmic scale. The highest intensity loci corresponds to the knockout residue of interest.	46
5.3	Relative efficiencies as a function of energy using a ^{152}Eu radioactive source for addback and non-addback mode. Intensities were obtained relative to the 778 keV γ -ray.	49
5.4	Comparison of addback (red) to non-addback (blue) spectra using in-beam data for ^{33}Si	49
5.5	addback curve including in-beam points from ^{33}Si , ^{35}P (obtained from [23] and ^{152}Eu calibration data.	51
5.6	Schematic representation of the addback performed in detector crystals.	51
6.1	Add-back, Doppler corrected spectra showing γ -rays observed in this work for ^{33}Si . The 931 keV transition is observed in coincidence with the 1724 keV transition (see inset.)	59
6.2	Level scheme for ^{33}Si from this work constructed using $\gamma\gamma$ coincidences and add-back spectra where the width of the arrows is proportional to the γ -ray intensity(which were normalized to the 1010 keV transition), b_f is the population fraction and spins and parity assignments are as suggested by Ref. [64]. The transitions marked in black originate from the removal of a neutron from the occupied sd - or the pf -shell valence orbits. Transitions shown in red connect higher-spin states, obviously requiring another reaction mechanism not yet identified.	61

6.3	γ -ray gated spectra to show coincidences observed between the 971 keV and 1010 keV transitions. The gating transitions are indicated in red in the figures.	62
6.4	Experimental parallel momentum distributions for ^{33}Si determined by gating on γ -rays with fits from theoretical calculations using different L values. The horizontal arrow shows the range in which the fit was considered.	64
6.5	PID plot for identifying the incoming beam and indicating the repetitions seen for the ^{36}S beam and (-1n) setting.	70
6.6	Particle identification plots to identify the incoming beam and knockout residues for the $^{36}\text{S}(-1n)$ settings. This plot shows the selection for the ^{35}P incoming beam and ^{34}P knockout residue	71
6.7	Add-back, Doppler corrected spectra showing γ -rays observed in this work for ^{35}S	72
6.8	Level scheme for ^{35}S from this work. The blue transition represents the 1990 keV isomer, the transitions in black correspond to states which have corresponding parallel momentum distributions while the red transitions correspond states where it was not possible to extract parallel momentum distributions due to low statistics.	73
6.9	Experimental parallel momentum distributions for ^{35}S determined by gating of γ -rays as indicated in the panels. Fits from theoretical calculations using different ℓ values are shown as solid lines.	75
6.10	Ground state experimental distribution fitted with the $\ell = 2$, 18 % of $\ell = 3$ 1990 keV and a combination of both theoretical predictions (18% + 82%).	76
6.11	Evaluation of best contribution (corresponding to the lowest χ^2 value) compatible for the $\ell = 3$, 1990 keV isomer state to the final ground state parallel momentum distribution.	77
7.1	Schematic layout of the SSC facility at iThemba LABS.	80

7.2	Schematic layout of the K600 magnetic spectrometer. It should be noted that for the current experiment the external beam stop was not used. . . .	81
7.3	Illustration of the X and U wire plane wires in a VDC detectors at the K600 focal plane [76].	84
7.4	Target ladder used in the experiment with respective positions occupied by the indicated targets.	85
7.5	Target frame holding the encapsulated enriched ^{36}S	88
7.6	Technical drawing of the two-axis swiveling system to uniformly expose the target to the 3 MeV proton beam and hence energy deposition. The beam traverses the chamber from left to right. The sides and blanking flanges of the vacuum chamber are removed from the 3D drawing for viewing purposes.	91
7.7	Scaler plot obtained for backscattered protons measured with energy between 2.45-2.65 MeV. The accumulated time is 4 hours at $I_b = 6 \text{ nA}$, $E_b = 3 \text{ MeV}$. The arrows indicate when the target is swiveling within the region comprising Mylar-Sulfur and Mylar only areas. The target positions are selected when high Sulfur spots are found.	92
7.8	Implementation of the designed moving target system in the K600 spectrometer scattering chamber during the experiment.	93
8.1	Particle identification spectrum of energy loss in the scintillator as a function of the relative TOF for the $^{36}\text{S}(p,d)$ reaction for data collected at $\theta_{lab} = 7^\circ$. There is a broad range of deuteron energies as a result of the deuterons having different incident energies (due to varying target thickness) in the scintillator resulting in different light output, see Figure 8.2.	95
8.2	The light output in the scintillator depends on the energy of the incident deuterons in the scintillator. Their pulse heights are registered for different states produced in ^{35}S that appear at different focal plane position.	96

8.3	Schematic illustration of deuteron particles passing the wire plane in a VDC. The drift direction of the electrons towards the signal wires is shown. See text for details.	98
8.4	A typical drift time spectrum obtained using a white tune spectrum. Each time pin corresponds to 100 ps.	99
8.5	The lookup table used in the conversion of drift time to drift length. The true drifttime is calculated as: $\text{drifttime}(\text{in ns}) = -0.1 * x + 500$. The vertical axis value of 1000 represents 8mm.	100
8.6	Converted TDC signals to corresponding drift length.	100
8.7	A sample selection showing the focal plane coordinates X_{fp} (mm), θ_{fp} (degrees) and Y_{fp} (mm) for the $^{36}\text{S}(\text{p,d})$ reaction.	101
8.8	Technical drawing of the multihole pepperpot collimator used in the calibration of θ_{scat} . The collimator is positioned in a collimator carousel situated in front of the quadrupole as shown in Figure 7.2.	103
8.9	Two-dimensional histogram indicating θ_{scat} as a function of X_{fp} before (top) and after (bottom) calibration using the pepperpot.	105
8.10	Lineshape Correction implementation to factor out dependence of θ_{scat} and Y_{fp} on X_{fp}	106
8.11	Focal position spectrum showing the resolution improvement. The blue (uncorrected) spectrum peak resolution corresponds to $\sigma = 1.4$ mm and the red (corrected) spectrum has a peak resolution of $\sigma = 1.2$ mm	107
8.12	Focal position spectrum indicating the states were used for the energy calibration.	107
8.13	Second order polynomial fit of the rigidity as a function of the focal plane position X_{fp} for the measurement of the $^{36}\text{S}(\text{p,d})$ reaction at $\theta_{lab} = 7^\circ$	109
8.14	Excitation energy as a function of the runtime for one run. The red arrows indicate examples of regions where the beam is either on only Mylar foils or a region with only a small amount of ^{36}S	114

8.15	Spectra used to select regions where count rate was at maximum where (a) represents the counts for the groundstate (GS) as a function of time, (b) Is the CI corrected spectra obtained by dividing the spectrum in panel (a) by the spectrum in panel (c). The spectrum in panel (c) represents the CI counts as a function of time. These regions are indicated in green and are associated with the maximum target thickness.	115
9.1	Excitation energy spectra for the $^{36}\text{S}(p,d)^{35}\text{S}$ reaction for the data col- lected at all K600 angle settings i.e $\theta_{lab} = 4^\circ, 7^\circ, 10^\circ, 15^\circ, 21^\circ$ and 28° . In the black is the data collected at higher field setting and in blue is the data collected at lower field settings.	118
9.2	Excitation energy spectra representing data collected at one K600 angle $\theta = 10^\circ$ for the different 4 angle cuts made for each angle $[-1.8^\circ:-0.9^\circ]$, $[-0.9^\circ:-0^\circ]$, $[0^\circ:0.9^\circ]$ and $[0.9^\circ:1.8^\circ]$	119
9.3	Spectrum representing states identified from a (p,d) reaction on Mylar (shown in red) and compared to the $^{nat}\text{S}(p,d)$ spectrum (black).	120
9.4	The excitation energy spectrum for the $^{36}\text{S}(p,d)^{35}\text{S}$ reaction (blue line) at 7° together with results of the ^{nat}S target (filled green peaks) whereby the $^{33,32,31}\text{S}$ states (in magenta) are scaled relative to ^{35}S peaks using the reported isotopic content.	122
9.5	Spectrum indicating the high energy tail seen in the peak shape of all states.	122
9.6	Excitation energy spectrum (blue histogram) for the angle region 13.65° - 16.35° , showing the total fit (black line) as well as the fit to the individual peaks and background (red line).	124
9.7	Excitation energy fit range for one peak 50 keV below the peak centroid, to 150 keV above the peak centroid. The green arrows represent the lower limit, centroid and upper limit in the range of the fit considered.	125

9.8	Angular distributions for the first five excited states with well known ℓ and j assignments. The (small) error bars, often smaller than the size of the data points, of the experimental cross sections reflect both systematic uncertainties (energy, normalization) and statistical errors.	132
9.9	Comparison between some $d_{5/2}$ and $d_{3/2}$ states in ^{35}S , indicating the difference in angular pattern of the angular distributions as a result of a j dependence.	133
9.10	A sample selection of typical expected angular distribution shapes for the different ℓ values as calculated for ^{39}Ca and ^{35}S	134
9.11	Angular distributions for $\ell=0$ ($s_{1/2}$) transferred angular momentum. . . .	137
9.12	Angular distributions for $\ell=1$ ($p_{3/2}$) transferred angular momentum. . . .	138
9.13	Angular distributions for $\ell=1$ ($p_{1/2}$) transferred angular momentum. . . .	139
9.14	Angular distributions for $\ell=2$ ($d_{3/2}$) transferred angular momentum. . . .	140
9.15	Angular distributions for $\ell=2$ ($d_{5/2}$) transferred angular momentum. . . .	141
9.16	Angular distributions for $\ell=3$ ($f_{7/2}$) transferred angular momentum. . . .	142
9.17	Experimental angular distributions superimposed with DWBA calculations from this work for different states in ^{39}Ca in the range $E_x=0-6$ MeV. Experimental data was obtained from Ref. [1].	144
9.18	Experimental angular distributions superimposed with DWBA calculations from this work for different states in ^{39}Ca in the range $E_x=6-8.7$ MeV. Experimental data was obtained from Ref. [1].	145
9.19	Comparison between some $d_{5/2}$ and $d_{3/2}$ states in ^{39}Ca , indicating the difference in angular character of the angular distributions as a result of a j dependence.	146

10.1	The sudden reduction of the neutron $2p_{3/2} - p_{1/2}$ spin-orbit splitting between ^{37}S and ^{35}Si , as protons are removed from the $2s_{1/2}$ orbital. The triangles represent the differences in energy between the $\frac{1}{2}^-$ and $\frac{3}{2}^-$ states having the largest C^2S value. The open circles were obtained by Kay et al., [96] who determined the differences of centroids obtained from transfer data.	157
10.2	Illustration of the distribution of the $d_{5/2}$ hole strength in ^{35}S (red) and ^{39}Ca (black) as a function of excitation energy.	158
10.3	Predictions of the evolution of the $d_{5/2} - d_{3/2}$ splitting using ab-initio Gorkov Self-Consistent Green's functions [92]. The different fragmentation of the $d_{5/2}$ orbit is shown and the horizontal bars are indicative of the magnitude of the C^2S values.	159
10.4	Fermi surface plot for neutron shells indicating occupation probabilities as a function of binding energies. From above: 1) Using combined data from the current work $^{34}\text{Si}(-1n)$ reaction with the $^{34}\text{Si}(d, p)$ reaction Ref. [2], 2) current work $^{36}\text{S}(-1n)$ reaction with the $^{36}\text{S}(d, p)$ reaction Ref. [2]	163
10.5	Fermi surface of ^{36}S neutrons (left) and ^{40}Ca neutrons (right). The data indicated in blue is from (p, d) reactions while the data indicated in red is from the (d, p) reaction. A general uncertainty (not shown) of 20% was assumed as explained in subsection 10.5.1.1.	165

List of Tables

3.1	Lippmann-Schwinger equations including the two potential formula [39]. . .	30
5.1	Energies for photopeaks, number of emitted γ -rays per decay (relative intensities) and associated errors used from the ^{152}Eu source in relative efficiency calibration. The data used as reference was taken from Ref. [54].	47
6.1	Energy, spin (j) and parity (π), population fraction b_f , single particle cross sections σ_{sp} and partial cross sections of final states populated in the $^{34}\text{Si}(-1n)^{33}\text{Si}$ reaction together with spectroscopic factors C^2S_{exp} deduced from the present work and as quoted by [66].	67
6.2	Energy, spin(j) and parity (π), population fraction b_f , single particle cross sections σ_{sp} and partial cross sections of final states populated in the $^{36}\text{S}(-1n)^{35}\text{S}$ reaction.	74
7.1	Isotopic Distribution	86
7.2	Chemical admixtures	87
8.1	Rigidity calibration parameters for each angle setting.	109
8.2	Normalization factors	116
9.1	Gaussian and Landau parameters obtained from fitting the first five excited states and used in fitting the remaining states above 2.938 MeV. . .	123

9.2	Identification of states	127
9.3	Details of the theoretical calculations.	130
9.4	Comparison in C^2S values between previous study by Ref. [1] and the values obtained using the new set of theoretical angular distributions.	143
10.1	Summed C^2S , C^2S weighted mean energy and the binding energy $\langle \epsilon_j \rangle$ values in ^{39}Ca	148
10.2	Spectroscopic factors and comparison between results from the $^{36}\text{S}(-1n)^{35}\text{S}$ and $^{36}\text{S}(p, d)^{35}\text{S}$ reactions. Blank entries indicate the absence of data. The uncertainties in the C^2S values for the (p, d) reaction only include the error in the target thickness and the statistical contribution. The systematic error associated with the choice of optical model is not included.	150
10.3	Summed C^2S , C^2S weighted mean energy and the binding energy $\langle \epsilon_j \rangle$ values in ^{35}S . The $p_{1/2}$ orbit was not included despite the fact that some $p_{1/2}$ strength is being observed, because of the need to maintain consistency with the analysis of the study of Matoba <i>et al.</i> , [1], whereby the $p_{1/2}$ orbit was excluded in the normalization.	153
10.4	Neutron occupations for the positive-parity orbitals obtained from the $^{34}\text{Si}(-1n)^{33}\text{Si}$ and $^{36}\text{S}(-1n)^{35}\text{S}$ reactions.	160
10.5	$^{34}\text{Si}(d, p)^{35}\text{Si}$ and $^{36}\text{S}(d, p)^{37}\text{S}$ reaction data obtained from Ref. [2].	161
10.6	Neutron occupations for the negative-parity orbitals obtained from the $^{34}\text{Si}(-1n)^{33}\text{Si}$ and $^{36}\text{S}(-1n)^{35}\text{S}$ reactions.	161

Part I

PART I: Introduction and Motivations

1 | Introduction

An atomic nucleus is a many-body Fermionic quantum system made of neutrons and protons (collectively termed nucleons). The atomic nucleus was discovered by Rutherford in 1911 [4], who proposed that most of the atom's mass ($\approx 99.9\%$) is concentrated inside the nucleus which is positively charged. Soon after, the neutron was discovered by Chadwick [5] resulting in a more complete picture of the nucleus. The nucleons are confined in the nucleus by the strong force within a region of a few fm.

One essential goal of nuclear physics is to understand the nature and effects of the fundamental nucleon-nucleon interaction. This is done by solving the many-body problem. An important step in solving the many-body problem is the choice of interaction introduced. Because the nucleon-nucleon interaction is not fully understood, several approaches have been employed over the past years. These are the phenomenological effective interaction, realistic interaction and effective field theory.

Once a suitable interaction is chosen, then in principle it is possible to solve the Schrödinger equation, which describes the dynamics of the many-body system. It has been proven a challenging task to solve the Schrödinger equation without making use of some approximations. Several microscopic approaches have been employed such as ab-initio [6], shell model [7] and self-consistent mean field [8]. They all have shortcomings and perform

better or worse depending on the application. For instance, for the purposes of modeling the evolution of nuclear structure across the nuclear chart, it is more appropriate to use the self-consistent mean field calculations. This is because they use effective energy density functionals whereby the parameters are adjusted phenomenologically to reproduce many average nuclear properties such as the total energy per nucleon and nuclear incompressibility [9].

This dissertation is organized into three parts: Part I, Chapter 1 gives an introduction to the nucleon-nucleon interaction, and the physics motivations behind the study. In Part I, Chapter 2 and 3, the reaction theory relevant to the ^{34}Si , $^{36}\text{S}(-1n)$ and $^{36}\text{S}(p,d)$ reactions is discussed. In Part II, and III the different experimental techniques used in performing the knockout reactions and transfer reaction respectively are outlined, together with the obtained results. A global discussion of the results from both experiments is detailed in Chapter 10 and concluding remarks are made in Chapter 11.

1.1 The nucleon-nucleon interaction

In order to have a quantitative description of the nucleus it is necessary to review the theoretical background on the underlying nature of the nuclear force and its variety of phenomenological features. The strong force has been studied using nucleon-nucleon (NN) scattering at different energies. Both protons and neutrons are made up of three quarks, the proton is composed of two up quarks and one down quark (uud) while the neutron has one up quark and two down quarks (udd). Because the nuclear force saturates after a certain range it was proposed that it is due to the exchange of particles with mass (π -mesons) [10] as illustrated in Figure 1.1.

The force was first described as short range by Yukawa *et al.*, [10] in 1935. He pointed

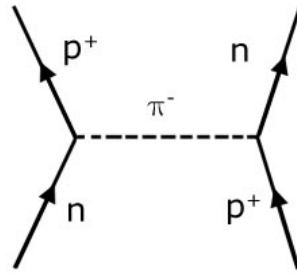


Figure 1.1: Schematic illustration of the nucleon-nucleon interaction as a result of pion exchange.

out that the short range nature of the force is due to the exchange of a particle with mass, analogous to the Coulomb (electromagnetic) force which is a result of the exchange of a mass-less particle (the photon). The Yukawa potential is represented by [10]:

$$V(r) = g^2 \frac{e^{-\lambda r}}{r}, \quad (1.1)$$

where r is the range, g represents a coupling constant, λ is a constant corresponding to the inverse of the range of the nuclear forces and $\lambda = \frac{h}{mc}$ where m is the mass of the particle, h is Planck's constant and c is the velocity of light .

1.1.1 One-pion exchange potential

An illustration of the nucleon-nucleon potential is shown in Figure 1.2, where at distances of $r \geq 2$ fm the force describes the static one-pion-exchange processes. The medium-range part corresponding to $1 \text{ fm} \leq r \leq 2 \text{ fm}$ is attributed to the non-static part of the pion exchange where there is an exchange of the heavier mesons (ρ, σ, ω). At distances of less than ≈ 0.9 fm the potential becomes strongly repulsive [11].

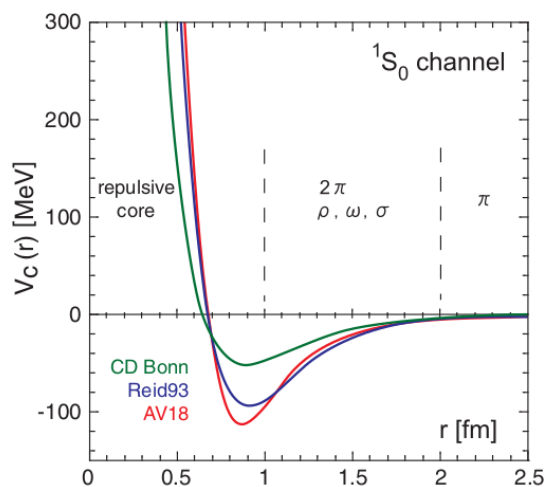


Figure 1.2: Three examples of the nucleon-nucleon interaction as a result of meson exchange, figure adapted from [12].

Pions (π -mesons) were first discovered in 1947 by Powell *et al.*, [13] and they exist in three charge states: (π^- , π^0 , π^+). Within the framework of pseudo-scalar theory [14] i.e. pions are ($J^\pi = 0^-$) isovector ($T = 1$) particles, the potential due to pion exchange, the so called “one-pion-exchange-potential” [15]:

$$V_{OPEP}(r) = 0.33m_\pi c^2 \frac{g^2}{4\pi\hbar c} (\tau_1\tau_2) [(\sigma_1\sigma_2) + S_{12}f(r)] \frac{e^{-\frac{r}{\lambda}}}{r\lambda}, \quad (1.2)$$

where m_π is the mass of the pion, S_{12} represents the tensor operator, $\frac{1}{\lambda} = \frac{m_\pi c}{\hbar}$, $f(r)$ represents the pion coupling, τ_1 and τ_2 are the spin matrices for nucleon 1 and 2 respectively, while σ_1 and σ_2 , are the isospin matrices.

1.1.2 Components of the nucleon-nucleon interaction

Some basic concepts on the NN interaction are discussed to facilitate the presentation of the physics motivation. The NN interaction can be categorized into “central” and “non-central” components:

$$V = V_C(1, 2) + V_{\ell s}(1, 2) + V_T(1, 2), \quad (1.3)$$

where V_C is the central component, $V_{\ell s}$ is the spin-orbit interaction and V_T is the tensor interaction. The central part can be further dissolved into four terms using the spin-isospin representation [9]:

$$V_C = V_o(r) + V_\sigma(r)\vec{\sigma}_1 \cdot \vec{\sigma}_2 + V_\tau(r)\vec{\tau}_1 \cdot \vec{\tau}_2 + V_{\sigma\tau}(r)\vec{\sigma}_1 \cdot \vec{\sigma}_2 \vec{\tau}_1 \cdot \vec{\tau}_2, \quad (1.4)$$

where $r = |\vec{r}_1 + \vec{r}_2|$ represents the distance between the two nucleons, σ and τ represent the spin and isospin respectively.

The non-central interaction consists of two terms [9]:

- The two-body spin-orbit interaction:

$$V_{\ell s}(1, 2) = (V_{\ell s}^{is}(r) + V_{\ell s}^{iv}(r)\vec{\tau}_1 \cdot \vec{\tau}_2)\vec{\ell} \cdot \vec{s}, \quad (1.5)$$

where ℓ is the relative orbital angular momentum between the two interacting nucleons, s is the total intrinsic spin where $\vec{s} = \frac{1}{2}(\sigma_1 + \sigma_2)$. The superscripts is and iv represent the isoscalar ($\Delta T = \tau_1 + \tau_2 = 0$) and isovector ($\Delta T = |\tau_1 - \tau_2| = 1$)

parts of the potential. The isoscalar part refers to the part of the potential making no distinction between protons and neutrons because the densities are summed, while the isovector part of the potential does differentiate between the two (i.e. densities are subtracted).

- The tensor component is defined by:

$$V_T(1, 2) = (V_T^{is}(r) + V_T^{iv}(r)\vec{\tau}_1 \cdot \vec{\tau}_2)S_{12}(r), \quad (1.6)$$

where $S_{12}(r)$ is the tensor operator:

$$S_{12}(r) = \frac{3}{r^2}(\vec{\sigma}_1 \cdot \vec{r})(\vec{\sigma}_2 \cdot \vec{r}) - \vec{\sigma}_1 \cdot \vec{\sigma}_2. \quad (1.7)$$

1.2 Physics Motivations

1.2.1 Shell evolution due to tensor force

It has been postulated [16] that the observed change in shell structure is due to the spin-isospin dependent part of the nucleon-nucleon interaction (i.e. monopole effect of the tensor force). The effective single-particle energy (ESPE) of a given orbital j is sensitive to the monopole part of the tensor force thereby highlighting the effect of the mean field emanating from the surrounding nucleons acting on one nucleon. For a given ℓ value, an orbit can have two possible values of j : $j_> = \ell + \frac{1}{2}$ or $j_< = \ell - \frac{1}{2}$, where $j_>$ and $j_<$ are spin-orbit partners. The S_{12} operator couples more strongly spin-orbit partners ($j_<, j_>$) or ($j_>, j_<$) as compared to other combinations ($j_<, j_<$), ($j_>, j_>$). An example is shown in Figure 1.3, indicating the splitting of the proton $\pi d_{3/2}$ and $\pi d_{5/2}$ orbitals with neutrons in the $\nu f_{7/2}$. The monopole part of the tensor force is attractive between the $\pi d_{3/2}$ and $\nu f_{7/2}$ orbitals and repulsive for the $\pi d_{5/2}$ and $\nu f_{7/2}$. This results in a shift

of the single-particle energies accordingly (either raised or lowered) as shown in Figure 1.3. However, the monopole part of the tensor force can be repulsive, inducing a more modest gain in binding energy as compared to an orbital that is exposed to an attractive tensor component.

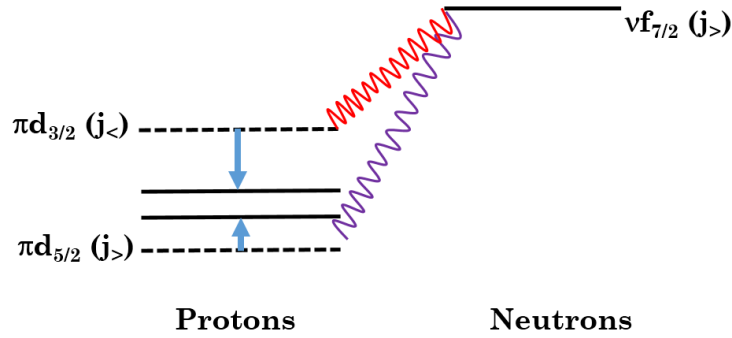


Figure 1.3: Schematic illustration of the monopole part of the tensor interaction as neutrons are added to the $f_{7/2}$ orbit. The ESPEs are affected accordingly depending on whether the tensor force is attractive (red wavy line) or repulsive (purple wavy line).

The single-particle energy of a given orbital j is a result of its kinetic energy and the closed shell effects on the orbital [17]. Adding nucleons to different orbitals may change the binding energy of a given orbital, as compared to the adjacent ones. The corresponding tensor monopole interaction is given by [17]:

$$V_{j^\pi j^\nu}^T = \frac{\sum_J (2J+1) \langle j^\pi j^\nu | \widehat{V} | j^\pi j^\nu \rangle_{JT}}{\sum_J (2J+1)}, \quad (1.8)$$

where $\langle j^\pi j^\nu | \widehat{V} | j^\pi j^\nu \rangle_{JT}$ refers to the diagonal matrix element for 2 nucleons coupled to angular momentum J and isospin T . Subsequent filling of nucleons in the j^ν orbital results in a change in single-particle energy of the j^π orbital. Given that neutrons are in

the j^ν orbital while protons are in the j^π orbital, then as per equation 1.8 single-particle energies are changed according to the monopole effect as follows [17]:

$$\Delta\epsilon_\pi(j^\pi) = \frac{1}{2}V_{j^\pi j^\nu}^{T=0} + V_{j^\pi j^\nu}^{T=1}n_\nu(j^\nu), \quad (1.9)$$

where n_ν is the neutron number in the j^ν orbit and ϵ_π is the effective single-particle energy of the j^π orbital.

The monopole part of the tensor interaction $V_{j^\pi j^\nu}^T$ between nucleons is attractive for nucleons with non-aligned intrinsic spins ($j^\pi_>, j^\nu_<$) and repulsive for nucleons with aligned intrinsic spins ($j^\pi_>, j^\nu_>$). In addition a proton in the j^π orbital will affect the energies of neutrons in the j^ν orbital. However, the $T = 0$ is significantly more attractive than the $T = 1$ term [17].

Indeed the shell evolution is caused by a subtle combination of several components of the nuclear force [17], however in this study the focus is in singling out the effect of the tensor force. Most mean field and relativistic mean field models predict a decrease in sin-orbit splitting with increasing mass [18] as shown in Figure 1.4.

In the framework of the mean field and relativistic mean field models, the magnitude of the spin orbit force has been attributed to be solely due to the spin orbit force [18]. Assuming a variation from the spin-orbit force only, a decrease of the $1d$ spin orbit (SO) splitting by about 460 keV is expected between ^{35}S and ^{39}Ca (as shown from the trend of Figure 1.4). It is the aim of this work to the evolution of the neutron $d_{3/2} - d_{5/2}$ spin-orbit splitting from ^{39}Ca to ^{35}S . If a deviation to this trend is observed, this could be due to the tensor force. In order to study such an effect I have studied the $^{36}\text{S}(p, d)^{35}\text{S}$ experiment. An important quantity in interpreting the results is the spectroscopic factors, of which the analysis involved in extracting the values is detailed in Chapter 9 and 10

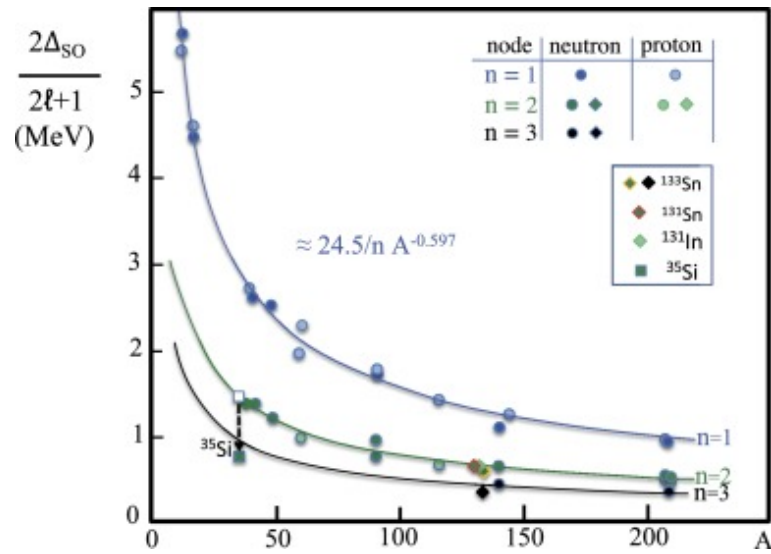


Figure 1.4: Evolution of the reduced spin-orbit splitting as a function of mass number derived from Ref. [18] and taken from [19]. The formula $2\frac{\Delta_{SO}}{2\ell+1}$ represents the reduced spin orbit splitting and n is the number of nodes. As can be seen from the systematic, the experimental data (solid circles) for the ^{133}Sn , and ^{131}Sn Refs [20, 21, 22] agrees well with the theoretical prediction represented by the curve. The first observed deviation is seen from the change in spin-orbit splitting in ^{35}Si as indicated by the arrow [2].

1.2.2 Fermi surface as a probe to characterize magicity

The second aim of this project is to classify the diffuseness of the Fermi surface in ^{34}Si and ^{36}S compared to ^{40}Ca . The intention is to find out if neutrons undergo pair excitations across the $N = 20$ shell gap, and if so how the situation compares to ^{40}Ca . To address the second physics motivation data from a neutron knockout experiment on ^{36}S and ^{34}Si was partially re-analysed from an experiment already performed previously by Mutschler *et al.*, [23]. In this present work, the data was partially and more carefully re-analysed for the purposes of publishing the $(-1n)$ knockout reaction channels in a peer-reviewed journal. In addition Figure 1.5 shows the data available from the MSU experiment performed for the PhD project of Mutschler *et al.*, [23] together with the analysed and published reaction channels as well as those which have not yet been published.

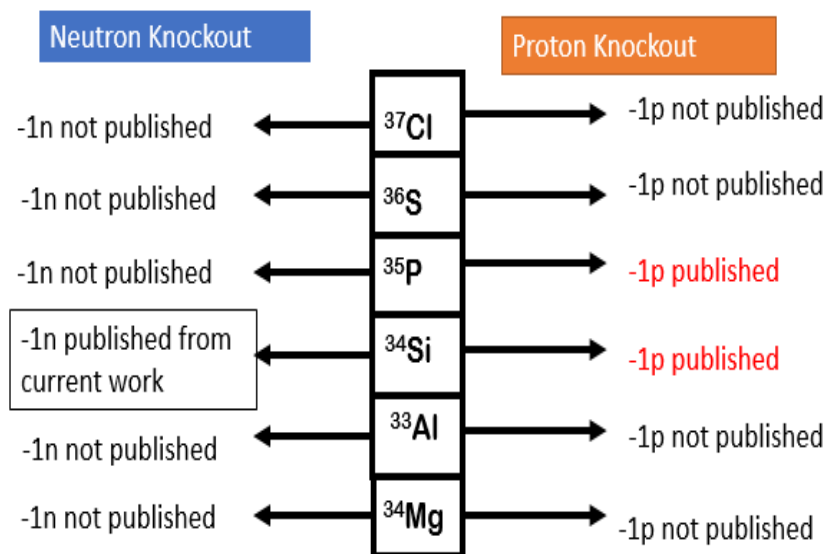


Figure 1.5: Various Channels available for study and some published already from the GREYINA-S800 experiment performed for the PhD of Mutschler *et al.*, [23].

From this study the resulting reanalysis of the $^9\text{Be}(^{34}\text{Si}, ^{33}\text{Si}+\gamma)\text{X}$ has been published. Certain analysis procedures were not repeated namely calibration of particle identifi-

cation detectors, extraction of efficiency values for particle detectors, beam purity and transmission values. The unfolding of data (converting of raw data into ROOT [24] calibrated trees), particle identification, extracting of scaler events to determine incoming and outgoing number of nuclei and the γ -ray analysis was repeated in this study. In Chapter 5 a detailed description is given of the analysis done by this study and that taken from the previous study. It should be noted that the Fermi surface plots were extracted as well for the $^{36}\text{S}(p, d)^{35}\text{S}$ reaction and ^{40}Ca data analysis from Matoba *et al.*, [1].

One-nucleon transfer or knockout reactions are often used to infer information pertaining to the Fermi surface of a nucleus. The Fermi surface of a nucleus can be used to characterize its magicity, which is how much it behaves like a magic nucleus. If a particular nucleus is extremely double magic, then what is expected is a very sharp Fermi surface. This is a situation whereby there are filled orbitals below the Fermi surface and no particles above the Fermi surface. In an occupation plot as a function of the binding energy, the occupancy of the valence orbital should be one and thereafter the occupation value should immediately drop to zero as shown by the dotted line in Figure 1.6. However this is not always the case because the nucleus is a correlated system of nucleons continuously interacting. It is possible and often happens that there are nucleons making pair excitations across a shell or shell gap which results in a diffuse Fermi surface. A classic example found in ^{40}Ca as shown in Figure 1.6. In ^{40}Ca there are neutrons undergoing pair excitations from the $\ell = 2, d_{3/2}$ orbit to upper orbits which are $\ell = 3, f_{7/2}$ and $\ell = 1, p_{3/2}$. The occupancy of the $\ell = 2$ orbit is reduced to the benefit of the upper orbits.

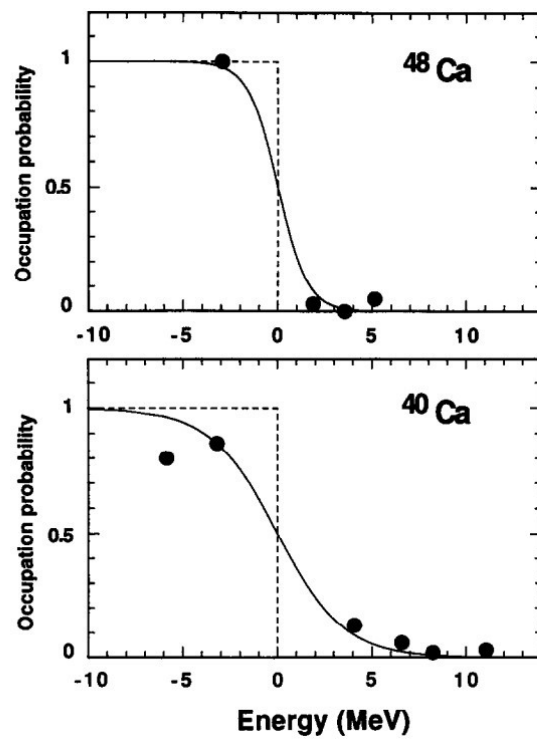


Figure 1.6: Fermi surface plots indicating the occupation probability of neutrons in the valence shells of ^{48}Ca and ^{40}Ca [25, 26].

2 | Theoretical background

This chapter discusses the different theoretical aspects of nuclear structure that are most relevant to this study. In addition, some different mean field approaches that have been used in understanding the evolving shell structure are discussed. The background theory on determining theoretical cross-sections, momentum distributions and spectroscopic factors is reviewed because these will be compared with experimentally determined counterparts are in Chapter 6.

2.1 Theoretical cross-sections

The total cross-section $\sigma(c)$ for populating a core state c can be separated into two parts: the single-particle cross section and the spectroscopic factor. It can be written in the form [27]:

$$\sigma(nlj) = \sum_j C^2S(nlj)\sigma_{sp}(S_n, nlj), \quad (2.1)$$

where C^2S represents the spectroscopic factor, (nlj) are the radial quantum number,

orbital angular momentum and j is the total angular momentum respectively. The symbol σ_{sp} represents the single-particle cross section and is equal to the probability of removing a single nucleon from a given orbit with j in the initial nucleus, resulting in a final state in the $A - 1$ nucleus. The term S_n is the neutron separation energy. The value σ_{sp} is highly dependent on the neutron separation energy S_n and on the angular momenta and excitation energy of the removed nucleon or added nucleon. The single-particle cross section can be broken down into three parts; stripping (σ_{str}), diffraction (σ_{diff}) and Coulomb (σ_{Cou}) [27]:

$$\sigma_{sp} = \sigma_{str} + \sigma_{diff} + \sigma_{Cou}, \quad (2.2)$$

The Coulomb term is usually negligible for light targets and hence it is not considered. The stripping mechanism involves the valence nucleon being absorbed and only interacting at most inelastically with the target. Here the nucleon is scattered at large angles leaving the target in an excited state. The cross section associated with this mechanism is [27]:

$$\sigma_{str} = \frac{1}{2I + 1} \int d\mathbf{b} \sum_M \langle \psi_{IM}^c | (1 - |S_n|^2) |S_c|^2 | \psi_{IM}^c \rangle, \quad (2.3)$$

where I is the angular momentum of projectile, \mathbf{b} is the core-target impact parameter, M is the magnetic number which contains all possible sub-states and ψ_{IM}^c refers to the core-removed nucleon wave function [27]. S_c and S_n are S matrices and they represent the probability of scattering the core elastically and absorption of the nucleon inelastically, respectively.

The diffractive (elastic breakup) refers to the process whereby the target remains in the

ground state while the removed nucleon is emitted in a forward direction. The diffractive cross section is more complex and is composed of two processes: 1) diffraction by the absorptive part and refraction as a result of the real part of the potential. The two terms add coherently to give [27]:

$$\sigma_{diff} = \frac{1}{2I+1} \int d\mathbf{k} \int d\mathbf{b} \sum_{M\sigma\mu} |\langle \psi_{\sigma\mu}^{(-)}(c, \mathbf{k}) | (S_n S_c) | \psi_{IM}^c \rangle|^2, \quad (2.4)$$

where \mathbf{k} is the relative wave-number, and the integral is over all final states of the core and nucleon with asymptotic spin projections μ and σ .

In the presence of a potential, the parameter σ_{diff} is the probability that for the outgoing channel both the valence nucleon and core, have been excited into a continuum state. Therefore it becomes [27]:

$$\sigma_{diff} = \frac{1}{2I+1} \int d\mathbf{b} \left[\sum_M \langle \psi_{IM}^c | |S_n S_c|^2 | \psi_{IM}^c \rangle - \sum_{iMM'} |\langle \psi_{M'M'}^2(i) | S_n S_c | \psi_{IM}^c \rangle|^2 \right], \quad (2.5)$$

where $i \equiv (nljI)$ represents all bound states. If the initial and final states in 2.4 are orthogonal then the equation above can be further simplified by making the substitution of $S_n S_c$ with $1 - S_n S_c$, without changing the value [27]. This form of the equation gives the single-particle cross section i.e. the probability of both the core and target surviving, excluding the creation of a final bound state.

Often by applying the following approximation, the integral over the breakup states can be discarded [27]:

$$\sum_{\sigma\mu} \int d\mathbf{k} |\psi_{\sigma\mu}^{(\pm)}(c, \mathbf{k})\rangle \langle \psi_{\sigma\mu}^{(\pm)}(c, \mathbf{k})| = 1 - \sum_{M'i} |\psi_{I'M'}^c\rangle \langle \psi_{I'M'}^c(i)|, \quad (2.6)$$

to give:

$$\sigma_{diff} = \frac{1}{2I+1} \int d\mathbf{b} \left[\sum_M \langle \psi_{IM}^c || S_n S_c|^2 | \psi_{IM}^c \rangle - |\langle \psi_{I'M'}^c(i) | S_n S_c | \psi_{IM}^c \rangle|^2 \right]. \quad (2.7)$$

2.2 Momentum distributions

A crucial source of information is deduced from the momentum distribution of the knockout residue. In the framework of the ‘‘sudden approximation’’ [28], the momentum of the knockout residue that recoils with a certain momentum p is equal but opposite in sign to the momentum of the removed nucleon. In this work, the parallel momentum distributions are deduced, and despite the fact that both projections contain the same information, parallel distributions are less sensitive to Coulomb diffraction and hence are easier to obtain [29].

The theoretical momentum distributions are obtained using the MOMDIS code [30] within the eikonal framework. The expression used to compute the distributions for the case of a stripping reaction is:

$$\frac{d\sigma_{str}}{d\mathbf{k}_z^c} = \frac{1}{2J+1} \sum_M \int d^2\mathbf{b}_\nu (1 - |S_n|^2) \int d^2\rho |S_c|^2 \left| \int dz \frac{e^{-ik_z^c z}}{2\pi} \psi_{IM}^c(\rho, z) \right|^2, \quad (2.8)$$

where \mathbf{k}_z represents the longitudinal component of \mathbf{k} , \mathbf{b}_ν is the impact parameter of the

valence nucleon, S_c and S_n are core-target and nucleon-target eikonal S matrices. The integration spans over all space with $(\vec{\rho}, z)$ being the vector between the valence-particle and the core.

2.3 Spectroscopic factors

From a theoretical point of view the spectroscopic factor is defined as the radial overlap between a nucleus with A nucleons in an initial state $|\psi_i^A\rangle$ and the final nucleus $|\psi_f^{A\pm 1}\rangle$ [31]. A stripping reaction refers to the transfer of nucleons from the projectile to the target, while for pickup reactions nucleons are transferred from the target to the projectile. For a stripping or pickup reaction it can be defined as [31]:

$$S_j^{str} = \frac{1}{2I+1} |\langle \psi_i^A | a_k^\dagger | \psi_f^{A-1} \rangle|^2, \quad (2.9)$$

$$S_j^{pick} = \frac{1}{2I+1} |\langle \psi_i^A | a_k | \psi_f^{A+1} \rangle|^2, \quad (2.10)$$

where a_k^\dagger , a_k are the creation and annihilation operators, respectively, ψ^A , $\psi^{A\pm 1}$ are the wave-functions of the incoming and outgoing nuclei. If the wave function is normalized to 1, then the spectroscopic factor is equal to 1 for the removal of a nucleon from a pure single particle state and the spectroscopic factor is equal to $2I+1$ for the removal of a nucleon from a fully occupied orbit.

It must be noted that the spectroscopic factor is not an experimental observable. Nevertheless the spectroscopic factors are extracted from cross sections. A center of mass

correction is applied if the spectroscopic factors are computed using a harmonic oscillator basis [31].

Depending on whether the reaction is stripping or pickup the corrections are:

$$C_{str} = \left(\frac{A}{A+1} \right)^N, \quad (2.11)$$

$$C_{pick} = \left(\frac{A}{A-1} \right)^N, \quad (2.12)$$

where $N = n + \ell$ and is the principal quantum number of the major oscillator shell.

In nuclei the separation energy serves as an indicator or upper limit for the cut off for bound excited states. A part of the spectroscopic factor strength is dependent on the neutron and proton separation energies. This is more evident in exotic nuclei with uneven neutron to proton numbers as the nucleon separation energies decrease towards the driplines. The systematics for the increasing body of reactions indicate a trend in R_s , the ratio of experimental (σ_{exp}) to theoretical inclusive cross sections (σ_{th}):

$$R_s = \frac{\sigma_{exp}}{\sigma_{th}}. \quad (2.13)$$

The suppressions indicate that the shell models used, plus the reaction model, overestimate the cross section (spectroscopic strength) leading to bound final states. Such a systematic reduction in spectroscopic strength has been reported in Ref. [32] illustrated in Figure 2.1, from shell predictions in studies of electron-induced proton knockout reactions.

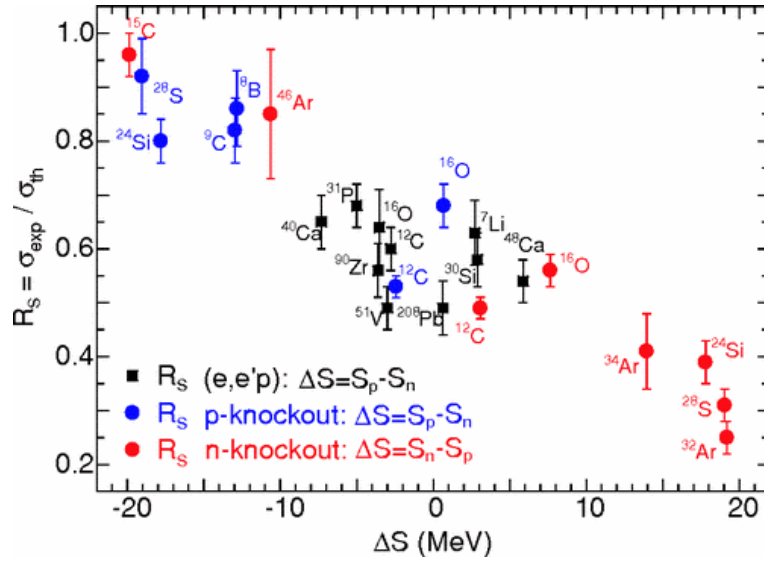


Figure 2.1: Illustration from Ref [32] containing a compilation of data from different knockout reactions, indicating the dependence of reduction factors R_s on the binding energy.

In Ref. [32], the reduction factor is reported as depending on the asymmetry of the neutron and proton Fermi surface. The asymmetry is proportional to the difference in proton and neutron separation energies ΔS . For neutron removal $\Delta S = S_n - S_p$, while for proton removal $\Delta S = S_p - S_n$. If we consider neutron removal reactions, and proton-rich nuclei, it follows that ΔS takes on large negative values because in this case neutrons are less bound compared to protons.

The R_s associated with an individual state is

$$R_s = -a|S_n \pm E - S_p| + b, \quad (2.14)$$

where the parameters a and b are 0.016 and 0.61, respectively [32].

3 | Reaction Model: Transfer Reactions

In order to study the neutron configuration of the ground state of ^{36}S , the (p, d) neutron pick-up reaction was performed. During a transfer reaction one or more nucleons are exchanged between the beam and the target. Such reactions proceed at relatively low beam energies in the order of a few MeV to several tens of MeV/u. Transfer reactions are useful experimental probes providing information on the location and occupation of orbitals [33]. In a transfer reaction the reaction can be approximated as a single step process and therefore this makes these reactions very important for spectroscopy as the cross sections in such scenarios are directly related to the overlap of the initial and final wave-function [33] (yielding spectroscopic factors). In this chapter I outline, the reaction models that have been used in this study to describe transfer reactions and how angular distributions have been used to extract information on the reaction mechanism.

3.1 Shell Model

It was discovered [34, 35, 36] that nuclei with certain combinations of neutron and proton numbers have enhanced stability (“magic”). These nuclei exhibit certain experimental signatures such as high first-excited 2_1^+ energies and relatively low $B(E2 : 2^+ \rightarrow 0_{gs}^+)$ values. Goppert-Mayer and Jensen [34, 35, 36] successfully managed to account for these magic numbers by introducing the spin-orbit interaction. The shell model falls under the independent-particle model and as such assumes that particles should be treated differently while moving independently in a common potential. According to the shell model nucleons exist in single-particle orbits which are derived from a mean field potential.

The shell model assumes the existence of single-particle wave functions as solutions to the Schrödinger equation. The Hamiltonian from the Schrödinger equation consists of two parts: 1) the many-body interaction term and 2) the kinetic energy. The other terms can be neglected from the many-body interaction and one can only consider the two-body interaction:

$$H = \sum_{i=1}^A \frac{-\hbar^2}{2m} \Delta_i + \sum_{i < j=1}^A V_{i,j}. \quad (3.1)$$

By including the a spherically symmetric potential $U(\mathbf{r})$ where $\mathbf{r} \equiv (r, \theta, \varphi)$ and the Hamiltonian becomes [37]:

$$H = \sum_{i=1}^A \left[\frac{-\hbar^2}{2m} \Delta_i - U(\mathbf{r}) \right] + \left[\sum_{i < j=1}^A V_{i,j} - U(\mathbf{r}) \right]. \quad (3.2)$$

In this form the Hamiltonian is characterized by two parts $H = H^s + V$, one which is

the single-particle Hamiltonian:

$$H^s = \sum_{i=1}^A \frac{-\hbar^2}{2m} \Delta_i - U(\mathbf{r}) \quad (3.3)$$

and the second part which represents the residual interactions:

$$V = \sum_{i<j=1}^A V_{i,j} - U(\mathbf{r}). \quad (3.4)$$

In an attempt to solve the single-particle part an angular parameter is introduced and, assuming a spherical potential, it becomes:

$$H^s \phi = \left(\sum_{i=1}^A \frac{-\hbar^2}{2m} \Delta_i - U(\mathbf{r}) \right) \phi = \epsilon \phi. \quad (3.5)$$

It is convenient and often useful to use spherical harmonics because they form a complete orthogonal basis and any function can be represented in the spin basis, hence the radial part can be solved easily. The radial part is solved by:

$$-\frac{\hbar^2}{2m} \frac{\partial^2 u}{\partial r^2} + \left(\frac{\hbar^2}{2m} + \frac{\ell + 2}{r} + U(r) \right) u(r) = \epsilon u(r). \quad (3.6)$$

It is then possible to form a basis by solving the radial part of the shell model, which in turn can be used in diagonalizing the residual interactions. A spin-orbit term is introduced to the single-particle part of the Hamiltonian to give [34]:

$$H^s = \frac{-\hbar^2}{2m}\Delta - \frac{1}{2}m\omega^2\mathbf{r}^2 + f_{\ell\ell}\vec{\ell}\cdot\vec{\ell} + f_{\ell s}\vec{\ell}\cdot\vec{s}. \quad (3.7)$$

3.2 Scattering Theory

The two-body scattering in quantum mechanics is well described by the Schrödinger equation and the goal of scattering theory is to find a solution to the Schrödinger equation. Nuclear reactions proceed in time and hence can be represented by a time-dependent Schrödinger equation:

$$-i\hbar\frac{\partial\psi(\mathbf{r},t)}{\partial t} = H(\mathbf{r},t)\psi(\mathbf{r},t), \quad (3.8)$$

where \mathbf{r} is a vector representing the distance between the target and scattered projectile, t is time, H is the Hamiltonian and ψ is the wave-function. It is difficult to obtain eigen-values for a dynamic process (involving time), therefore a term representing energy is required resulting in a time-independent Schrödinger equation:

$$H(\mathbf{r})\psi(\mathbf{r}) = E\psi(\mathbf{r}). \quad (3.9)$$

If the scenario is modeled as shown in Figure 3.1, the Schrödinger equation in 3 dimensions is:

$$\left(\frac{\hbar^2}{2\mu}\frac{\partial^2}{\partial\mathbf{r}^2} + \frac{\hbar^2\ell(\ell+1)}{2\mu r^2} + U(\mathbf{r}) - E\right)\psi_\ell(\mathbf{r}) = 0, \quad (3.10)$$

where $\hbar\ell$ is the angular momentum, related to the classical impact parameter: $\ell = kb$, k is the linear momentum, μ is the reduced mass and U is the potential. If the potential is independent of the direction of the vector separating nuclei, then the potential used is spherical. This indicates that the wave-functions are only dependent on \mathbf{r} and θ i.e. $\psi(\mathbf{r}, \theta)$. Assuming that the beam is a plane wave in the z direction, the incoming wave can then be represented as e^{ikz} , while the outgoing wave is well represented by a spherical wave. Combining the incident and outgoing scattered wave $\psi = \psi^{in} + \psi^{scat}$ and assuming $U(\mathbf{r}) \rightarrow 0$ as $\mathbf{r} \rightarrow \infty$, then the wave-function ψ representing the combined incident and scattered wave $\psi = \psi^{inc} + \psi^{out}$ is [38]:

$$\psi(\mathbf{r} \rightarrow \infty) = A \left[e^{ikz} + \frac{e^{ikr}}{r} f(\theta) \right], \quad (3.11)$$

where $f(\theta)$ is the scattering amplitude and is important because it is directly related to the differential scattering cross section $\frac{d\sigma}{d\Omega}$ (observable) by the relation:

$$\frac{d\sigma}{d\Omega} = \frac{v_{out}}{v_{in}} |f(\theta)|^2, \quad (3.12)$$

where v_{out} , v_{in} is the velocity of the scattered particle and incident particles, respectively. The wave function can be approximated using partial waves by applying Legendre polynomials ($P_\ell(\cos\theta)$) to give:

$$\psi(\mathbf{r}, \theta) = \frac{i}{k\mathbf{r}} \sum_{\ell=0}^{\infty} (2\ell + 1) i^\ell P_\ell(\cos\theta) \chi_\ell(\mathbf{r}), \quad (3.13)$$

where the partial waves are represented by χ_ℓ . The scattering amplitude for measuring a particle along the direction $\mathbf{r}(\theta)$ is given by [39]:

$$\begin{aligned}
f(\mathbf{r}) &= -\frac{\mu}{2\pi\hbar^2} \int d\mathbf{r}' e^{i\mathbf{k}' \cdot \mathbf{r}'} U(\mathbf{r}') \psi(\mathbf{r}', k') \\
&= -\frac{\mu}{2\pi\hbar^2} \langle e^{i\mathbf{k}' \cdot \mathbf{r}} | U(\mathbf{r}') | \psi(\mathbf{r}', k') \rangle.
\end{aligned} \tag{3.14}$$

Since we are dealing with a system of interacting nucleons it is therefore convenient to further decompose the Hamiltonian H into the kinetic energy $T = \frac{\hbar^2 k^2}{2\mu}$ and potential energy $U(\mathbf{r})$. The Schrödinger equation becomes $(E - T)|\psi\rangle = U(\mathbf{r})|\psi\rangle$. Because it is difficult to obtain an exact solution of the Schrödinger, certain approximations and boundary conditions are used to describe the wave function. In the form just shown the Schrödinger equation can be treated as an inhomogenous partial differential equation. A powerful method that can be used to solve partial differential equations is the Green's method. The Green's function is an inverse operator having the general form [39]:

$$\hat{G}^\pm = \frac{1}{E - T \pm i\epsilon}. \tag{3.15}$$

A more general form of the Schrödinger equation then becomes:

$$|\psi^\pm = |\phi\rangle + \frac{1}{E - T \pm i\epsilon} U(\mathbf{r})|\psi^\pm\rangle. \tag{3.16}$$

The superscripts $-$ and $+$ represent the incoming and outgoing wave functions respectively and ϕ represents a homogeneous solution. In scattering theory any physical quantity can be represented by an operator. The transition operator \mathbf{T} connects the initial states to the final states:

$$\mathbf{T} = \frac{-2\mu}{\hbar^2 k} \langle \phi^{(-)} | U(\mathbf{r}) | \psi \rangle. \tag{3.17}$$

If we recall equation 3.14, then it follows that the scattering amplitude is related to the

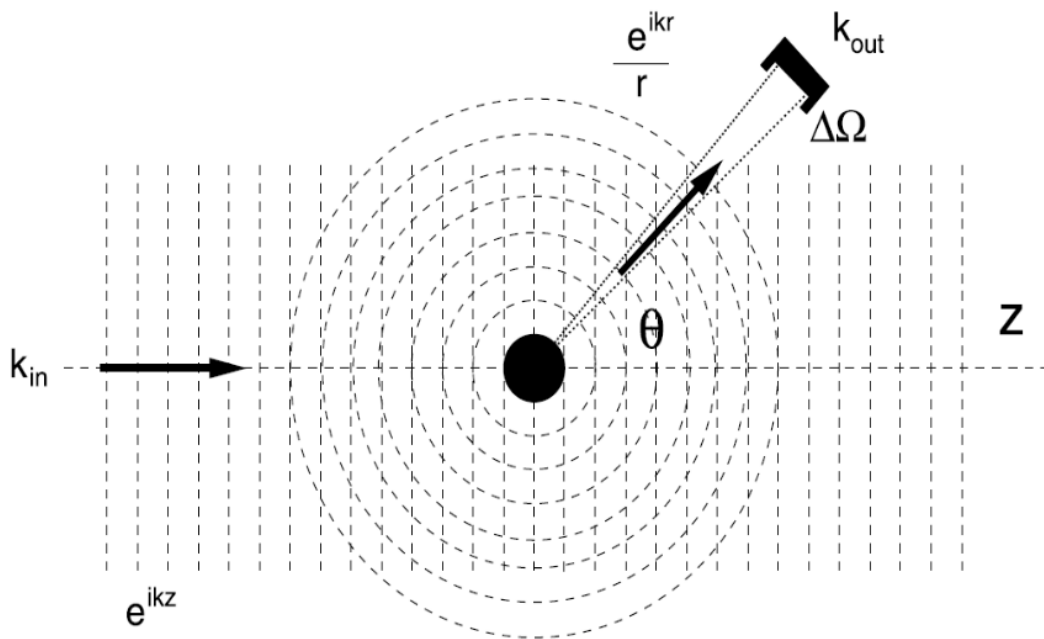


Figure 3.1: Quantum mechanical illustration of scattering [40].

\mathbf{T} matrix by:

$$f(k, k') = \frac{-\mu}{2\pi\hbar^2} \mathbf{T}(k, k'). \quad (3.18)$$

Likewise by introducing the transition operator or \mathbf{T} matrix, such that $\mathbf{T}|\phi\rangle = U|\psi^+\rangle$, and multiplying everything by the potential U , the Schrödinger equation can be written as:

$$\mathbf{T}|\phi\rangle = U(\mathbf{r})|\phi\rangle + U(\mathbf{r}) \frac{1}{E - T \pm i\epsilon} \mathbf{T}|\phi\rangle. \quad (3.19)$$

Equation 3.16 and 3.19 are widely known as the Lippmann-Schwinger equations. In general, in scattering theory, the scattering mechanism can be described using a Hamiltonian for the projectile at finite range by employing partial waves (differential form of equations) and using the integral formulation which includes Lippmann-Schwinger equations. Using the Lippmann-Schwinger equations, it can be shown that the \mathbf{T} matrix is proportional to the scattering amplitude [39].

3.2.1 Distorted Wave Born Approximation (DWBA)

The DWBA theory considers the projectile and ejectile in a transfer reaction to be moving under the influence of the long-range Coulomb interaction and short-range nuclear interaction. The formalism assumes that elastic scattering is the prominent and more significant component in a transfer reaction, while the inelastic component is only treated as a perturbation. The DWBA formalism employs a two potential formula: $U(\mathbf{r}) = U_1(\mathbf{r}) + U_2(\mathbf{r})$ where $U_1(\mathbf{r})$ is the distorting potential and $U_2(\mathbf{r})$ is treated as a perturbation. The Lippmann-Schwinger equations including the two potentials are shown in Table 3.1. Therefore the Schrödinger equation within the framework of the DWBA approximation can be written as:

$$(E - T - U_1(\mathbf{r}) - U_2(\mathbf{r}))|\psi\rangle = 0, \quad (3.20)$$

where for the outgoing wave $\psi = \chi + \hat{G}^+ U_2(\mathbf{r})\psi$ and χ represents the distorted wave. In the DWBA approximation the motion is not described by plane waves but by "distorted waves" that arise mostly due to the elastic scattering. The term $e^{i\mathbf{k}\mathbf{r}}$ is replaced by $\chi(\mathbf{r}) + \psi$.

Table 3.1: Lippmann-Schwinger equations including the two potential formula [39].

Form	Schrödinger equation	Lippmann-Schwinger equations	Solution
free	$[E - T]\phi = 0$	$\hat{G}^+ = [E - T]^+$	$\phi = F$
distorted	$[E - T - U_1(\mathbf{r})]\chi = 0$	$\chi = \phi + \hat{G}^+ U_1(\mathbf{r})\chi$	$\chi \rightarrow \phi + \mathbf{T}^{(1)}H^+$
full	$[E - T - U_1(\mathbf{r}) - U_2(\mathbf{r})]\psi = 0$	$\psi = \phi + \hat{G}^+(U_1(\mathbf{r}) + U_2(\mathbf{r}))\chi$	$\psi \rightarrow \phi + \mathbf{T}^{(1+2)}H^+$

As alluded to earlier ϕ is a solution for no potential, such that each partial wave $\phi = F$, χ represent the solution for the distorting potential $U_1(\mathbf{r})$ and ψ refers to the full solution. Withing the DWBA framework it follows that there should be a two potential formula including the \mathbf{T} matrix as well. Using equation 3.19 the \mathbf{T} matrix due to a scattering by $U_1(\mathbf{r})$ is denoted as $\mathbf{T}^{(1)}$ [39]:

$$\mathbf{T}^{(1)} = \frac{-2\mu}{\hbar^2 k} \langle \phi^{(-)} | U_1(\mathbf{r}) | \chi \rangle. \quad (3.21)$$

It can be shown using a longer derivation [39] that the \mathbf{T} matrix for the combined potentials $\mathbf{T}^{(1+2)}$ satisfies the relation:

$$\frac{\hbar^2 k}{-2\mu} \mathbf{T}^{(1+2)} = \langle \phi^{(-)} | U_1(\mathbf{r}) | \chi \rangle + \langle \chi^{(-)} | U_2(\mathbf{r}) | \psi \rangle. \quad (3.22)$$

Part II

PART II: The GRETINA-S800

$^{34}\text{Si}, ^{36}\text{S}(-1n)$ knockout

Experiment and Results

4 | Experimental Details: the $^{34}\text{Si}, ^{36}\text{S}(-1n)$ knockout reactions

The $^9\text{Be}(^{36}\text{S}, ^{35}\text{S}+\gamma)\text{X}$ and $^9\text{Be}(^{34}\text{Si}, ^{33}\text{Si}+\gamma)\text{X}$ reactions were performed at the NSCL facility, using the S800 spectrometer coupled to the GRETINA array. For each of the reactions ^{36}S and ^{34}Si were produced as secondary beams. For each of the secondary beams the rigidity settings were adjusted so as to select the $(-1n)$ reaction residue. The prompt γ -rays following the de-excitations of the reaction residues, were detected by the GRETINA array. This chapter describes the experimental techniques used to perform the knockout reactions and collect data for this experiment. As a reminder it is worthwhile mentioning that this experiment was performed for the study of Mutschler *et al.*, [23] who analysed the data. In the current project the resulting calibration of particle detectors and corresponding efficiency values were taken directly from this previous study. The reanalysis performed in this study was that involving the unfolding of data (extracting scaler events to determine number of incoming and outgoing particles), particle identification for both incoming beams and outgoing knockout residues, extraction of parallel momentum distributions and the γ -ray analysis.

4.1 Radioactive Beam Production

Prior to this study, the ^{36}S isotope was not readily available as an enriched target mainly because of its relative abundance (of 0.01%) (this challenge was overcome as detailed later in Chapter 7 for the K600 experiment), while ^{34}Si is unstable to β^- decay with a half life of 2.8 s [41]. Therefore it was more feasible to use these isotopes in the form of beams rather than as targets. This can be done at NSCL using in-flight fragmentation of stable primary beams such as ^{48}Ca which was used in this experiment to produce the secondary beams ^{36}S and ^{34}Si .

Initially ^{48}Ca , is heated in an oven producing a vapor of neutral atoms [42]. The atoms are then ionized by collisions with electrons in the ECR (Electron Cyclotron Resonance) [42] which are confined by a magnetic field and manipulated using a RF (radio frequency). After the atoms are ionized they are injected into the K500 cyclotron [42].

A cyclotron operates on the principle of confining particles with a charge q in a uniform magnetic field and thereafter using a RF electric field to accelerate them to a certain frequency:

$$\rho = \frac{p}{qB}, \quad (4.1)$$

$$\omega = \frac{qB}{\gamma m}, \quad (4.2)$$

where ρ represents the radius of the flight path of the particles with charge q , in a uniform magnetic field B with momentum p and frequency ω . In the K500 cyclotron, particles are only accelerated up to $\sim 0.15c$ and thereafter are transported to the second K1200

cyclotron [42] where they are accelerated to the desired velocity. Using equation 4.1 it can be noted that to increase the momentum (hence velocity) of the particles the magnetic field, the radius or charge of the particles needs to be increased. However, because it is not easy to change the radius (this means changing the size of the cyclotron) or the magnetic field B , the velocity of the particles is increased by increasing their charge state using a carbon stripper foil. Once the beam is accelerated to the required energy in the K1200 it then bombards a thick ^9Be target (846 mg/cm² in the case) to produce a cocktail of secondary beams containing either ^{36}S or ^{34}Si isotopes of interest in greater proportions. The A1900 fragment separator [43, 42] is used to separate different isotopes using a $B\rho$ selection. The term $B\rho$ is the magnetic rigidity and is useful because it can separate different isotopes according to the radius of curvature of their trajectories:

$$qvB = \frac{mv^2}{\rho}, \quad (4.3)$$

meaning:

$$B\rho = \frac{mv}{q}. \quad (4.4)$$

The selection is then made possible using slits that only accept particles within a specified trajectory. Another step in the beam selection is when the beam is passed through an aluminum foil which causes the beam to lose energy from collisions with atomic electrons, whereby the energy loss of charged particles through matter is governed by the Bethe formula [44]:

$$-\frac{dE}{dx} = \frac{4\pi e^4 z^2}{m_e v^2} NZ \left[\ln \frac{2m_e v^2}{I} - \ln \left(1 - \frac{v^2}{c^2} \right) - \frac{v^2}{c^2} \right], \quad (4.5)$$

and ze is the charge of the primary particle, v is the velocity, Z is the atomic number of the absorber, m_e is the rest mass of an electron, e is the electronic charge, N is the target electron density and I is the ionization potential of the target material.

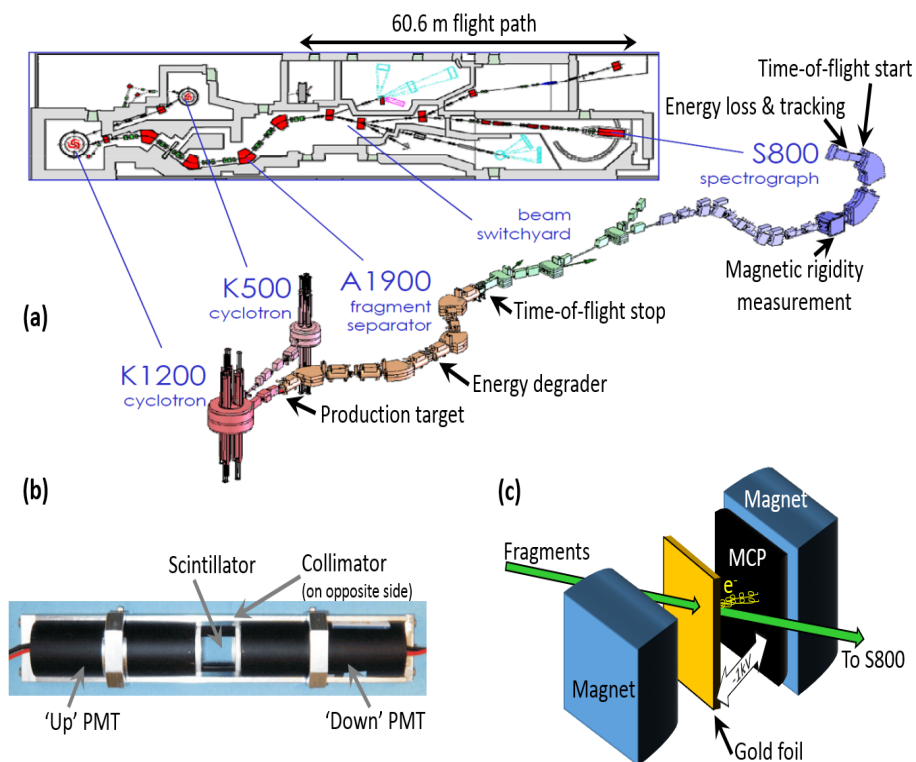


Figure 4.1: Schematic representation of the layout of the K500, K1200 cyclotrons and the S800 spectrometer adapted from [45]. (a) is the time-of-flight (TOF) setup to measure mass. (b) Shows the photo-multiplier and scintillators used for TOF measurements providing stop and start signals at the A1900 fragment separator and S800 focal plane. (c) Shows the setup for the rigidity measurement at the target position of the S800, where the green arrows indicates the beam after fragmentation.

4.2 The S800 spectrograph

After “purification” in the A1900 separator, the ^{36}S and ^{34}Si secondary beams were guided to the S800 magnetic spectrograph [46] shown in Figure 4.1 with the focal plane shown in

Figure 4.2. The second ^9Be target of thickness 100 mg/cm^2 is located at the pivot of the S800. The S800 spectrograph magnetic field was adjusted to transmit neutron knockout residues of interest.

The S800 spectrograph is separated into two parts: the beam analysis line, which is used solely for the purpose of beam diagnostic and selecting the required setting for optics modes. The analysis line operates using either one of two modes, which are: dispersion-matched or focused mode. Operating in focused mode allows for a relatively large acceptance of the analysis line that can be delivered (approximately $\pm 2\%$) [46]. This is because in focused mode the analysis line is achromatic and as a consequence there is a chromatic image at the focal plane of the spectrograph, i.e the beam is focused at the target, but dispersed at the focal plane.

The reaction residues finally arrive at the focal plane of the S800 where they are detected and characterized. The focal plane comprises:

- a pair of cathode readout drift chambers (CRDC's) as indicated in Figure 4.2 that give a two-dimensional position measurement and hence provide the particle trajectory,
- a segmented ionization chamber used primarily for identifying particles through their energy losses,
- a plastic scintillator (later called E1) that is used as a trigger for the S800 data acquisition and time-of-flight (TOF) identification [46].

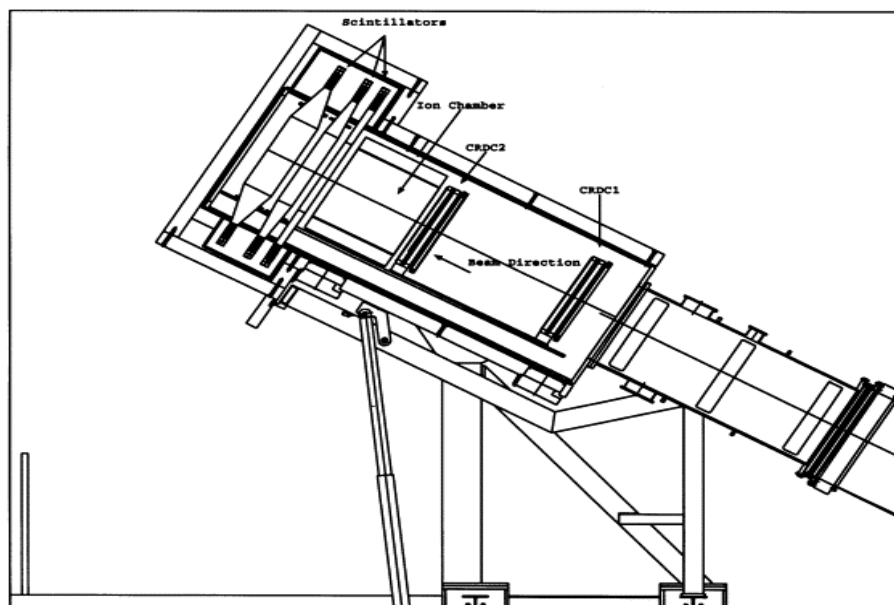


Figure 4.2: S800 focal plane showing the two CRDCs, ion chamber and scintillators [47].

4.3 Particle identification

4.3.1 Incoming and transmitted residue identification

The incoming ions are identified by measuring the TOF differences using three scintillators: E1, object position (OBJ) and extended focal plane (XFP) shown in Figure 4.3. Using the three scintillators two TOF difference measurements can be obtained which are all relative to the E1 scintillator located at the focal plane [46]. The incoming residues are selected according to their respective masses and momenta. Using the OBJ-E1 TOF, which is sensitive to the mass of the incoming residue and the OBJ TOF which depends on the particle trajectory, the different residues can be distinguished [46]. Identification of the knockout residues is achieved through their energy loss and TOF at the focal plane of the S800 spectrograph [46]. The residue energy loss in the ionization depends on the atomic number Z .

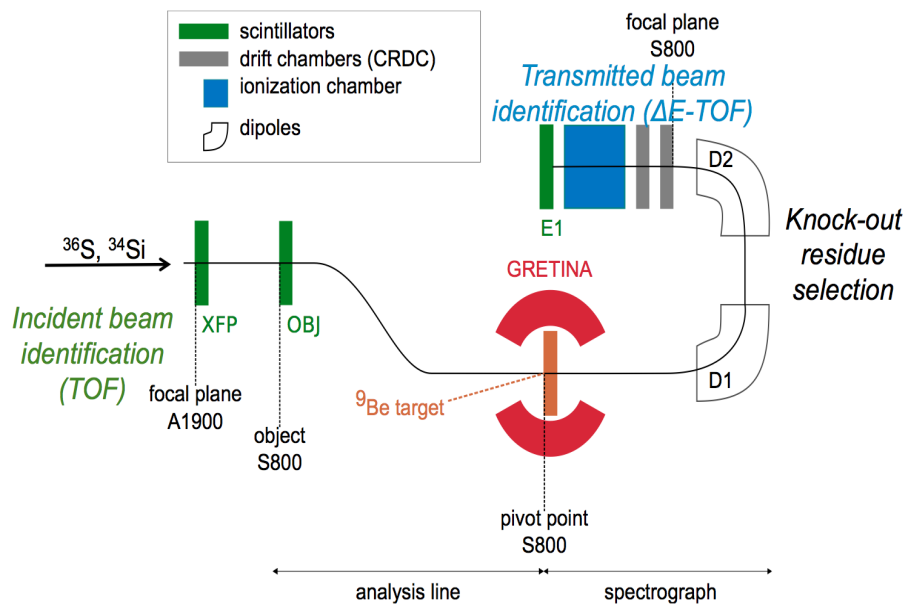


Figure 4.3: Schematic illustration of the S800 Spectrograph showing different sections in the analysis line and spectrograph [23].

4.4 Momentum reconstruction

Using the cathode-readout drift counters (CRDC's) which are used to detect the trajectory of the particle, we have (x_1, y_1) and (x_2, y_2) and then x_{fp} and y_{fp} are derived. A position (x_{fp}, y_{fp}) is determined which represents the dispersive and non-dispersive position, respectively while (a_{fp}, b_{fp}) represent the angles at the focal plane.. The x_{fp} coordinates are obtained by collection of charge in the cathode of the CRDC while y_{fp} is determined by the drift time. A calibration for the y_{fp} is performed with a mask having holes at marked positions.

It is necessary to reconstruct the particle's trajectory and to achieve this an analytical approach is employed. Using the ion-optics code COSY [48], it is possible to relate the particle's focal plane position and angle to target position, angle and energy parameters. The code implements this on an event-by-event basis by generating an inverse map

through the relation:

$$\begin{pmatrix} a_t \\ y_t \\ b_t \\ d_t \end{pmatrix} = S^{-1} \begin{pmatrix} x_{fp} \\ a_{fp} \\ y_{fp} \\ b_{fp} \end{pmatrix} \quad (4.6)$$

The coordinates (a_t, y_t, b_t, d_t) characterize the location of the nuclear reaction of interest. The parameters (a_t, b_t) represent the dispersive and non-dispersive angles, respectively, at the target, y_t represents the reconstructed y position at the target and d_t is the variation in energy from the central energy of the spectrograph. The experiment that is presented here is part of an experimental campaign in which several nuclei were studied in the same experimental conditions and the coordinates used in the analysis were obtained from the work done by [23].

4.5 The Gamma-Ray Energy Tracking In-beam Nuclear Array (GRETINA)

The prompt γ -rays emitted in flight by the knockout residues were detected using the GRETINA array [49]. The array consisted of seven modules, each module consisting of 4 coaxial Ge crystals. In order to enable a close packed geometry the individual crystals are tapered as shown in Figure 4.4. There are two types of crystals in each module: type A and type B. The difference between the crystals is the irregular/asymmetric hexagonal shape that is required to provide a spherical surface for the configuration. The full geometry of a module is illustrated in Figure 4.5. Each crystal is segmented into 36 segments, 6 longitudinal segments and 6 transverse segments as shown in Figure 4.6.

Without taking into consideration the tapering, each crystal is 9 cm in length and has a maximum diameter of 8 cm.



Figure 4.4: GRETINA array, showing ten detector modules (40 crystals) mounted in a close-packed configuration. In this work only 7 modules were used 4 being at forward angles with respect to the beam axis at 58° and 3 were placed at 90° [50].

4.5.1 Principle of operation

A γ -ray interacts with the Ge crystal by one of the three mechanisms: photoelectric absorption, Compton scattering and pair production [44]. The primary mode of interaction is photoelectric absorption for γ -rays with incident energy less than 200 keV. In the photoelectric effect the incident γ -ray deposits all its energy in the crystal. For photoelectric absorption to occur the γ -ray should have sufficient energy greater than the binding energy of the electron.

Compton scattering refers to a process where the γ -ray deposits only part of its energy in the crystal. This leaves the γ -ray free to lose the remaining energy by either subsequent

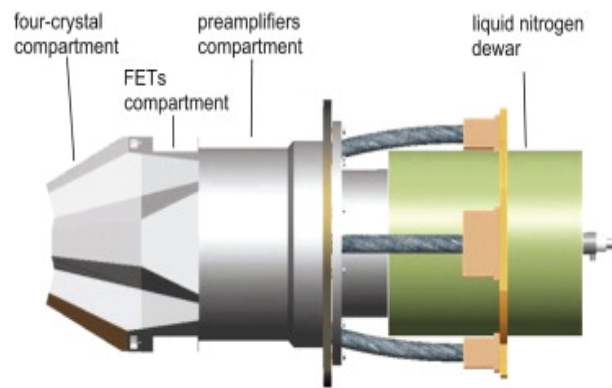


Figure 4.5: A schematic view of one GRETINA module [49].

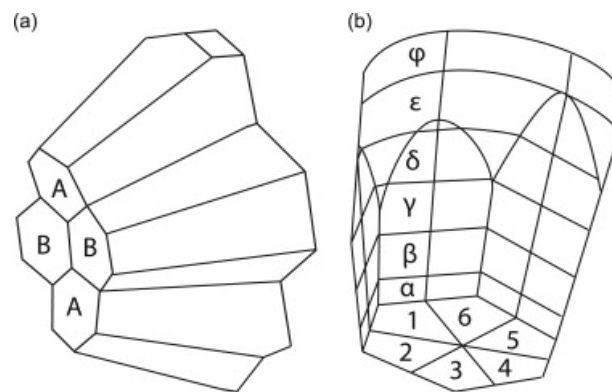


Figure 4.6: Schematic representation indicating the segmentation in a GRETINA module, the two types of crystals (A and B) are shown [49].

Compton scattering or the other two processes. Another possibility is that the γ -ray undergoes Compton scattering, but still deposits all of its energy within the crystal without escaping.

Compton scattering dominates in the energy range 200 keV - 8000 keV. Often it occurs that the γ -ray transfers some of its energy to the electron and then Compton scatters out of the crystal at an angle θ relative to its incoming trajectory. The energy of the incoming γ -ray E_{γ}^i can be related to part of the energy of the scattered γ -ray E_{γ}^f using [44]:

$$E_{\gamma}^f = \frac{E_{\gamma}^i}{1 + \frac{E_{\gamma}^i}{m_e c^2} (1 - \cos\theta)}. \quad (4.7)$$

Lastly, pair production occurs when the energy of the incident γ -ray is greater than or equal to the rest mass of the electron-positron pair (it dominates at energies greater than 8000 keV). The incident γ -ray interacts in the Coulomb field thereby creating an electron-positron pair. The positron promptly annihilates creating two 511 keV ($m_e c^2$) γ -rays emitted in opposite directions.

In this work it is more likely that we detect events originating from Compton scattering followed by photoelectric absorption. If a γ -ray undergoes multiple Compton scatters the energies must be added to determine the full energy of the incident γ -ray in a process called addback. A signal decomposition algorithm is used to identify and classify different interactions occurring in the crystal.

4.5.2 Signal Decomposition and γ -ray Tracking

The interaction of a γ -ray in germanium material causes the production of electron-hole pairs. By biasing the detector, the electron-hole pairs move in different directions inducing currents in each segment of the module. For each segment in which the γ -ray interacts there is a net current measured, while the other segments register no induced current. The amplitude of the signal is directly proportional to the energy deposited by the γ -ray. The signal decomposition performed serves the purpose of determining the number of interactions and corresponding energies and positions. There are a basis of signals computed for each detector that are used to perform decomposition.

All interaction points within a single crystal are assumed to originate from the same

γ -ray. Because of the forward peaking of the Compton scattering cross-section, the γ -ray interaction points are often clustered in a two dimensional space (θ, ϕ) [51]. The interaction points are grouped into clusters depending on a given angle of separation between interaction points (e.g all γ -rays within 20° belong to the same cluster). The interaction points grouped into a specific cluster are assumed to be originating from the interactions of one incident γ -ray. The Compton formula is then used to determine the different combinations of scattering sequences within a cluster. In order to achieve optimal position and energy resolution, firstly each of the scattering sequences are assigned a Figure-of-Merit (FM) value. This value quantifies how much the measured angles and position differ from expected values. In practice the scattering sequences with a value that is close to zero are ideal. Scattering sequences with a non-zero FM usually correspond to Compton events interactions from multiple γ -rays [49].

For this experiment, tracking was not used because given the low counting and multiplicity of the experiment, addback was clearly more efficient than any algorithm of tracking (that has always has a cut off in the FM, resulting in reduced efficiency).

5 | Analysis

This chapter describes the various analysis techniques employed in extracting parallel momentum distributions, inclusive cross sections and spectroscopic factors from both the ${}^9\text{Be}({}^{36}\text{S}, {}^{35}\text{S}+\gamma)\text{X}$ and ${}^9\text{Be}({}^{34}\text{Si}, {}^{33}\text{Si}+\gamma)\text{X}$ reactions. The procedure involved in unfolding the data collected from the GRETINA array and S800 spectrometer is explained. The analysis involved unfolding of data collected from the GRETINA array and S800 spectrometer is explained because it was re-analysed in this study using the software analysis package GrROOT developed by Wimmer *et al.*, [52]. The GrROOT program package is used for the analysis of experiments with the S800 spectrograph and GRETINA at NSCL/MSU. It allows for offline analysis, generating particle identification two dimensional histograms and addback doppler corrected γ -ray spectra [52].

5.0.1 Particle identification

The magnetic rigidity $B\rho = p/q$ is used to select the particles detected at the S800 focal plane, taking into consideration that for a specific value of q , the mass M_p of the reaction residues is proportional to its TOF (with the assumption that the path length is a constant). The timing scintillators XFP and OBJ provide two time differences relative to the E1 plastic scintillator at the S800 focal plane. The two time differences are OBJ-

XFP, which is dependent upon the mass of the incoming projectile, and the OBJ-E1 which depends on the mass of the transmitted reaction residues.

It follows that the energy loss has a quadratic dependence on the atomic number Z and the incoming beam consists of different nuclei hence different values of Z . If nuclei have almost equal values of mass then $\beta = \frac{v}{c}$ will be almost similar for the different nuclei. In order to distinguish between the different nuclei, the atomic number Z is used which corresponds to different energies deposited in the ionization chamber.

The reaction residues are identified using both the mass discrimination from the TOF and the different atomic charges (Z) from energy loss values. A particle identification plot is shown in Figures 5.1 and 5.2 to show the identification of the incoming beam and outgoing knockout residues.

5.1 Relative γ -ray efficiency

Energy and efficiency calibrations were performed using a ^{152}Eu radioactive source. The decomposition algorithm of GRETINA provides an output of calibrated energies. The energy calibration performed by the algorithm is very precise and therefore no additional energy calibration is required. Only a relative efficiency calibration was performed because the absolute efficiencies were obtained before [53]. The photo-peaks used for the relative efficiency calibration are from ^{152}Eu as listed in Table 5.1.

It is possible for γ -ray to undergo multiple Compton scattering at different points within a crystal or adjacent crystal. At each interaction point the γ -ray deposits some energy. Therefore as a result the energy deposited at each interaction point is not a reflection of the incident energy of the γ -ray. The incident energy of the γ -ray is equivalent to the

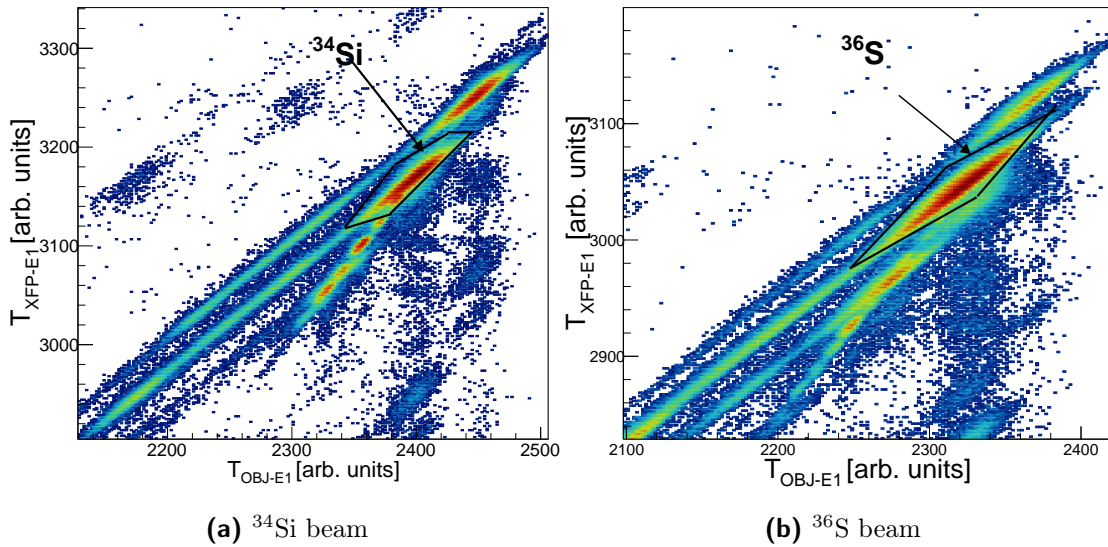


Figure 5.1: Incoming beam identification using time of flight between the OBJ and XFP scintillators for the (-1n) knockout setting from ^{34}Si beam shown in 5.1a and for ^{36}S beam shown in 5.1b.

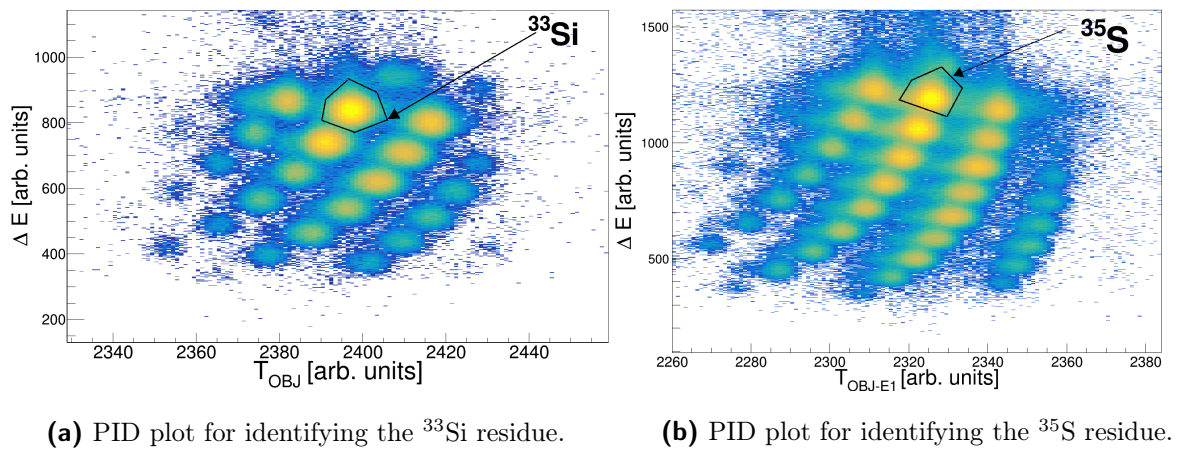


Figure 5.2: Particle identification plots to identify the knockout residues for the 1n settings. The TOF depends on the ratio of mass of the knockout residues to charge A/q while the energy loss depends on the nucleus's atomic charge Z^2 . Using this principle the knockout residues can be separated and have a definite loci as shown in the plot above where the colors indicate the intensity on a logarithmic scale. The highest intensity loci corresponds to the knockout residue of interest.

Table 5.1: Energies for photopeaks, number of emitted γ -rays per decay (relative intensities) and associated errors used from the ^{152}Eu source in relative efficiency calibration. The data used as reference was taken from Ref. [54].

Energy [keV]	Absolute Intensity [%]	Error in intensity
121.2	28.4	0.130
243.7	7.53	0.400
343.0	26.6	0.110
410.3	2.24	0.0100
443.3	3.13	0.0140
778.1	13.0	0.0600
866.5	4.21	0.0250
963.1	14.6	0.0600
1110.9	13.5	0.0600
1212.0	1.41	0.0080
1298.3	1.62	0.0110
1407.2	20.9	0.0900

sum of the energies deposited at all the different interaction points for a given event. It is assumed that the interactions in neighboring crystals are originating from the same γ -ray. The interaction point with the highest energy deposition is assumed to be the first hit. The addback procedure is performed to collect the total energy deposited by a γ -ray per event from the different interaction points within a crystal or neighboring crystals. Efficiency curves for addback and non-addback are compared in Figure 5.3. At energies above 700 keV the efficiency is highest in the addback spectra as compared to the non-addback spectra. This is because the addback procedure recovers Compton scattered events for the higher energy γ -rays. A problem arises, when there are γ -rays in coincidence. As at energies around 200 keV there are mostly photo-peaks, adding another γ -ray means adding a γ -ray from coincidence. This therefore depletes the correct energy

γ -ray to the benefit of a summed (but fake) peak.

The relative efficiency was then calculated using:

$$R_{\text{Eff}}(\%) = \left(\frac{\text{Area}}{I_{\gamma}} \right) \times 100. \quad (5.1)$$

The intensities I_{γ} of the γ -rays were calculated using the efficiency corrected areas under the peaks and normalized to the 778 keV γ -ray. A previous measurement of the absolute efficiency was performed by Ref. [55] using a multi-channel analyzer (MCA) with a calibrated dead time estimation connected to a single crystal of GRETINA. In order to be certain that the efficiency values were computed correctly, the efficiency curves were compared to values obtained by Ref. [55].

The relative efficiency was fitted with the formula:

$$\nu = e^{p_0 \ln(E) + p_1}, \quad (5.2)$$

and the resulting relative efficiency curves are shown in Figure 5.3.

5.2 Nearest-neighbor addback procedure

The addback factor refers to the ratio of the efficiency values obtained from addback spectra over the efficiency values obtained from non-addback spectra. A comparison between addback spectra and non-addback spectra is shown in Figure 5.4 and Figure 5.5 shows the addback factors obtained from the efficiency calculations by normalizing to the 778 keV γ -ray.

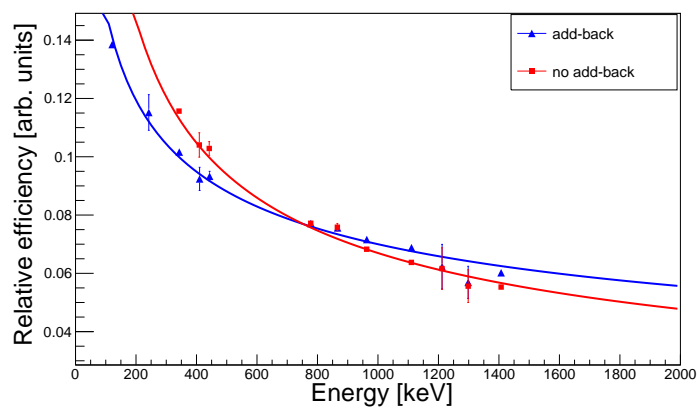


Figure 5.3: Relative efficiencies as a function of energy using a ^{152}Eu radioactive source for addback and non-addback mode. Intensities were obtained relative to the 778 keV γ -ray.

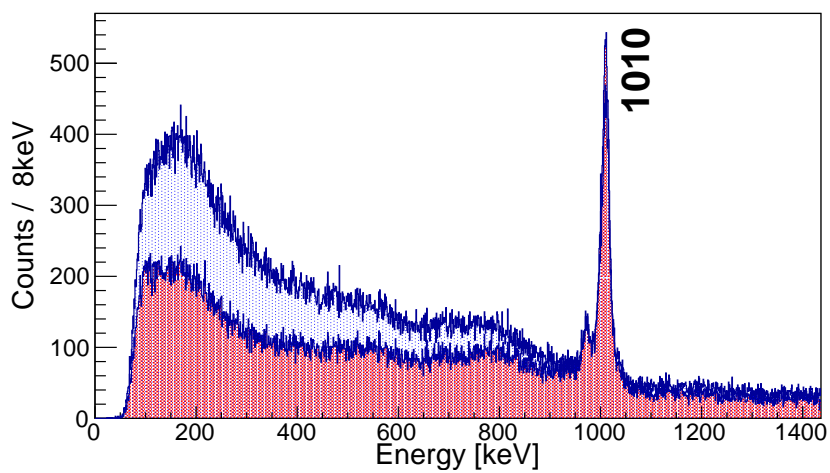


Figure 5.4: Comparison of addback (red) to non-addback (blue) spectra using in-beam data for ^{33}Si .

The addback procedure is performed by analyzing several interactions originating from one event. An interaction occurs when a γ -ray incident in a crystal deposits some energy then further scatters into another “neighboring” (crystal) and deposits the remaining energy (illustrated in Figure 5.6). Detectors are considered to be neighbors if they are: either adjacent within a cryostat or are adjacent to each other in different modules. It is required that both crystals share a boundary. The energies of the γ -ray that scattered are summed to constitute a single interaction. The interaction point with the highest energy deposition is assumed to be the first hit. Once the position of the first hit is identified then an angle for Doppler correction can be obtained.

Addback factors (AB_f) were computed using the in-beam data. The computed values included in the plot presented in Figure 5.5 using data points from ^{152}Eu (calibration data), ^{35}P [23] (to cover the energy range of interest) and ^{33}Si (in-beam data).

The equation used to fit the values is:

$$AB_f = p_0 + p_1(\sqrt{E}). \quad (5.3)$$

where p_0 and p_1 are parameters obtained from the fit.

5.3 Energy resolution

The energy resolution is characterized by the full width at half maximum (FWHM) of the γ -ray peaks and is defined as [56]:

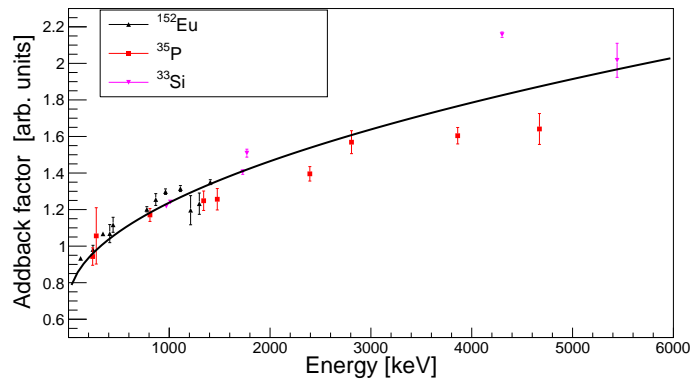


Figure 5.5: addback curve including in-beam points from ^{33}Si , ^{35}P (obtained from [23]) and ^{152}Eu calibration data.

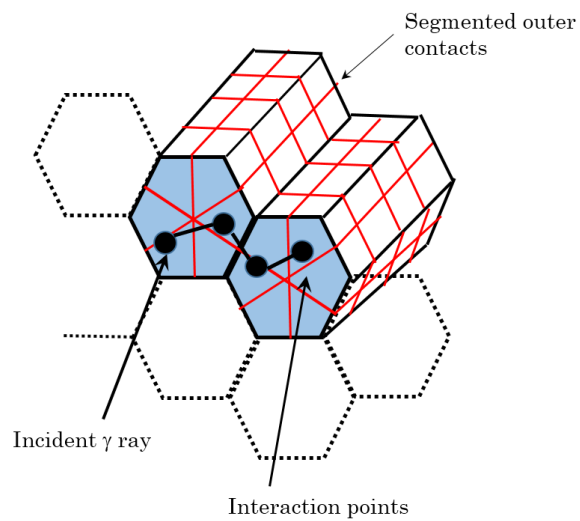


Figure 5.6: Schematic representation of the addback performed in detector crystals.

$$R = \frac{\Delta E_{\gamma}^{rest}}{E_{\gamma}^{rest}} = \frac{2.35\sigma_E}{E_{\gamma}^{rest}}, \quad (5.4)$$

where σ_E is the standard deviation, E_{γ}^{rest} is the energy of the γ -ray emitted by the residue in its rest frame and ΔE_{γ}^{rest} is the FWHM of the γ -ray peak at energy E .

It is important to evaluate the different contributions to the energy resolution. The total FWHM consists of two components:

$$FWHM = \sqrt{FWHM_i^2 + FWHM_D^2}, \quad (5.5)$$

where $FWHM_i$ is a result of the intrinsic detector properties and also consists of three components: $FWHM_{en}$ (electronic noise), $FWHM_{sf}$ (statistical factor) and $FWHM_{icc}$ (incomplete charge electrons) [44].

The second contribution $FWHM_D$ is due to the Doppler effect. For high beam energies such as the one in this experiment ($v \sim 0.3c$), the Doppler effect becomes highly significant. This is manifested in the observed energies of γ -rays emitted in-flight by residues, being shifted by a certain factor. A relativistic Doppler correction is required to correct the observed energy shifts in γ -ray spectra. The γ -ray energies are shifted according to the formula [44]:

$$E_{\gamma}^{rest} = E_{\gamma}^{lab} \gamma (1 - \beta \cos(\theta_{lab})), \quad (5.6)$$

where θ_{lab} is the angle of the emitted γ -ray with respect to the reaction residue direction and β is v/c and is equivalent to residue velocity and $\gamma = 1/\sqrt{(1 - \beta^2)}$. It is necessary

to perform a Doppler correction because we are interested in the energies of the nucleus in the rest frame. In order to reconstruct the energy in the rest frame β and θ_{lab} are needed.

The Doppler contribution comprises two components:

$$FWHM_D = \sqrt{FWHM_{\theta_{lab}}^2 + FWHM_{\beta}^2}, \quad (5.7)$$

where $FWHM_{\theta_{lab}}$ is due to the uncertainty in determining the emission angle and $FWHM_{\beta}$ arises as a result of the uncertainties in the velocity. Since $FWHM = 2.35\sigma_E$ we can incorporate σ_E to have [57]:

$$\sigma_E = \sqrt{\sigma_{int}^2 + \sigma_{E,\beta}^2 + \sigma_{E,\theta}^2}, \quad (5.8)$$

where [57]:

$$\sigma_{E,\beta} = \frac{\delta E_{\gamma}^{rest}}{\delta \beta} \sigma_{\beta} = \frac{E_{\gamma}^{rest}(\beta - \cos(\theta_{lab}))}{(1 - \beta^2)(1 - \beta \cos(\theta_{lab}))} \sigma_{\beta} \quad (5.9)$$

and:

$$\sigma_{E,\theta} = \frac{\delta E_{\gamma}^{rest}}{\delta \theta} \sigma_{\theta} = \frac{E_{\gamma}^{rest}(\beta \sin(\theta_{lab}))}{1 - \beta \cos(\theta_{lab})} \sigma_{\theta}. \quad (5.10)$$

The total uncertainty in the energy resolution is then given by:

$$\left(\frac{\sigma_E}{E_{\gamma}^{rest}} \right)^2 = \left(\frac{\beta \sin(\theta_{lab})}{1 - \beta \cos(\theta_{lab})} \right)^2 (\sigma_{\theta})^2 + \left(\frac{\beta - \cos(\theta_{lab})}{(1 - \beta^2)(1 - \beta \cos(\theta_{lab}))} \right)^2 (\sigma_{\beta})^2 + \left(\frac{\sigma_{int}}{E_{\gamma}^{rest}} \right)^2 \quad (5.11)$$

5.4 Population fraction

The population fractions were computed using γ -ray intensity balance. This was done by subtracting the contribution of γ -rays feeding a state from γ -rays being emitted from that state. This was performed by fitting a specific peak area and correcting for peak-to-total (P/T) efficiency, the resulting efficiency corrected areas are used in the subtraction. The population fractions were computed using the formula [23]:

$$b_f = \frac{\sum_{\gamma \leftarrow i} \frac{N_\gamma}{\epsilon_\gamma} - \sum_{\gamma \rightarrow i} \frac{N_\gamma}{\epsilon_\gamma}}{N_{knockout}}, \quad (5.12)$$

where N_γ represents the number of counts under the γ -ray of interest, ϵ_γ is the P/T efficiency and $N_{knockout}$ is the number of knockout residues in a given reaction.

5.5 Inclusive Cross section

The inclusive cross section takes into account the sum of all reaction channels leading to bound states. It is obtained by counting the number of knockout residues registered in the E1 scintillator in the focal plane. It was determined using:

$$\sigma_{inc} = \frac{N_r}{N_i} \frac{1}{N_t}, \quad (5.13)$$

where N_r is the number of knockout reaction residues for the reaction and N_i is the number of incident beam particles. N_t is related to the target thickness by $N_t = nx$, where n is the number of target atoms per volume, and x is the thickness. N_r is obtained

by determining the number of counts in the gate applied in the PID plot shown in Figure 5.2. It has an associated statistical error of $\sqrt{N_r}$. The value of N_r is calculated using [23]:

$$N_r = N_{S800}^{SC} f_p f_{TOF}, \quad (5.14)$$

where N_{S800}^{SC} is the number of S800 focal plane events provided by the scalers, f_p represents the fraction of knockout residues after the target and f_{TOF} is the fraction of incident particles selected solely from prompt events in the identification matrix.

The number of incident beam particles are calculated using [23]:

$$N_i = N_{OBJ}^{SC} P \frac{T}{\epsilon_{OBJ}}, \quad (5.15)$$

where N_{OBJ}^{SC} refers to the number events provided by the scalers in the OBJ scintillator, P is the purity of the beam, T is the transmission of the knockout residues along the analysis line of the S800 spectrograph and ϵ_{OBJ} is the efficiency of the OBJ scintillator.

5.5.1 Least squares fit of parallel momentum distributions

In comparing the theoretical predictions for the parallel momentum distributions to experimentally obtained distributions, χ^2 values were computed to see which of the theoretical distributions is a better fit to experimental data. In computing the χ^2 value certain precautions have to be taken into account. If statistics is low then different binning can lead to significantly different results obtained from a fit. Re-binning the data affects the

relative weights or contents in each bin (relative heights). As such when histograms are shifted a procedure was performed so as to use a histogram with correct bin contents. The χ^2 value was computed and follows a histogram with N bins:

$$\chi^2 = \sum_{i=1}^N \frac{(y_e - y_t)^2}{y_t}, \quad (5.16)$$

where N represents the number of bins, y_e are the experimental values and y_t are the theoretical values.

The drawback in using this equation to calculate the least squares is that it can poorly estimate the χ^2 value for histograms with low statistics. In the values quoted the normalized χ^2 values were used which is simply the χ^2 value divided by the number of degrees of freedom (i.e number of bins - 1):

$$\chi_{Normalized}^2 = \frac{\chi^2}{N - 1}. \quad (5.17)$$

6 | Results and Interpretation

In this chapter the obtained parallel momentum distributions, spectroscopic factors and cross sections are presented and interpreted. The experimental parallel momentum distributions are compared with theoretical predictions enabling the assignment of orbital angular momentum values to different states. In addition the experimental spectroscopic factors are compared with theoretical calculations and results from previous experiments.

6.1 ${}^9\text{Be}({}^{34}\text{Si}, {}^{33}\text{Si}+\gamma)\text{X}$

6.1.1 Inclusive cross sections to all bound states

As detailed previously in Chapter 5 equation 5.13, the inclusive cross section is computed using the total number of incident nuclei N_i , and the number total knockout reaction residues taking into account the time of data acquisition being approximately one hour and the resulting value for $1/nx = 149$ b. The knockout originated from the reaction on a 100 mg/cm^2 thick ${}^9\text{Be}$ secondary target. The inclusive cross section for the ${}^{34}\text{Si}(-1n){}^{33}\text{Si}$ was calculated to be $\sigma_{inc} = 116(6)$ mb

6.1.2 Number of incident nuclei

To obtain the value of σ_{inc} it is necessary that the number N_i is known. This is extracted using recorded scalers from the OBJ scintillator in the object plane of the S800. It was found that $N_{OBJ}^{SC} = 1.17 \times 10^9$, $P = 70.5\%$, $T/\epsilon_{OBJ} = 0.851$ and a value measured for $N_i = 7 \times 10^8$ counts. The uncertainty in this number is given by the statistical counting equivalent to $\sqrt{N_i}$. The value of N_{OBJ}^{SC} was obtained from scaler events as a result of monitoring the rate of the OBJ scintillator scaled to a calibration where the rigidity of the S800 was centered on an unreacted run. This is where the rigidity of the S800 is set to match the value of the fragment beam (selected in the A1900) after passing through the S800 target. As a result any errors associated with fluctuations in beam rate are accounted for. This leaves the main source of uncertainty to be due to the composition of the beam where in particular with cocktail beams, the composition can change as function of time. To account for this cross sections are calculated run by run. In the case of ${}^{34}\text{Si}$ beam, the inclusive cross section was calculated for the available 3 runs having values of 113 mb, 126 mb and 118 mb. Assuming these runs are of equal importance the resulting systematic error is 6 mb.

The value of ϵ_{OBJ} is obtained by analyzing a run for unreacted beam, the unreacted run is when the S800 is tuned to transmit nuclei that pass the target without interacting. The value of ϵ_{OBJ} is computed by using the ratio of counting the nuclei registered in the S800 focal plane to the number of nuclei counted in the OBJ scalers. It should be noted that this method applies to the condition that efficiency of detection is 100% in the spectrograph part. The purity of the beam refers to the ratio of the number of incident particles which interact in relation to the number of incident particles available extracted using the TOF from the OBJ-E1 matrices deduced using the unreacted beam run. .

Number of knockout residues

To determine the number of knockout residues the scaler events are counted from the E1 scintillator located at the focal plane. From the resulting analysis $N_{S800}^{SC} = 3.11 \times 10^6$ counts, and $f_p = 30\%$ is the fraction of residues produced obtained using the PID matrix. It represents the fraction of nuclei produced as per selection using δE and TOF compared to the total number of nuclei. The parameter $f_{TOF} = 57.5\%$ and represents the proportion of incident nuclei in the TOF selection in the total number of nuclei. Therefore, the value for N_r obtained is 5.42×10^5 counts.

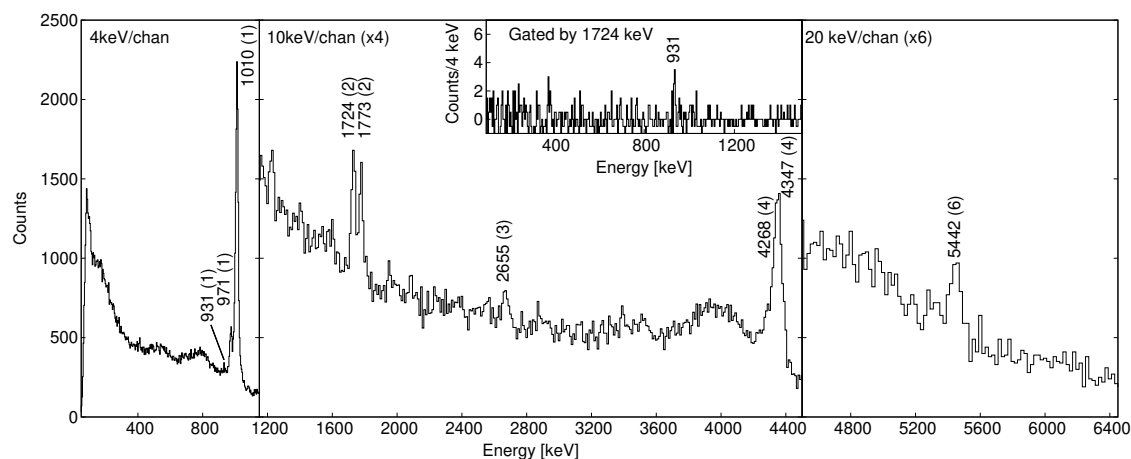


Figure 6.1: Add-back, Doppler corrected spectra showing γ -rays observed in this work for ${}^{33}\text{Si}$. The 931 keV transition is observed in coincidence with the 1724 keV transition (see inset.)

6.1.3 Level scheme

The level scheme of ${}^{33}\text{Si}$ has been established from previous work using different techniques such as the one-neutron knockout reaction [58], deep-inelastic reactions with a thick targets [59, 60], β -decay studies [61] and multi-nucleon transfer [62, 63]. A neutron knockout reaction was performed by [58] but due to limited statistics and energy

resolution, only three states were observed at 1.06 MeV, 4.32 MeV and the ground state. Due to the high γ -ray detection efficiency and good resolution of the GRETINA γ -ray tracking array, seven photo-peaks were observed up to 5.5 MeV as shown in Figure 6.1 and the level scheme consistent with the γ -rays observed is shown in Figure 6.2.

A coincidence is observed between the 971 keV and 1010 keV transitions as shown in Figure 6.3 and also between the 931 keV and 1724 keV transitions. An unexpected observation was made where two states at 4931 keV and 5441 keV are emitting γ -rays above the neutron separation energy ($S_n = 4.5$ MeV). It is less common to observe γ -rays competing with neutron emission while it is not surprising for γ -rays to compete with proton emission, where the proton emission is inhibited by the Coulomb barrier. For a γ -ray to be preferentially emitted over neutron emission, a high angular-momentum value is required to inhibit neutron emission. Even though in the present experiment, starting with a 0^+ ground state in ${}^{34}\text{Si}$ and removing neutrons from the sd shells, it is impossible that a state with $\ell \geq 4$ is populated directly via knockout.

The isomer (10.2 ns lifetime) at 1435 keV was observed in previous work using a deep-inelastic reaction [59], however in the current experiment the γ -ray corresponding to this state was not observed. This is due to the fact that while it has a long lifetime of 10.2 ns it is emitted a distance away (~ 1.5 m) from the reaction point for it to be detected with good efficiency.

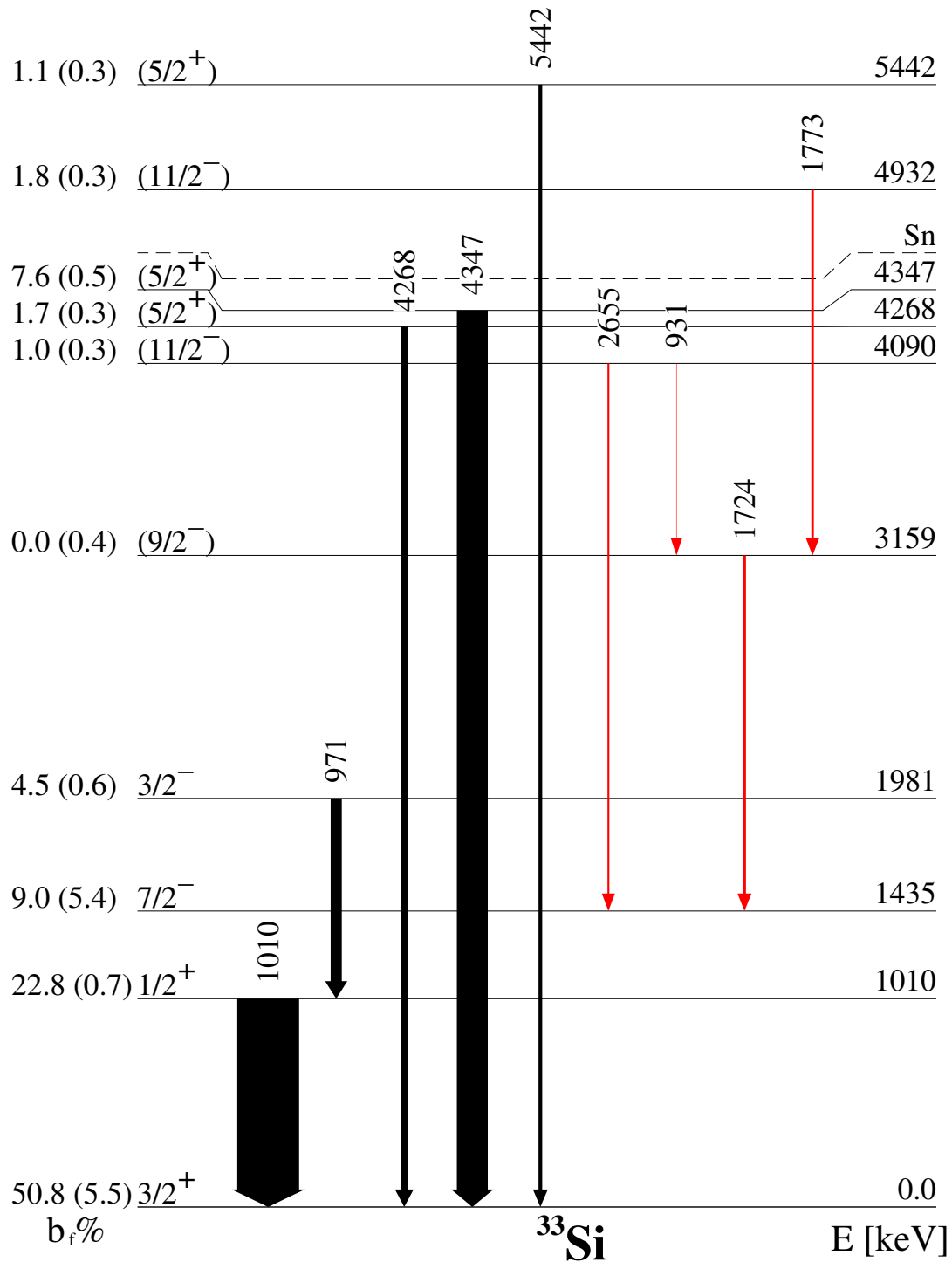


Figure 6.2: Level scheme for ${}^{33}\text{Si}$ from this work constructed using $\gamma\gamma$ coincidences and add-back spectra where the width of the arrows is proportional to the γ -ray intensity (which were normalized to the 1010 keV transition), b_f is the population fraction and spins and parity assignments are as suggested by Ref. [64]. The transitions marked in black originate from the removal of a neutron from the occupied sd - or the pf -shell valence orbits. Transitions shown in red connect higher-spin states, obviously requiring another reaction mechanism not yet identified.

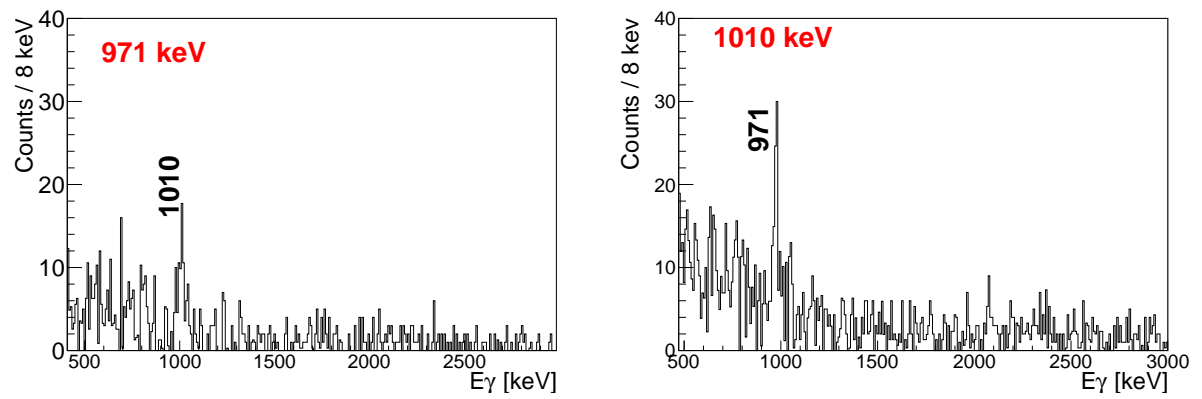


Figure 6.3: γ -ray gated spectra to show coincidences observed between the 971 keV and 1010 keV transitions. The gating transitions are indicated in red in the figures.

The experimental parallel momentum distributions that were measured at the focal plane for the knockout residues reflect the shift in momentum induced in the reaction. Following the mapping of focal plane parameters to target parameters, the momentum distributions are obtained from the positions of fragments measured at the target and focal plane. In constructing the exclusive (γ -ray gated) parallel momentum distributions the background subtraction was performed by extracting background only from the right side of the peak being fitted. The experimental distributions obtained in this work for the ${}^{34}\text{Si}(-1n)$ reaction are shown in Figure 6.4. The parallel momentum distributions are obtained using [29]:

$$p_{\parallel} = Q_f B \rho \left(1 + \frac{x_{fp}}{D_2} + \frac{x_t}{D_1} \right), \quad (6.1)$$

where x_{fp} represents the dispersive position, x_t refers to the reconstructed x position at the target, $B\rho$ is the magnetic rigidity, Q_f is the charge state and the dispersion at different points of the spectrometer related to the strength of the magnetic field are represented by D_1 and D_2 .

The interval used for subtracting the background was from $E_x + 1.5\sigma$ to $E_x + 4.5\sigma$, hence the width of the background considered was 3σ and E_x represents the centroid of the peak. For the states which are fed by states higher in excitation energy the contribution of the corresponding γ -ray was removed taking into account the efficiency of the γ -rays. This was done for the respective histograms corresponding to the parallel momentum distributions using:

$$p_{\parallel} = p_{\parallel\gamma_2} - \left(\frac{eff_{\gamma_1}}{eff_{\gamma_2}} \right) p_{\parallel\gamma_1}, \quad (6.2)$$

where the state emitting γ_1 is fed by γ_2 , $p_{\parallel\gamma_1}$ and $p_{\parallel\gamma_2}$ are the parallel momentum distributions obtained from gating on γ_1 and γ_2 respectively. This procedure was performed for the $E_x = 1010$ keV state, which is fed from above by the 971 keV γ -ray. However

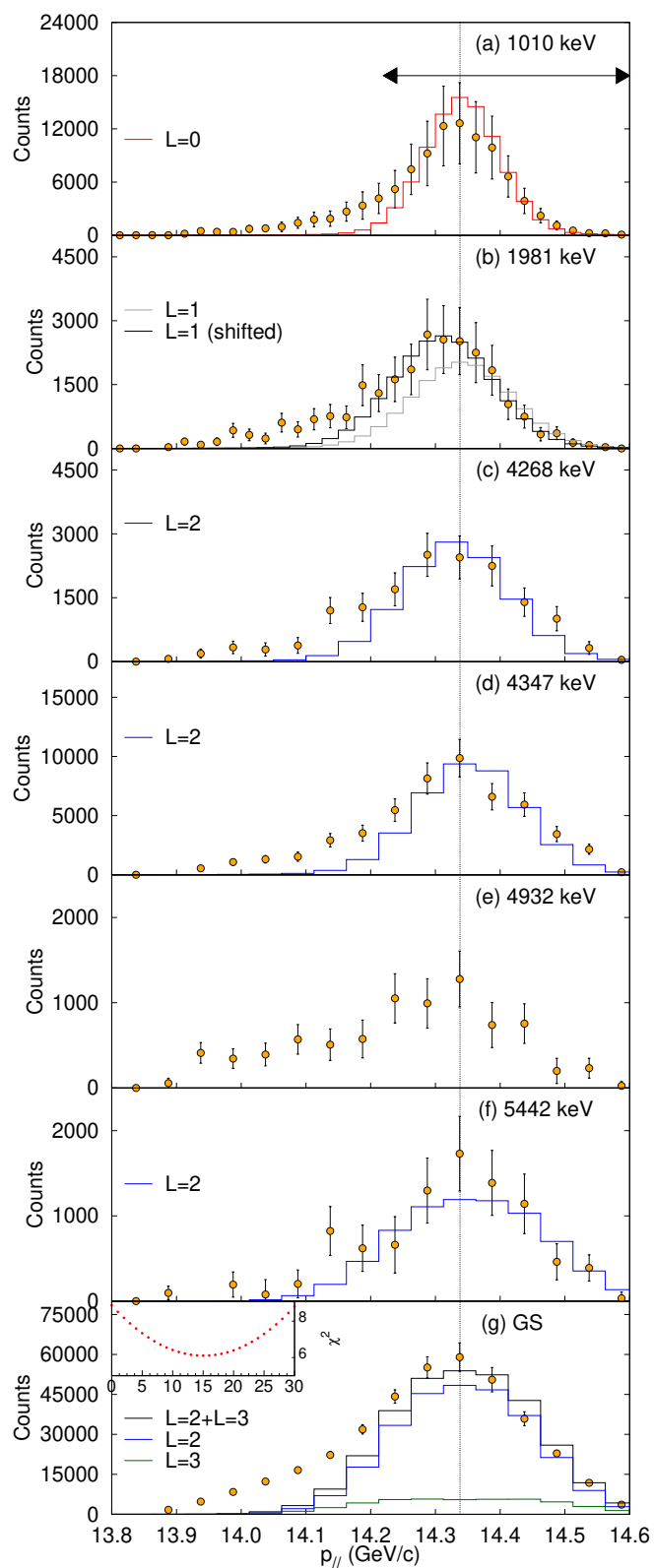


Figure 6.4: Experimental parallel momentum distributions for ${}^{33}\text{Si}$ determined by gating on γ -rays with fits from theoretical calculations using different L values. The horizontal arrow shows the range in which the fit was considered.

this was not feasible for the $E_x = 3159$ keV state which de-excites by the 1724 keV and 1773 keV γ -rays, due to limited statistics. The parallel momentum distribution for the $E_x = 4931$ keV state was obtained from gating on the 1773 keV γ -ray. The centroid of the distribution for the state at $E_x = 1981$ keV, is shifted by 0.1 GeV/c to lower momenta, suggesting that the $3/2^-$ state may not be exclusively populated by direct neutron knockout. The contribution of $\ell = 3$ and $\ell = 2$ were included in the final fit to the final ground state distributions using the following function [23]:

$$p_{\parallel exp}(0keV) = a_2 p_{\parallel th}(0keV, \ell = 2) + a_3 p_{\parallel th}(1435keV, \ell = 3), \quad (6.3)$$

with:

$$\begin{aligned} b'_f(0keV) &= a_2 b_f(0keV) \\ b'_f(1435keV) &= b_f(1435keV) + a_3 b_f(0keV) \\ b'_f(1435keV) &= (0.13 \times 51.9) - 0.2 - 1.1 = 5.45\%, \end{aligned}$$

where a_2 and a_3 represent the best fit parameters for the $\ell = 2$ and $\ell = 3$ contributions respectively and these allow for the final ground state parallel momentum distribution to be adjusted taking into account the contribution of the isomer. The variable $p_{\parallel exp}$ is the experimental distribution and $p_{\parallel th}$ is the theoretical distribution as predicted by the Glauber model [28]. The resulting distribution $p_{\parallel exp}$ is fitted to the experimental distribution. The ideal or most suitable contributions are determined by performing a χ^2 evaluation as shown in the insert of Figure 6.4 panel (g), assuming a_3 can take possible values between 0 and 100%. The $\ell=3$ contribution was found to be 5.45% of the ground-state distribution.

6.1.4 Evaluation of least squares in fitting theoretical distributions

In the analysis of the ${}^{34}\text{Si}(-1n){}^{33}\text{Si}$ data, experimental parallel momentum distributions were obtained and compared with theoretical predictions from the MOMDIS code [30]. In the fitting procedure the low-energy tail (assumed to be as a result of dissipative processes or target inelastic excitation [65]) was excluded as indicated in Figure 6.4 by the horizontal arrow. The amplitude and centroid of the theoretical distributions are allowed to vary as free parameters. This allowed the evaluation of the effect of changing the amplitude and centroid in the procedure of obtaining the best fit. The amplitude and centroid were varied and the resulting χ^2 values computed. The amplitude and centroid corresponding to the smallest χ^2 values were used to fit the experimental distributions. The ℓ value chosen is the one with the lowest χ^2 value.

Table 6.1: Energy, spin (j) and parity (π), population fraction b_f , single particle cross sections σ_{sp} and partial cross sections of final states populated in the ${}^{34}\text{Si}(-1n){}^{33}\text{Si}$ reaction together with spectroscopic factors C^2S_{exp} deduced from the present work and as quoted by [66].

Energy [keV]	j^π	ℓ	b_f^1 [%]	$\sigma_{inc} \times b_f$	σ_{sp} [mb]	C^2S_{exp}	C^2S Ref. [66]
0	$\frac{3}{2}^+$	2	50.8 (55)	58.9 (71)	15.1	3.90 (47)	4.5 (7)
1010(1)	$\frac{1}{2}^+$	0	22.8 (7)	26.4 (16)	19.7	1.34 (8)	2.0 (3)
1435(1)	$\frac{7}{2}^-$	3	9.0 (54)	10.4 (62)	14.4	0.72 (43) ²	
1981(1)	$\frac{3}{2}^-$	1	4.5 (6)	5.2 (6)	14.6	0.35 (4) ²	
4268(4)	$(\frac{5}{2}^+)$	2	1.7 (3)	2.0 (3)	13.3	0.15 (3)	
4347(4)	$(\frac{5}{2}^+)$	2	7.6 (5)	8.8 (6)	13.3	0.66 (5)	1.3 (4)
5442(6)	$(\frac{5}{2}^+)$	2	1.1 (3)	1.2 (4)	12.6	0.10 (3) ³	

¹Values all normalized to 100% of the one-neutron removal reaction.

²Upper limit assuming that these states are only populated by one-neutron knockout.

³Lower limit based on observed γ transition from state above S_n .

Table 6.1 shows calculations to obtain partial cross sections, single particle cross sections σ_{sp} and spectroscopic factors C^2S_{exp} . The values of σ_{sp} are taken from MOMDIS calculations, σ_{inc} is the inclusive cross section, b_f denotes branching ratio for the final state f as determined from γ -ray spectroscopy and the values for C^2S are obtained using:

$$C^2S_{exp} = \frac{b_f \sigma_{exp}^{inc}}{\sigma_{sp}}. \quad (6.4)$$

6.1.5 Spectroscopic Factors

The spectroscopic factor value C^2S_{exp} for the ground state is 3.90(47) and is close to 4 and hence consistent with an almost fully occupied $d_{3/2}$ orbital. However, we cannot determine with enough accuracy that the $d_{3/2}$ orbital is fully occupied, therefore it was necessary to investigate the upper shells. The large uncertainty associated with the ground state C^2S_{exp} value comes from the subtraction of the feeding from upper states. The $7/2^-$ and $3/2^-$ valence states at $E_x = 1435$ keV and 1981 keV, respectively, with C^2S_{exp} values of 0.72(43) [$7/2^-$] and 0.35(5) [$3/2^-$]. These values are indicative of a rather large neutron occupation of the $p_{3/2}$ and $f_{7/2}$ orbits. By summing the two fractions of pairs this implies there is an average of 1 neutron above the sd shell.

The $1/2^+$ state at $E_x = 1010$ keV is created by an $\ell = 0$ neutron removal from the $s_{1/2}$ orbit. The $1/2^+$ state has a corresponding C^2S_{exp} value of 1.34(4) which is less than the expected full occupancy value of 2 for a $s_{1/2}$ orbit. The $9/2^-$ and $11/2^-$ states originate from the recoupling of a 2^+ state from the $d_{3/2}$ pair with a neutron in $f_{7/2}$.

The $d_{5/2}$ is well below the Fermi surface so it is partially fragmented and hence not a single state. There are three $5/2^+$ states that have been identified at $E_x = 4268$ keV, 4347 keV and 5442 keV corresponding to a summed C^2S_{exp} value of 0.91(5). It is highly

probable that the $d_{5/2}$ sub-shell is fully occupied, but due to it being fragmented this cannot be concluded. The $5/2^+$ state originate from a particle excitation from a hole in the $d_{5/2}$ orbit. The $5/2^+$ state at 5442 keV is unbound and has a low C^2S_{exp} value of 0.10(3), but at this energy it should be noted that not all the branching is attributed to the γ -decay. If we assume this is indeed a $5/2^+$ state, which is likely as it has an $\ell = 2$ assignment, then using such a hypothesis corresponds to a M1 transition.

6.2 ${}^9\text{Be}({}^{36}\text{S}, {}^{35}\text{S}+\gamma)\text{X}$

Prior to this work ${}^{35}\text{S}$ has been studied using different approaches such as β^- decay studies [67], (d, p) reaction [68], (n, γ) [69], stripping reactions [70, 71, 72] and a pickup reaction from a ${}^{37}\text{Cl}$ target in [73]. However ${}^{35}\text{S}$ has not been studied using a knockout reaction and the spin and parity assignments available are tentative. Therefore, in this study the aim was to rule out some ambiguities in the spin and parity assignments.

6.2.1 Inclusive Cross section

The inclusive cross section from the ${}^{36}\text{S}(-1n)$ reaction was computed in a similar manner as described for the ${}^{34}\text{Si}(-1n)$ reaction. The ${}^{36}\text{S}$ beam had a corresponding purity of $P = 84.7\%$ and T/ϵ_{OBJ} ratio = 0.923. A total of $N_{OBJ}^{SC} = 2.76 \times 10^9$ incident nuclei was registered and this has an associated number of ${}^{36}\text{S}$ incident nuclei of $N_i = 2.16 \times 10^9$. The E1 scintillator registered a total of 1.08×10^7 nuclei for $f_{TOF} = 87.6\%$ and $f_p = 20.4\%$. This corresponds to a number of final knockout product residues of ${}^{35}\text{S}$ to be $N_f = 1.93 \times 10^6$.

The resulting inclusive cross section for ${}^{36}\text{S}(-1n){}^{35}\text{S}$ was 134(4) mb. The value obtained

for σ_{inc} is higher than that of the ${}^{34}\text{Si}(-1n){}^{33}\text{Si}$ reaction with $\sigma_{inc} = 116(6)$ mb. This is unexpected because the separation energy of ${}^{36}\text{S}$ is at $S_n = 9889$ keV compared to ${}^{34}\text{Si}(-1n)$ which has a corresponding separation energy $S_n = 7514$ keV [41]. Because the separation energy of ${}^{36}\text{S}$ is higher, one would expect this to translate to it being more difficult to remove a neutron therefore the cross section associated with a neutron removal reaction in ${}^{36}\text{S}$ should be less compared to ${}^{34}\text{Si}$. As such it may be anticipated that the cross section for the neutron knockout has to be lower for ${}^{36}\text{S}(-1n)$.

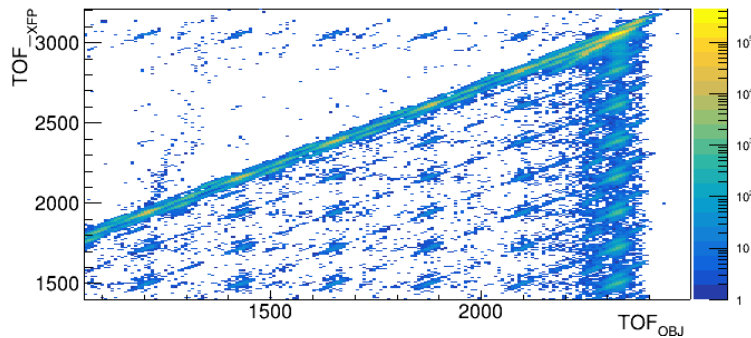
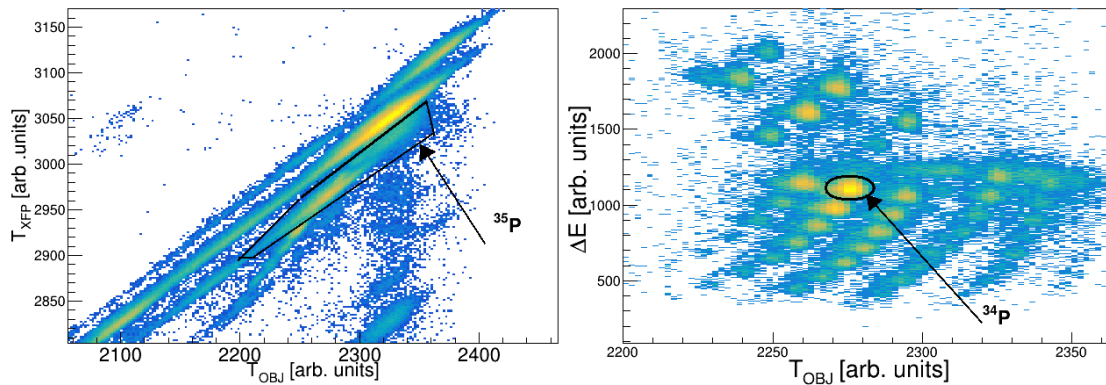


Figure 6.5: PID plot for identifying the incoming beam and indicating the repetitions seen for the ${}^{36}\text{S}$ beam and $(-1n)$ setting.

In the XFP-OBJ TOF matrices repetitions in the blobs were observed as shown in Figure 6.5. It is suspected that the repetitions correspond to uncorrelated events. This is a situation whereby one nucleus can trigger in the focal plane but does not interact either in the XFP or OBJ scintillator. For the 2 beam settings the following nuclei were included in the cocktail beam for ${}^{34}\text{Si}$: (${}^{33}\text{Al}$, ${}^{34}\text{Si}$ and ${}^{35}\text{P}$) and similarly for ${}^{36}\text{S}$: (${}^{35}\text{P}$, ${}^{36}\text{S}$ and ${}^{37}\text{Cl}$). To get an idea of how much the registered events were affected, the ${}^{35}\text{P}(-1n)$ reaction channel was used which is common to both ${}^{34}\text{Si}$ and ${}^{36}\text{S}$ incoming beams (shown in Figure 6.6). In principle the value for σ_{inc} obtained from both beam settings should be the same. The ratio of $\sigma_{inc} = \frac{N({}^{34}\text{P})}{N({}^{35}\text{P})} \times \frac{1}{nx}$ for the two different beam settings and hence correction factor is 0.5 as taken from Ref [23]. The value of the σ_{inc} was re-normalized to 67(4) mb using a correction factor of 0.5.



(a) PID plot for identifying ${}^{35}\text{P}$ incoming beam. (b) PID plot for identifying the ${}^{34}\text{P}$ residue.

Figure 6.6: Particle identification plots to identify the incoming beam and knockout residues for the ${}^{36}\text{S}(-1n)$ settings. This plot shows the selection for the ${}^{35}\text{P}$ incoming beam and ${}^{34}\text{P}$ knockout residue

6.2.2 Level Scheme

A level scheme was built with the aid of $\gamma\gamma$ coincidences, and events collected using all GREYINA modules in add-back mode. Similar to the ${}^{34}\text{Si}(-1n)$ reaction, there was an isomer (1.02 ns) which is the 1990 keV state whose γ -ray could not be observed because it either decays far from the GREYINA modules a distance of 1.5 m downstream of the reaction target prohibiting a reconstruction of the emission angle γ . The level scheme has been constructed taking into account previously reported coincidences while the spin and parities are consistent with assignments made by Ref. [70].

6.2.3 Momentum distributions

Assignments of orbital angular momentum were made by comparing the experimental distributions to theoretical predictions [28] as shown in Figure 6.9. The states at $E_x =$

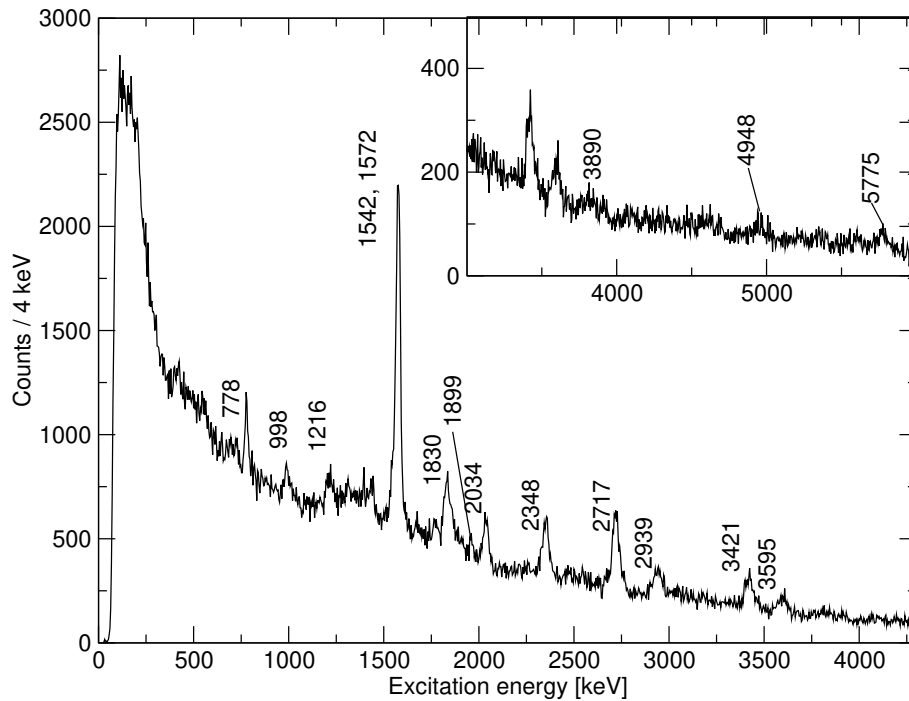


Figure 6.7: Add-back, Doppler corrected spectra showing γ -rays observed in this work for ${}^{35}\text{S}$.

1572 keV and 3890 keV are assigned orbital angular momentum $\ell = 0$. The state at $E_x = 2348$ keV is assigned $\ell = 1$ while the states at $E_x = 0$ keV, 2717 keV, 3421 keV, 3595 keV and 4025 keV are all assigned $\ell = 2$. The state at 3818 keV is assigned an orbital momentum of $\ell = 3$.

The ground state momentum distribution of ${}^{35}\text{S}$ is not fully in agreement with the theoretical prediction from the Glauber model. This is due to the fact that, as in the case of ${}^{34}\text{Si}$, it is contaminated by contributions from the isomeric state at $E_x = 1990$ keV whose γ -ray was not observed. It was therefore necessary to investigate the contribution of $\ell = 3$ and account for it in a similar manner as was done for ${}^{34}\text{Si}$. It was accounted for using:

$$p_{\parallel exp}(0\text{keV}) = a_2 p_{\parallel th}(0\text{keV}, \ell = 2) + a_3 p_{\parallel th}(1990\text{keV}, \ell = 3), \quad (6.5)$$

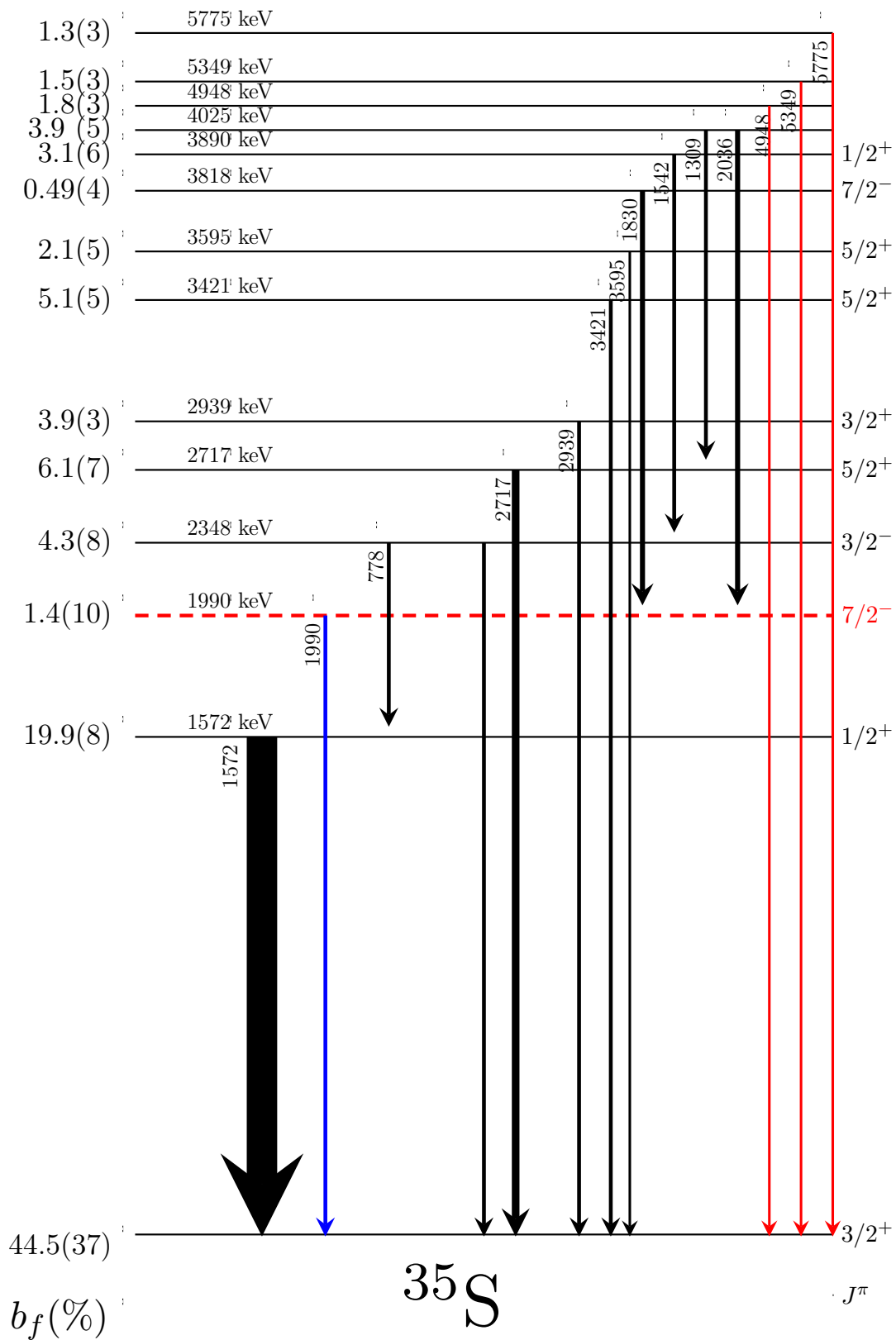


Figure 6.8: Level scheme for ${}^{35}\text{S}$ from this work. The blue transition represents the 1990 keV isomer, the transitions in black correspond to states which have corresponding parallel momentum distributions while the red transitions correspond states where it was not possible to extract parallel momentum distributions due to low statistics.

Table 6.2: Energy, spin(j) and parity (π), population fraction b_f , single particle cross sections σ_{sp} and partial cross sections of final states populated in the ${}^{36}\text{S}(-1n){}^{35}\text{S}$ reaction.

Energy [keV]	J^π	ℓ	b_f^1 [%]	$\sigma_{inc} \times b_f$	σ_{sp} [mb]	$C^2 S_{exp}$
0	$\frac{3}{2}^+$	2	44.5(37)	29.8(5)	13.1	3.33(76)
1572(1)	$\frac{1}{2}^+$	0	19.9(8)	13.3(6)	16.1	1.26(25)
1990	$\frac{7}{2}^-$	3	1.41(10)	0.9(5)	12.7	0.11(20)
2348(1)	$\frac{3}{2}^-$	1	4.33(8)	2.9(5)	13.1	0.34(1)
2717(2)	$\frac{5}{2}^+$	2	6.14(7)	4.1(5)	11.4	0.56(12)
2939(2)	$\frac{3}{2}^+$	2	3.99(3)	2.7(2)	13.5	0.31(6)
3421(2)	$\frac{5}{2}^+$	2	5.08(5)	3.4(3)	11.0	0.49(11)
3595(5)	-	2	2.13(5)	1.4(3)	11.0	0.21(6)
3818(5)	$\frac{7}{2}^-$	3	0.49(4)	0.3(2)	11.8	0.25(7)
3890(4)	$\frac{1}{2}^+$	0	3.09(6)	2.1(4)	13.5	0.29(9)
4025(4)	-	2	3.98(5)	2.7(4)	12.1	0.34(9)
4948(5)	-	-	1.8(3)	1.2(2)	-	-
5349(8)	-	-	1.5(3)	1.0(2)	-	-
5775(4)	-	-	1.1(3)	0.7(1)	-	-

¹Values all normalized to 100% of the one-neutron removal reaction.

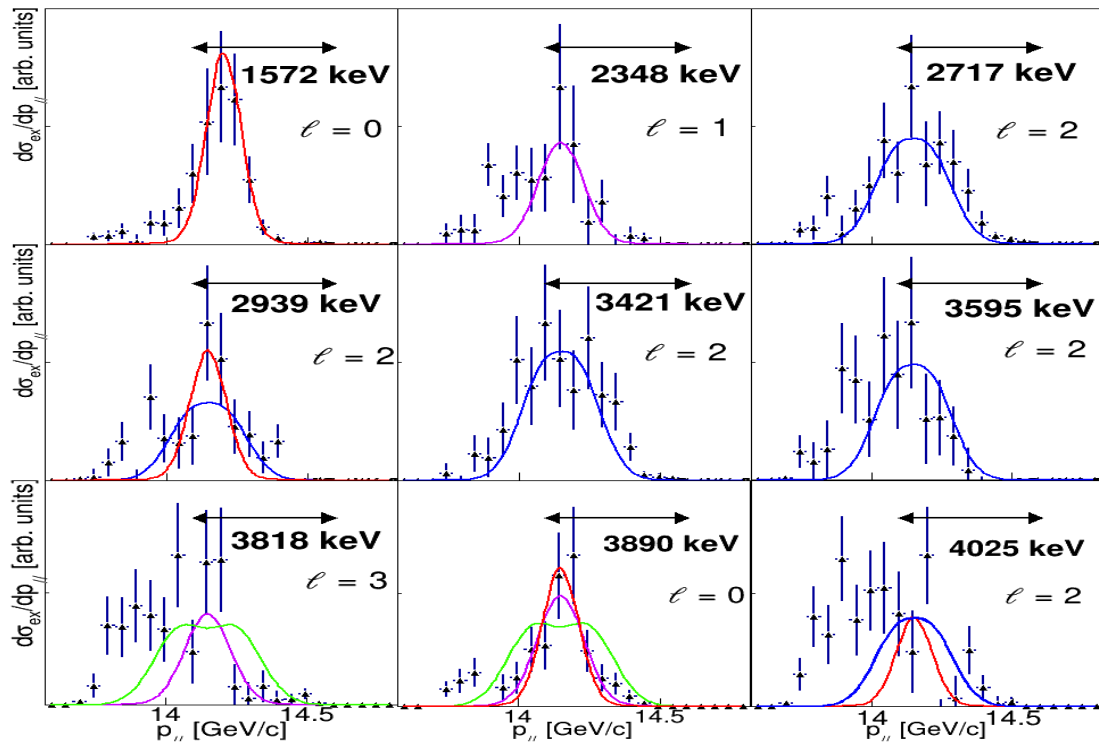


Figure 6.9: Experimental parallel momentum distributions for ${}^{35}\text{S}$ determined by gating of γ -rays as indicated in the panels. Fits from theoretical calculations using different ℓ values are shown as solid lines.

where the parameters a_2 and a_3 represent the $\ell = 2$ and $\ell = 3$ contributions respectively, while $p_{||exp}$ is the experimental distribution and $p_{||th}$ is the theoretical distribution as predicted by theory [28]. The fit showing the different contributions is shown in Figure 6.10.

The resulting distribution $p_{||exp}$ is fitted to the experimental distribution. The ideal or most suitable contributions are determined by performing a χ^2 evaluation (shown in Figure 6.11) assuming $\ell = 3$ can contribute any fraction between 0 and 100% corresponding to the value of a_3 . The calculated branching of the 1990 keV state was computed as follows:

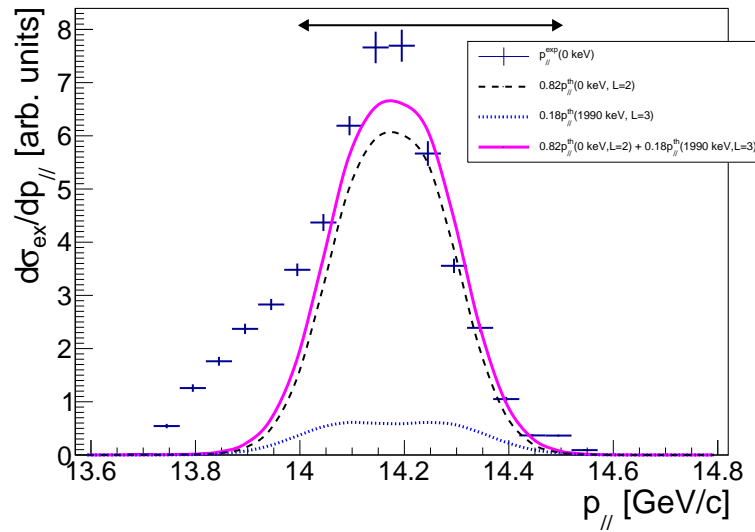


Figure 6.10: Ground state experimental distribution fitted with the $\ell = 2$, 18 % of $\ell = 3$ 1990 keV and a combination of both theoretical predictions (18% + 82%).

$$b'_f(0\text{keV}) = a_2 b_f(0\text{keV})$$

$$b'_f(1990\text{keV}) = b_f(1990\text{keV}) + a_3 b_f(0\text{keV})$$

$$b'_f(1990\text{keV}) = (0.18 \times 44.5) - 3.9 - 2.7 = 1.41\%.$$

The discussion and interpretation of results for the knockout reactions will be discussed together with the results from the transfer reaction in Chapter 10.

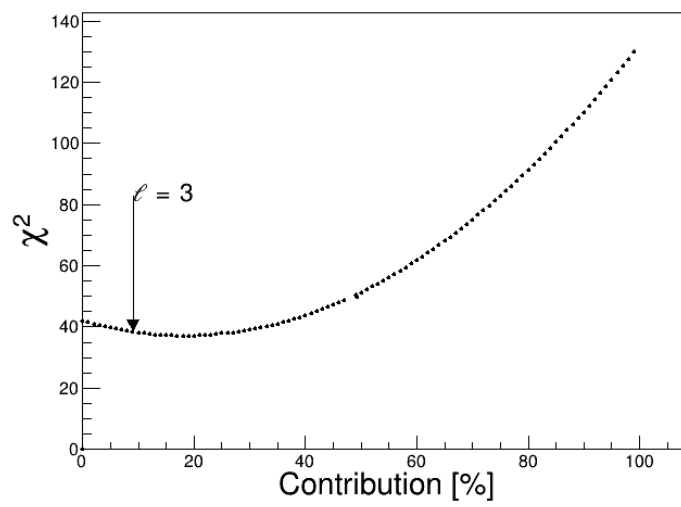


Figure 6.11: Evaluation of best contribution (corresponding to the lowest χ^2 value) compatible for the $\ell = 3$, 1990 keV isomer state to the final ground state parallel momentum distribution.

Part III

PART III: The iThemba LABS

$^{36}\text{S}(p,d)$ Experiment

7 | Experimental Details

In this chapter the experimental techniques used to collect data from the $^{36}\text{S}(p,d)^{35}\text{S}$ reaction are discussed. This experiment was performed in August 2019 at the iThemba Laboratory for Accelerator Based Sciences (LABS) facility in Cape Town (South Africa) using the K600 magnetic spectrometer [74]. A 66 MeV proton beam delivered by the Separated Sector Cyclotron (SSC) was incident on a 99.24% enriched ^{36}S target. First the beam production is described followed by the K600 magnetic spectrometer and its focal plane detection assembly. Finally the target system that was developed for this experiment is discussed.

7.1 Beam Production

The beam was produced using the K=200 Separated Sector Cyclotron (SSC) facility at iThemba LABS [75]. The SSC is the main accelerator facility at iThemba LABS and is used to deliver proton beams for radioactive isotope production as well as proton, neutron and heavy ion beams used for radio-biology and nuclear physics research. The SSC operates in conjunction with two solid pole injector cyclotrons namely SPC1 and SPC2. A schematic floor layout of the accelerators and corresponding beam lines is shown in Figure 7.1.

The beam to the SSC is supplied by either of the two injector cyclotrons. SPC1 is a K8 solid pole cyclotron and SPC2 is a K11 solid pole cyclotron [75]. The two cyclotrons are equipped with ion sources: SPC1 with an internal ion source which is the Penning Ionization Gauge (PIG) while SPC2 is equipped with two external ion sources, which are the electron cyclotron resonance (ECR) source and the polarized proton ion source [75]. For this experiment we made use of SPC1 and its PIG source, since it was convenient to use the standard proton beam that is produced for isotope production. The generated hydrogen ions are then pre-accelerated and thereafter extracted through the J-line so that they can be injected into the SSC. At the SSC the proton beam is then further accelerated to the desired energy of 66 MeV.

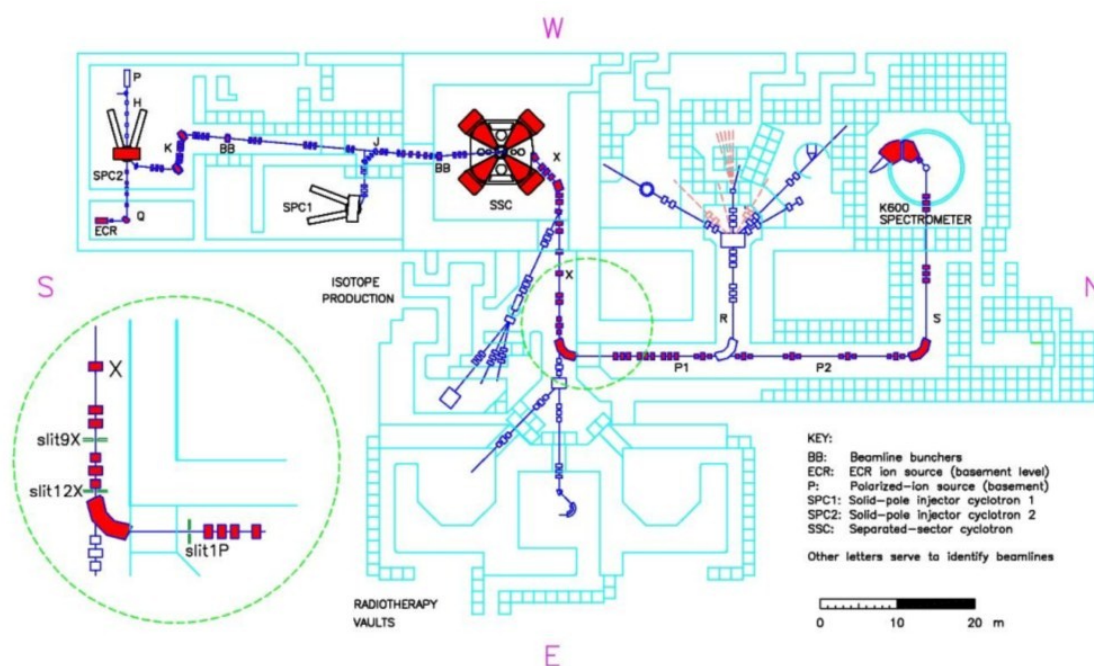


Figure 7.1: Schematic layout of the SSC facility at iThemba LABS.

7.2 K600 magnetic spectrometer Overview

The experiment was performed using the K600 spectrometer which is a QDD magnetic spectrometer consisting of five active elements namely: one quadrupole, two dipoles (D1 and D2) and two trim coils (K and H). The arrangements of these elements in the spectrometer is shown in Figure 7.2. The beam impinges on a target inside a scattering chamber positioned at the rotation axis of the K600. A target ladder at the center of the scattering chamber can house 6 targets in different vertical positions and is shown in Figure 7.4. The principle of operation of the K600 spectrometer is similar to the S800 explained in Chapter 4 in terms of physical separation of particles according to their respective rigidities.

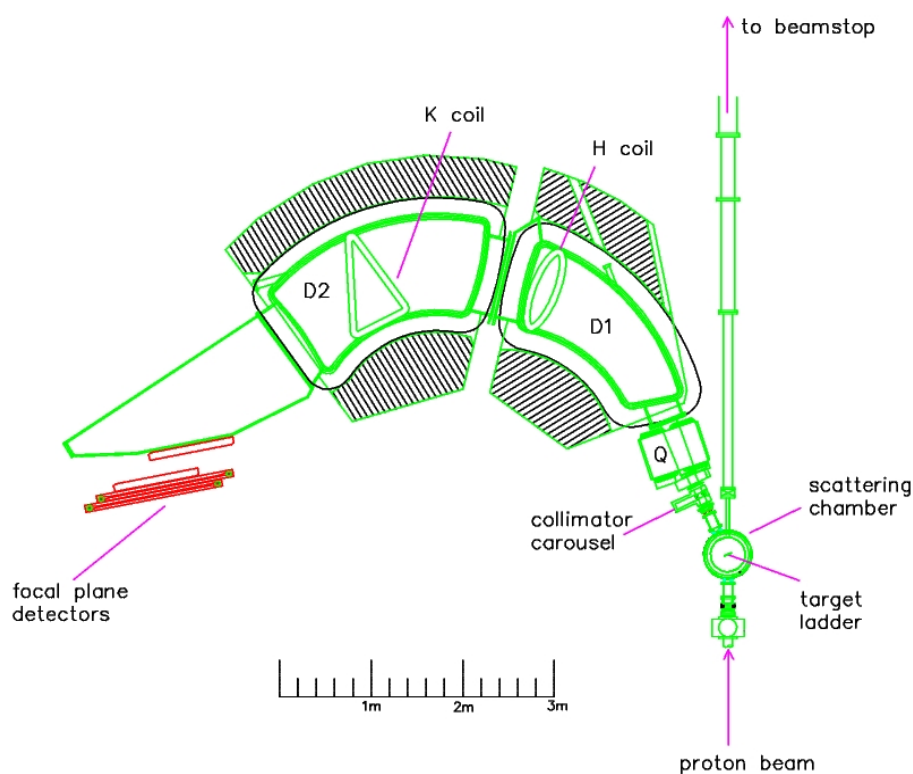


Figure 7.2: Schematic layout of the K600 magnetic spectrometer. It should be noted that for the current experiment the external beam stop was not used.

Once the reaction takes place the produced particles pass through a collimator that is housed in a collimator carousel that holds three different collimators and is located in front of the quadrupole magnet. The function of the quadrupole magnet is to focus the reaction products vertically while the two dipoles following it serve to arrange particles in the focal plane according to their rigidity [76]. The final focusing is achieved using the trim coils. The K coil compensates for changes of momentum as a function of the horizontal scattering angle ($x|\theta$), while the H coil serves to correct for second order aberrations ($x|\theta^2$). Particle beams from cyclotrons have an undesirable large momentum spread which introduces spectrum line broadening thereby resulting in poor energy resolution of the measurement. To correct for such an effect, dispersion matching [77] is employed. This is whereby the energy spread of the beam on the target is arranged in such a way that particle rays from a specific reaction is focused at a single point in the spectrometer focal plane [74].

In this experiment the K600 spectrometer was set to angles at $4^\circ, 7^\circ, 10^\circ, 15^\circ, 21^\circ$ and 28° . For angles in the range $7^\circ < \theta_{lab} < 28^\circ$ an internal beam stop inside the scattering chamber is used while for the angle at 4° a beam stop in front of the K600 quadrupole was used. The K600 spectrometer can, depending on the specifications of the experiment, be operated with the focal plane detectors in one of the three focal planes i.e, the low dispersion, medium dispersion or high dispersion focal plane. The low dispersion mode has not been used due to the limited energy resolution that can be obtained with it. The high energy dispersion mode accesses a limited momentum range and is more suitable for zero degree measurements. For the current experiment we made use of the medium dispersion focal plane. The focal plane detector package will be detailed in the next section.

7.2.1 Focal Plane Detector Packages

The focal plane detector array used in the medium dispersion focal plane constituted two multi-wire drift chambers (MWDC) and two plastics paddle scintillators. The MWDCs at iThemba LABS are of two types of configurations namely the XU vertical drift chamber (VDC) and the horizontal drift chambers (HDC) [76]. In the present experiment only the VDCs were used. It should also be noted that the naming convention for the drift chambers is due to the drift direction that the electrons follow in the chamber. For the VDCs the electrons drift perpendicular to the orientation of the signal wires while in the HDCs electrons drift parallel to the signal wires. In the X plane of the VDCs are 198 gold plated tungsten wires each $20\ \mu\text{m}$ in diameter and 4mm apart. Positioned in between these are 199 field shaping wires which are $50\ \mu\text{m}$ in diameter. Likewise the arrangement of the wires in the U plane is similar with 143 signal wires and 144 field wires separated by 4 mm but are slanted at 50° relative to the X wires, as shown in Figure 7.3. The two wire planes are sandwiched between Al cathode foils as indicated in Figure 7.3. Both the X and U wire planes are placed in a gaseous mixture with a composition of 90% Ar and 10% CO_2 . The gas is isolated from the atmosphere using two $25\ \mu\text{m}$ thick Mylar planes [76].

Particles enter the VDC and ionize the Ar gas producing electrons. The electrons drift towards the closest anode signal wires where avalanching takes place. The aluminum cathode foils are biased with a negative voltage of 3500 V and 500 V on the field shaping wires. When a particle traverses the VDCs at an angle of θ , charge is recorded in the X and U plane. Different drift distances are associated with different drift times due to the constant electron drift velocity. With all these parameters it is then possible to reconstruct the trajectory of the particles through the focal plane.

Two plastic scintillators, $1/4''$ and $1/2''$ thick respectively, are located in the focal plane,

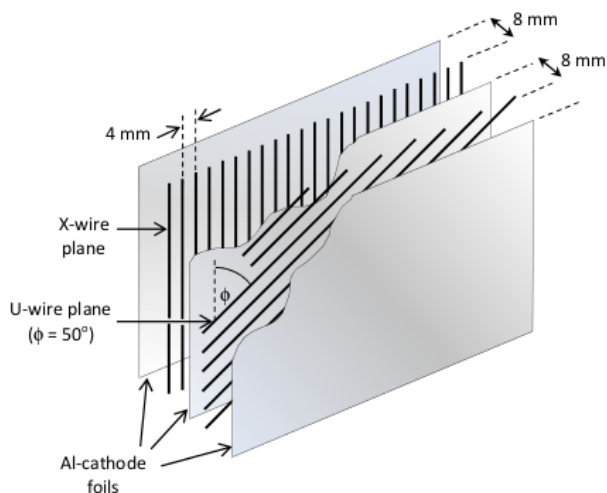


Figure 7.3: Illustration of the X and U wire plane wires in a VDC detectors at the K600 focal plane [76].

downstream from the VDCs. These are used typically for particle identification (PID) through $\Delta E - \Delta E$ or $\Delta E - E$ techniques, depending on the energy of the detected particles. The two scintillators also serve to create the event trigger for the data acquisition system (DAQ). In this experiment one plastic scintillator was used because the majority of the reaction products in this experiment are stopped within a few mm in the first scintillator. Therefore a combination of the total energy measured in the first scintillator and information on the time of flight (TOF) of particles through the K600 is used for PID purposes.

7.3 ^{36}S Target

Two different target ladders were used in this experiment. During the initial tuning phases of the experiment a standard target ladder with six positions was employed. Then for the measurement of the $^{36}\text{S}(p, d)^{35}\text{S}$ reaction a special sulfur target was developed,

which will be detailed below.

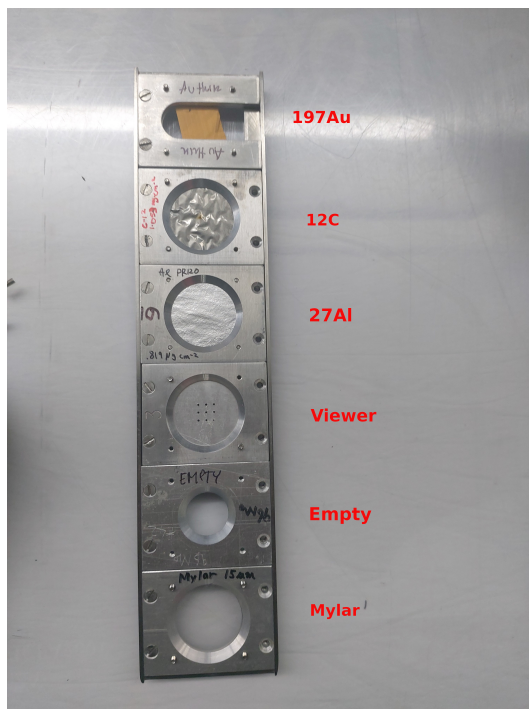


Figure 7.4: Target ladder used in the experiment with respective positions occupied by the indicated targets.

The standard target ladder consisted of the following targets: ^{197}Au (1 mg/cm^2), ^{12}C (1.053 mg/cm^2), ^{27}Al (0.819 mg/cm^2), Mylar ($\text{C}_{10} \text{H}_8 \text{O}_4$) (15 micron), a fluorescent ZnS beam viewer, and empty frame. The ^{197}Au and ^{12}C targets were used during the initial (p, p') tuning phases and energy resolution optimization phase of the experiment. The ^{27}Al target was used in scattering angle calibration procedures, with the $^{27}\text{Al}(p, d)$ reaction used to test the (p, d) mode prior to the installation of the special ^{36}S target system. The beam viewer, which is made from material that fluoresces when hit by the beam, was used to optimize beam steering and spot size on target, while the empty frame was instrumental in the periodic monitoring of the beam halo conditions and background checks.

7.3.1 Production of ^{36}S targets

Sulfur targets present certain challenges when used in direct reaction measurements. One major challenge is that they cannot be used as self-supporting targets because sulfur sublimates when subjected to energy deposition during beam bombardment. In previous studies [78] sulfur targets in the form of compounds such as silver sulfide and antimony sulfide were utilized. For a direct reaction such as a (p, d) reaction this is highly unsuitable as heavy contaminants lead to numerous unwanted states being populated that can obscure the sulfur states. To overcome these challenges a new method was developed to produce sulfur targets which is also at the same time cost effective. This is especially important when an experiment requires the use of less abundant isotopes of sulfur such as $^{33,34,36}\text{S}$, as they are very expensive (20 mg of ^{36}S at 8500 USD). The target used in this experiment, ^{36}S , has a natural abundance of only 0.01% and hence the high procurement cost may limit the amount of material that is available for an experiment. In addition a target with high purity (greater than 99% enrichment) is required for a direct reaction such as (p, d) . Standard production techniques are typically very wasteful and therefore not ideal.

7.3.2 Method of Production

Enriched ^{36}S in powder form was sourced from Isoflex with isotopic enrichment as indicated in Table 7.1. The presence of other contaminants is indicated in Table 7.2

Table 7.1: Isotopic Distribution

Isotope	^{32}S	^{33}S	^{34}S	^{36}S
Content (%)	0.07	0.05	0.64	99.24

^{36}S targets were produced by encapsulating 1 mg (2×10^{19} atoms/cm²) of enriched

Table 7.2: Chemical admixtures

Element	C	F	Mg	Si	Fe	Al	Mn	Ca	Cu	Co
Content ppm	750	530	<30	100	<30	<30	<30	<30	<30	<30

material in-between two Mylar foils, with a thickness of $0.5 \mu\text{m}$ equivalent to 3.43×10^{18} atoms/cm². The advantage of encapsulating ^{36}S in between the Mylar foils is that it prevents the loss of material to the vacuum due to sublimation as the ^{36}S is contained within a pocket of Mylar during beam exposure. To ensure a secure seal, the two Mylar foils were melted together by applying heat on the foils using a temperature controlled cylinder. Careful attention was paid with respect to adjusting/selecting the temperature, to ensure that the foils stuck together while preventing the encapsulated sulfur from sublimating. This target is shown in Figure 7.5. The advantage of using Mylar as the material for encapsulation is that, the only contaminant peaks that appear in the spectra due to encapsulation are solely from C and O. These contaminants are well accounted for, discernible and simple to identify in the K600 magnetic spectrometer.

The frame used to support the Mylar foils consisted of two identical aluminum rings held together by M2.5 stainless steel screws. This is shown in Figure 7.5. The other holes in the target frame allow attachment to a swiveling system as shown in Figure 7.6. The swiveling system ensures exposure of a part of the target to the beam only for a short period of time, before the target is moved so that a different part of the target is exposed to the beam, thus minimizing sublimation. Prior to the $^{36}\text{S}(p,d)^{35}\text{S}$ experiment the feasibility of such targets was tested using less costly material, namely natural sulfur. The feasibility of such targets was tested using an Elastic Back Scattering (EBS) measurement.

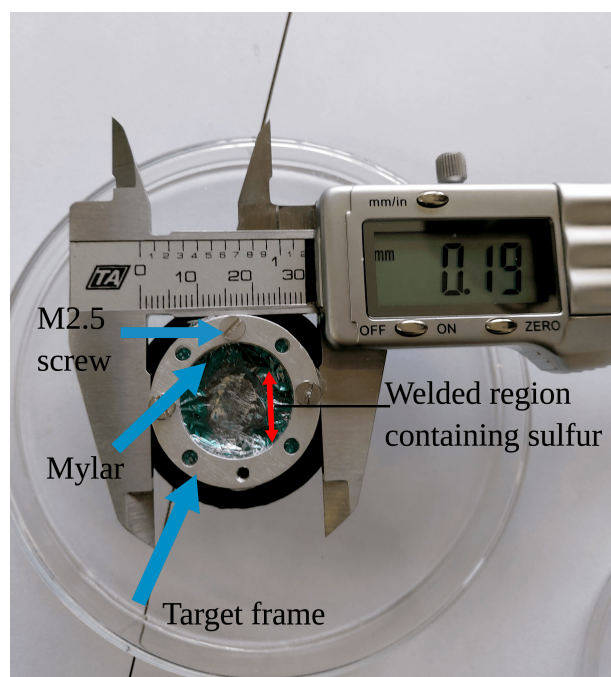


Figure 7.5: Target frame holding the encapsulated enriched ^{36}S .

7.3.3 Elastic backscattering spectrometry (EBS) characterization

The EBS experiment was performed at iThemba LABS at the Material Research Department, using a 3 MeV proton beam supplied from a Tandetron. The proton beam was incident on natural sulfur sandwiched between Mylar foils produced as described above. In order to detect the back scattered protons, a single silicon surface barrier detector was placed at $\theta_{lab} = 35^\circ$ relative to the beam axis. The scattering chamber and swiveling system is shown in Figure 7.6.

The target frame holding the target was connected to two independent motors and a spring. The motors mounted in the target chamber, were connected to the target via off-axis rods that caused a swiveling motion of the target by pulling the target, against the spring, at a 90° angle with respect to each other. This allowed the incident beam to irradiate all parts of the target. The motors were set up to move the target in regular

time intervals of 15 minutes to achieve homogeneous irradiation. The fact that the target was enclosed meant that any sulfur that did undergo sublimation would move to another place of the target, but still within the confines of the Mylar foils. The goal of the elastic back-scattering measurement was to determine how long the targets last and stays intact while exposed to 3 MeV protons. For the $^{36}\text{S}(p, d)^{35}\text{S}$ experiment using 66 MeV protons, less energy is deposited through beam energy loss and therefore the lifetime estimation using 3 MeV protons is considered to be a safe upper limit.

The disadvantage of this method is that the target thickness can vary drastically due to the presence of some large grains of sulfur within the Mylar. Unfortunately this could affect a cross section measurement where the target thickness needs to be known with more precision. Despite this drawback this method proved useful as a method was devised on how to normalize the varying target thickness (see discussion in Chapter 8 section 8.7.1).

To identify the different elements in the target sample a SIMNRA [79] analysis was performed. This is a simulation of charged particle spectra for ion beam analysis that was used to identify different elements in a sample. From the analysis it can be deduced that the thickness varies considerably from very thick (large grains) to no material. In this measurement the average thickness measured was $450 \mu\text{g}/\text{cm}^2$. It is expected that some material is lost during the process of applying heat to the Mylar foils. It was observed that the target lasts for approximately 48 hours when subject to continuous irradiation using 3 MeV proton beams with intensity of 6 nA. Target failure occurs when the integrity of the Mylar foil is compromised and the sulfur material is lost in the vacuum.

Figure 7.7 shows a scalar spectrum obtained from integrating the Rutherford Back-scattering peak corresponding to sulfur. The beam current intensity was 6 nA and was kept relatively constant within 10%. The amount of sulfur material decreased by 25%

during the course of irradiation. If we consider only heat deposition, based on SRIM calculations [80] using 3 MeV protons incident on 0.4 mg/cm^2 of natural sulfur, the energy deposited is 33.5 keV while the deposition corresponding to 66 MeV protons is 3.2 keV. It was found that the time it takes to lose 50 % of the target material is:

$$Days = \frac{\Delta E(3MeV) \times 6}{\Delta E(66MeV) \times 10}, \quad (7.1)$$

where $\Delta E(3 \text{ MeV})$ represents the energy loss for 1 proton with energy 3 MeV in 0.4 mg/cm^2 of sulfur while $\Delta E(66 \text{ MeV})$ represents the energy loss for 1 proton with energy 66 MeV in 0.4 mg/cm^2 of sulfur. Considering that heat deposition is solely responsible for loss of material through a compromised Mylar foil, it is estimated that a run of 6 days with 66 MeV protons, will reduce 50% of the target. The outcome of this study was published in Ref. [3].

7.3.4 ^{36}S target in K600 scattering chamber.

The same mechanism used to allow for target movement in the EBS measurements was installed inside the K600 scattering chamber in preparation for the $^{36}\text{S}(p, d)$ measurement. The setup is shown in Figure 7.8. Throughout the measurements the ^{36}S target moved to a new position every 60 seconds to achieve more exposure to each part of the target during irradiation. During the course of the experiment two different ^{36}S targets were used. The thickness of these ^{36}S targets were measured using the alpha energy loss technique, and were found to be 1 mg/cm^2 thick. The second ^{36}S target was necessitated by the fact that the Mylar windows on the original ^{36}S target became damaged after prolonged beam exposure, resulting in the eventual loss of ^{36}S material to vacuum due to sublimation. In addition a 1 mg/cm^2 thick natural sulfur target was also manufactured and used to acquire data at 7° and 15° with the aim to help identify possible contaminant

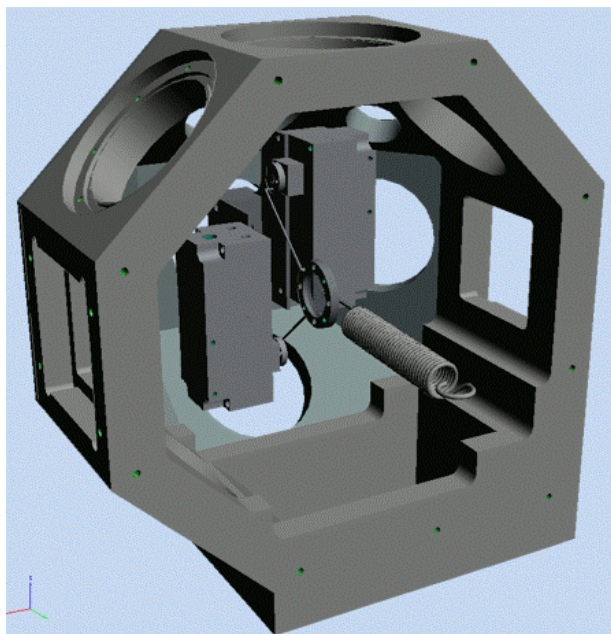


Figure 7.6: Technical drawing of the two-axis swiveling system to uniformly expose the target to the 3 MeV proton beam and hence energy deposition. The beam traverses the chamber from left to right. The sides and blanking flanges of the vacuum chamber are removed from the 3D drawing for viewing purposes.

states due to the presence of $^{32,33,34}\text{S}$. We also used a Mylar target made of equivalent thickness to identify the contribution of the contaminants from Mylar and the resolution of the peaks.

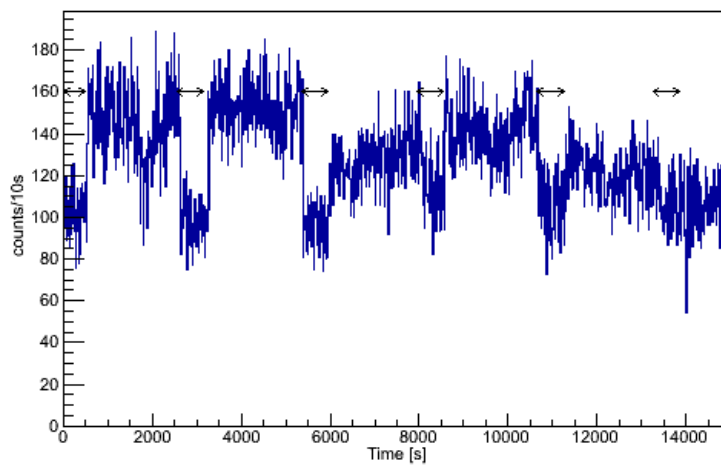


Figure 7.7: Scaler plot obtained for backscattered protons measured with energy between 2.45-2.65 MeV. The accumulated time is 4 hours at $I_b = 6$ nA, $E_b = 3$ MeV. The arrows indicate when the target is swiveling within the region comprising Mylar-Sulfur and Mylar only areas. The target positions are selected when high Sulfur spots are found.

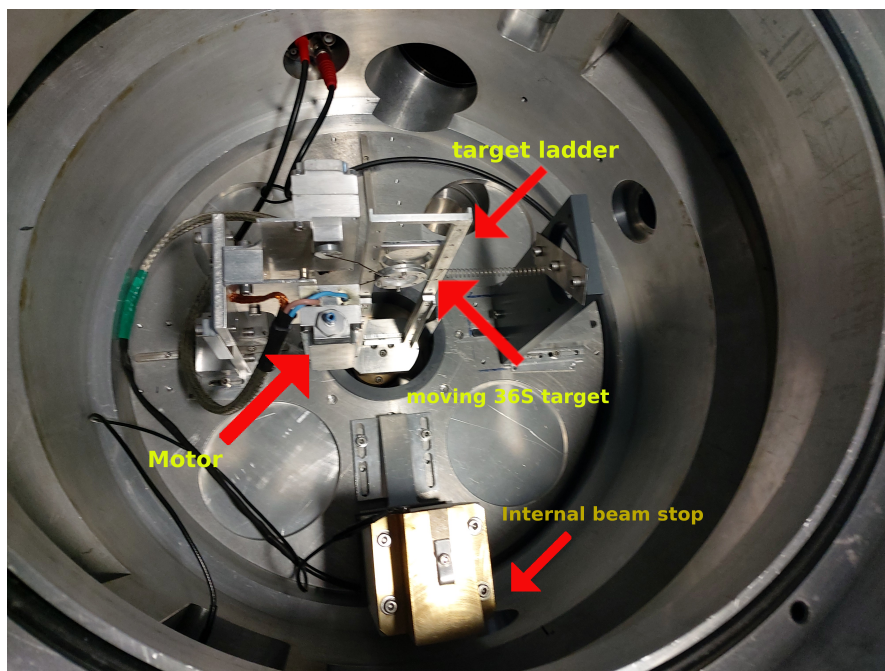


Figure 7.8: Implementation of the designed moving target system in the K600 spectrometer scattering chamber during the experiment.

8 | Analysis

8.1 Focal-Plane Particle Identification

Particle identification is performed so as to isolate charged particles of interest in the magnetic spectrometer. The information related to the particle's energy, mass or charge is provided using two methods: 1) their energy loss in the scintillator and 2) the TOF information. The energy loss of the particles is governed by the Bethe–Bloch formula which was detailed previously in Chapter 4. The pulse height signal of the scintillator carries this information. Particle identification is achieved using TOF information. Recalling that deuterons traverse the spectrometer under the influence of the Lorentz force:

$$\vec{F} = \vec{q}v \times \vec{B} \quad (8.1)$$

where v is the velocity of the particles with charge q in a magnetic field \vec{B} . Under the influence of this force the particles are constrained in a circular trajectory. The radius of the trajectory depends on the particles' rigidity defined as:

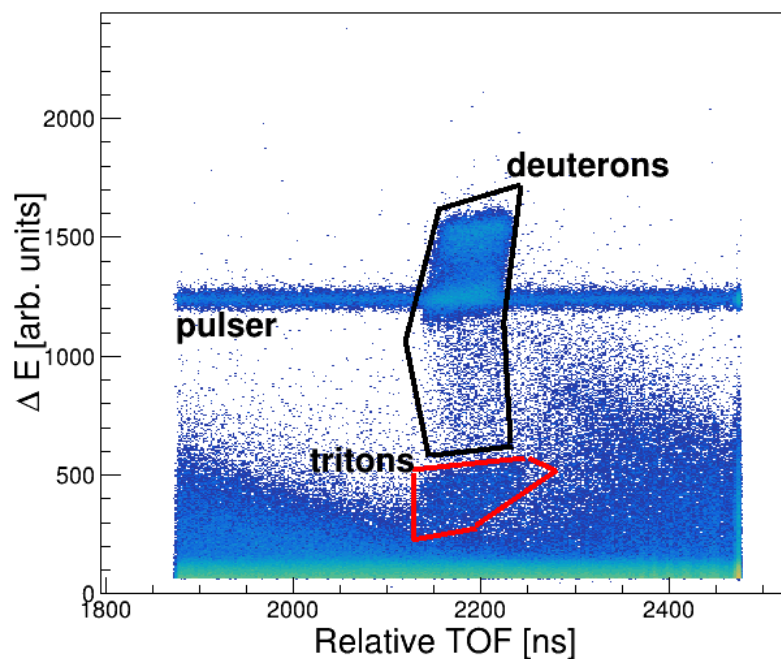


Figure 8.1: Particle identification spectrum of energy loss in the scintillator as a function of the relative TOF for the $^{36}\text{S}(p,d)$ reaction for data collected at $\theta_{lab} = 7^\circ$. There is a broad range of deuteron energies as a result of the deuterons having different incident energies (due to varying target thickness) in the scintillator resulting in different light output, see Figure 8.2.

$$B\rho = \frac{p}{q}. \quad (8.2)$$

The time-of-flight of the light particles depends on their flight path length as well as their velocity. Light particles having the same rigidity but different values of momentum and charge can therefore be distinguished by measuring their time-of-flight. Particle identification through TOF involves measuring the time elapsed between a radio frequency (RF) signal from the SSC and an event registered in the scintillator. Combining both the TOF and energy loss information, a two-dimensional histogram is obtained showing the loci of the reaction products as seen in Figure 8.1. In the data analysis, a software

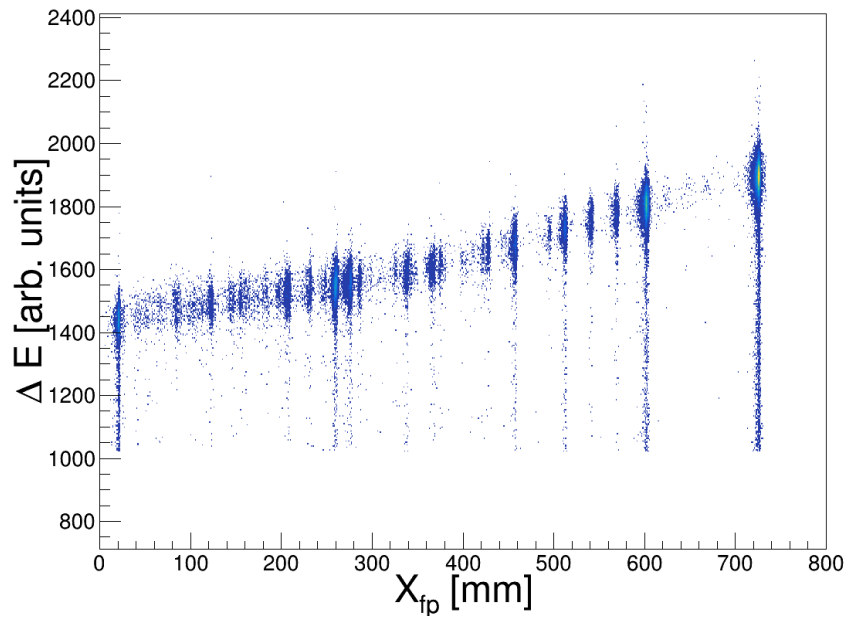


Figure 8.2: The light output in the scintillator depends on the energy of the incident deuterons in the scintillator. Their pulse heights are registered for different states produced in ^{35}S that appear at different focal plane position.

gate (using the ROOT software package [24]) is applied to select the proper region of interest shown in Figure 8.1.

8.2 VDC operation

The position of the deuteron in the focal plane is obtained using data collected from the VDCs. An event is considered valid when:

1. The scintillator received a signal,
2. More than 3 wires were fired per wire plane, but not more than 9,

3. The signal wires that fired should be neighbors.

An illustration of what happens in a case where a particle transversing the VDC results in three wires being triggered is illustrated in Figure 8.3. The position resolution is estimated by:

$$\Delta = \frac{|d_{i+1} - d_{i-1}|}{2} - d_i, \quad (8.3)$$

where the parameters d_{i-1} , d_i and d_{i+1} represents different drift distances for adjacent wires. In an ideal situation the quantity Δ should be zero. Non-zero values indicate inaccuracies in drift time measurements which translate to uncertainties in associated drift lengths. To obtain position information in the focal plane, measured drift times and hits in the wire positions are used. The drift time refers to the time elapsed between the first ionization (following incident particles), to the time where avalanching takes place in the drift cell. The drift times are converted to associated drift distances using a so-called Look-Up-Table (LUT) as shown in Figure 8.5. To correct the mapping of drift times to drift length LUT offsets are applied after checking a two-dimensional resolution spectra which relative positions in a drift cell. For all valid events the position X_{fp} is obtained by means of a ray-tracing algorithm [76] which obtains the crossing point in the wire planes using a least squares fit through valid (wire:drift distance) coordinates.

8.3 Calculation of Focal Plane Coordinates

In the beginning of an experiment it is advisable to acquire data for a reaction producing charged particles that illuminate the entire focal plane. In this way the average timing response of the signal wires in the VDC is obtained. The resulting drift times spectrum

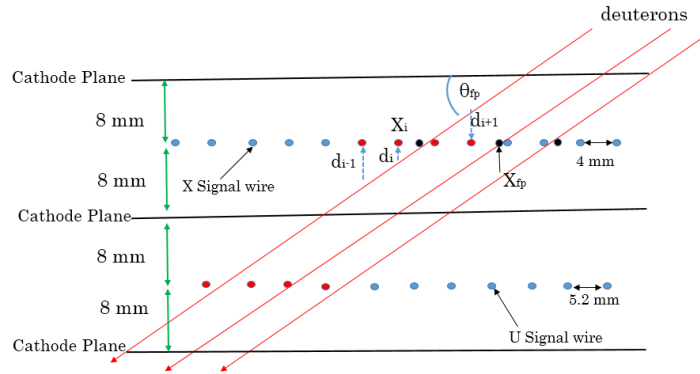


Figure 8.3: Schematic illustration of deuteron particles passing the wire plane in a VDC. The drift direction of the electrons towards the signal wires is shown. See text for details.

from reaction products illuminating the entire focal plane is called a “white spectrum”. It is preferable to use a white spectrum that does not contain a significant number of structures/peaks and it is necessary to use the same reaction producing the same particles of interest (i.e (p, d) in this case), so that a LUT is created for the right particles. The drift time spectrum used for this work is shown in Figure 8.4 and it must be noted that the absolute value of the horizontal (time) axis is of no consequence, but that the relative times are accurate. The x-axis times are read from right to left, with shorter drift times situated near the sharp peak and the flat region corresponding to deuterons with uniform velocity. The ionization takes place at a maximum distance of 8 mm from the wire plane. A drift cell (with guard wires) is associated with each signal wire to which electrons drift to form a measurable signal. The events per time bin are denoted as $\frac{dN}{dt}$ and once a drift time distribution is obtained, a corresponding drift length distribution can be obtained using [76]:

$$x(t) = \left(\frac{dN}{dx}\right)^{-1} \int_{t_i}^{t_f} \left(\frac{dN}{dt'}\right) dt', \quad (8.4)$$

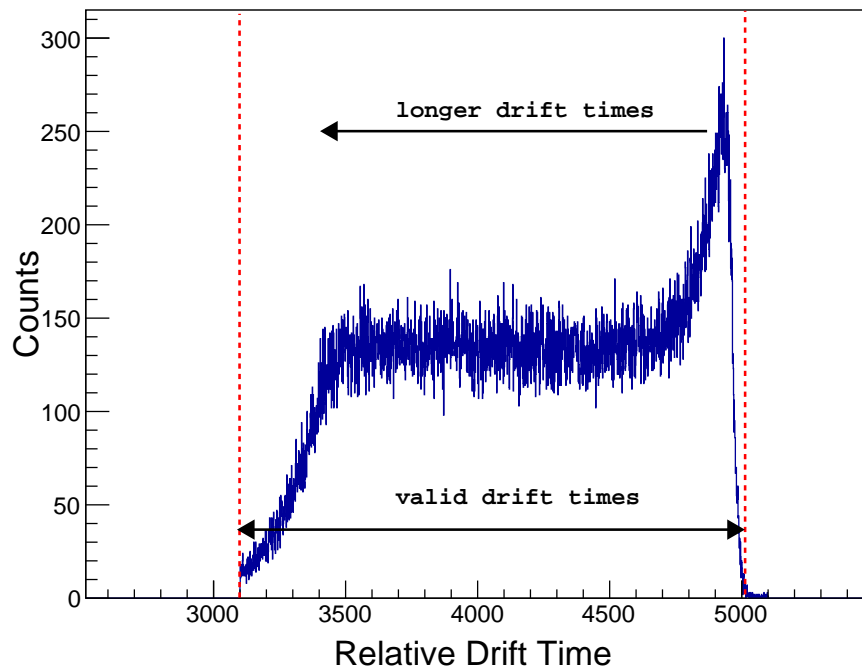


Figure 8.4: A typical drift time spectrum obtained using a white tune spectrum. Each time pin corresponds to 100 ps.

where t_i is the time the particle initially passes the drift cell, t_f refers to the time an anode registers a pulse, and $\frac{dN}{dx}$ refers to the drift length distribution in the cell. The LUT describes the mapping of drift times to drift length. A typical LUT spectrum generated by integrating the drift times is shown in Figure 8.5 together with a typical drift length spectrum shown in Figure 8.6.

As the deuterons traverse through the VDC, ionize the gas, and electrons start to drift, it takes some time for the electrons to reach the wires and a signal to be created for each wire. In the meantime, the deuterons will have reached the scintillator, which has a very fast response and creates a signal long before the electrons reach the wires. Strictly this scintillator-created signal is a "start" signal for a time measurement. Each signal from each of the wires can be considered a "stop" signal for a time measurement. However,

what is done during an experiments is to delay the paddle signal with a delay box so that it arrives at the TDC after the signal from the individual wires. Therefore when reading the time axis in the Figure 8.5 the time is read from right to left.

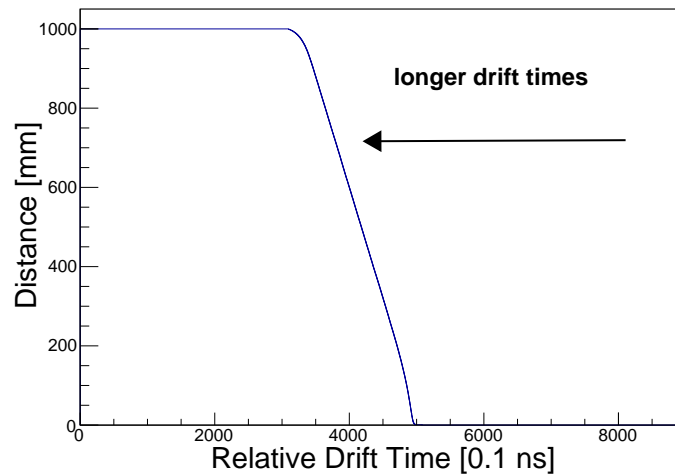


Figure 8.5: The lookup table used in the conversion of drift time to drift length. The true drifttime is calculated as: $\text{drifttime(in ns)} = -0.1 * x + 500$. The vertical axis value of 1000 represents 8mm.

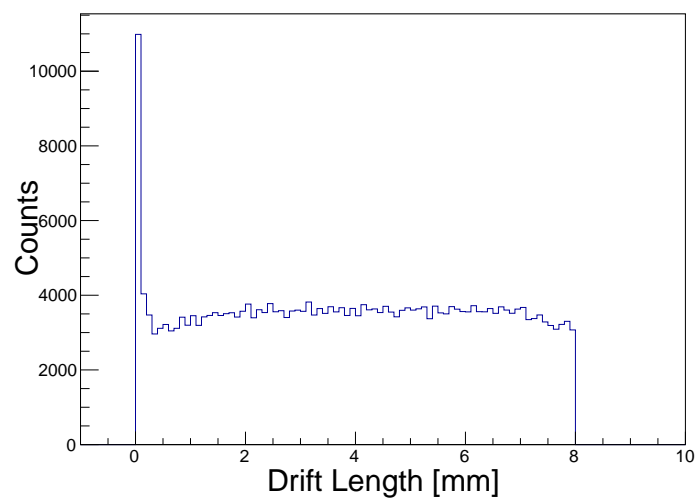


Figure 8.6: Converted TDC signals to corresponding drift length.

For a more detailed description on optimization procedures for good drift length deter-

mination, please refer to the K600 manual [76]. Once a drift length is associated to each drift time for the 3-9 wires hit per event, the focal plane coordinate associated with each event is determined by a simple regression analysis.

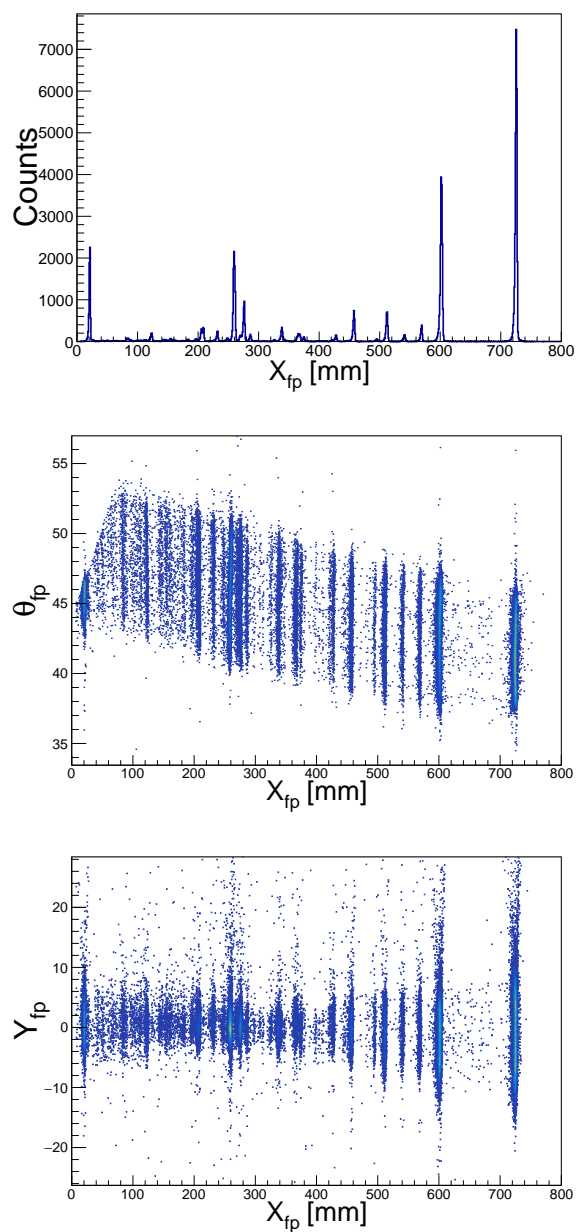


Figure 8.7: A sample selection showing the focal plane coordinates X_{fp} (mm), θ_{fp} (degrees) and Y_{fp} (mm) for the $^{36}\text{S}(p,d)$ reaction.

In addition to the horizontal focal plane position (X_{fp}), the ray tracing also provides information on the horizontal focal plane angle (θ_{fp}) of the particle track by employing the focal plane position information of two wire X-wire planes.

Finally by combining the information from the X-wire plane and a U-wire plane one can also determine the vertical coordinate (Y_{fp}) of the particle track in the focal plane. Figure 8.7 shows the focal plane coordinates X_{fp} , θ_{fp} and Y_{fp} for the $^{36}\text{S}(p,d)$ reaction.

8.4 Horizontal Angle Calibration

A multi-hole collimator referred to as the “pepperpot” and shown in Figure 8.8, is used to reconstruct the horizontal component of the scattering angle (θ_{scat}) from the measured focal plane angle (θ_{fp}).

Using the position of the holes on the collimator, it is possible to calibrate both the horizontal and vertical components of the scattering angle only if the K600 is operated in off-focus scattering mode. In this project, however, the ion optical mode used limits the angle calibration to the horizontal component. Data were acquired for four pepperpot runs. For each “pepperpot run” the magnetic field of the spectrometer was adjusted such that the inelastic peak from the $^{27}\text{Al}(p, p')$ reaction is at different focal plane positions.

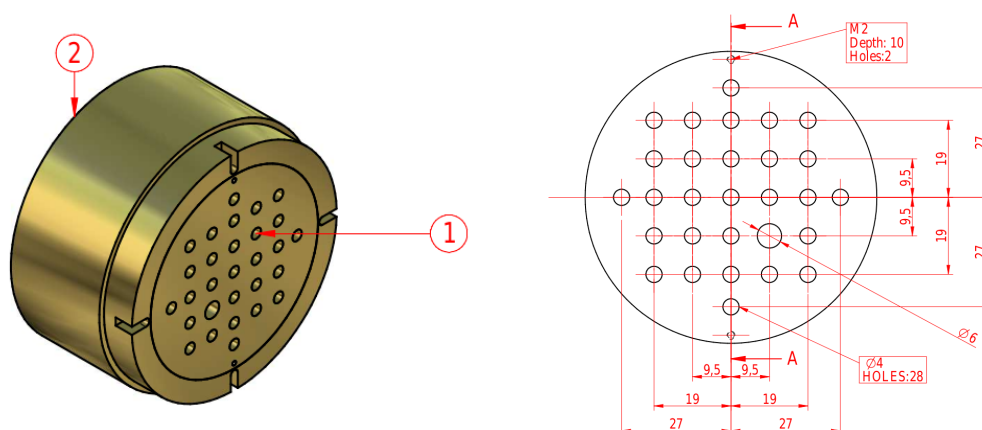


Figure 8.8: Technical drawing of the multihole pepperpot collimator used in the calibration of θ_{scat} . The collimator is positioned in a collimator carousel situated in front of the quadrupole as shown in Figure 7.2.

This is done to achieve angle calibration for the range of positions available between 0 – 800 mm. The resulting θ_{fp} spectra corresponding to different X1 positions has 7 peaks corresponding to the 7 vertical runs in the pepperpot. These peaks in each pepperpot run are fitted with a Gaussian to determine the value of θ_{fp} . Thereafter, a

calibration is performed to the known value θ_{scat} using the following equation [76]:

$$\theta_{scat} = (a_1 X_{fp} + a_0)\theta_{fp} + (b_1 X_{fp} + b_0), \quad (8.5)$$

where a_0 , a_1 , b_0 , b_1 are parameters obtained using the calibration procedure. Typical results of a θ_{scat} calibration is shown in Figure 8.9, which utilized the calibration equation (X_{fp} is in mm):

$$\theta_{scat} = (-0.361^\circ - (-5.656^\circ mm^{-1} \times 10^{-5})X_{fp})\theta_{fp} + (17.98^\circ - 0.001848^\circ mm^{-1}X_{fp}). \quad (8.6)$$

8.5 Improving energy resolution

Despite achieving corrections for aberrations using the K and H coils during the experiment, there are additional offline corrections required to achieve optimum resolution. This is due to a kinematic dependence of the momentum of the deuterons on the scattering angle and the vertical focal plane position Y_{fp} . This is clear when inspecting the two-dimensional histogram relating Y_{fp} or θ_{scat} to X_{fp} (shown in the bottom panels of Figure 8.7). It is therefore necessary to correct X_{fp} such that it is independent of Y_{fp} and θ_{scat} . The lineshape for θ_{scat} could have been performed using the TOF, but because in this experiment two VDCs were used, the correction was done using θ_{scat} . A TOF correction is only done in the absence of good angle information. This is the case whereby an experiment is performed with only 1 VDC, then there is no good angle information meaning the TOF information would be a poor substitute for angle. The long TOF means longer flight times that goes with bigger scattering angles, and conversely smaller

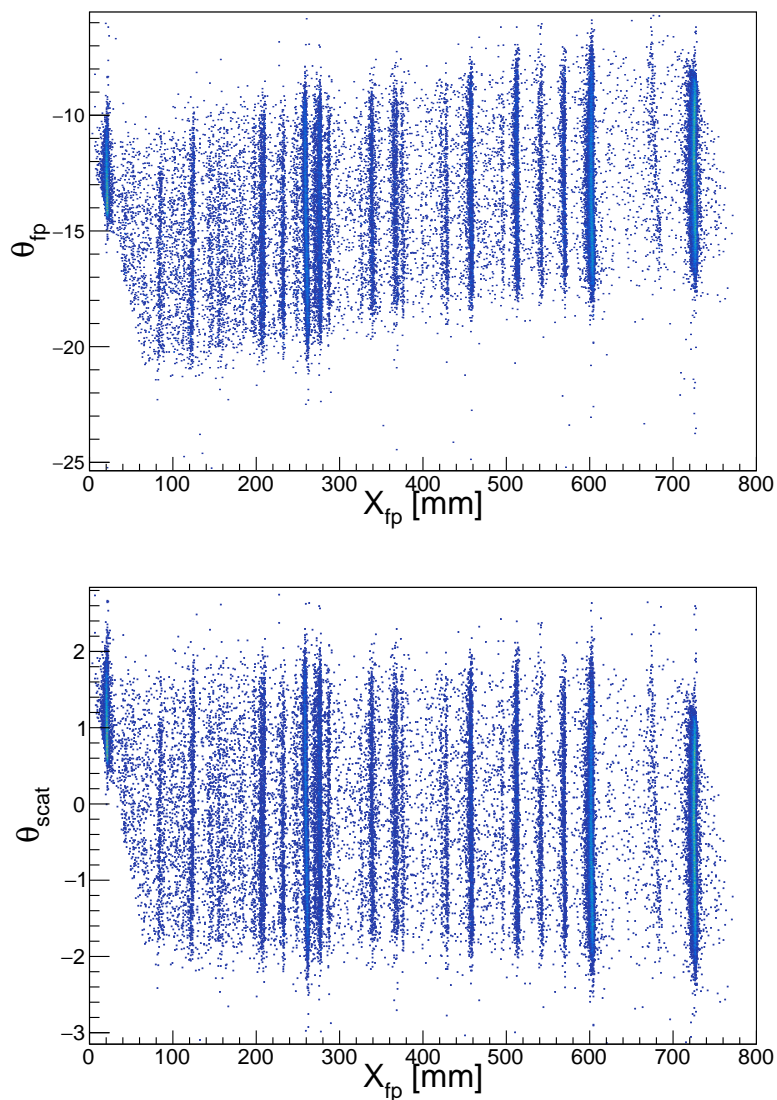


Figure 8.9: Two-dimensional histogram indicating θ_{scat} as a function of X_{fp} before (top) and after (bottom) calibration using the pepperpot.

TOF typically means a smaller arc and also smaller scattering angles. The correction was performed using the following equation [76]:

$$X_c = X_{fp} + \sum_{i=0}^5 c_i \theta_{scat}^i + \sum_{j=0}^2 d_j \theta_{scat}^j (X_{fp} - X_{offset}), \quad (8.7)$$

where X_c is the corrected position, c_i and d_j represent the correction coefficients obtained from a least squares fit. A very simple linear correction for Y_{fp} was employed as follows:

$$Y_c = Y_{fp} + \sum_i c_i Y_{fp}. \quad (8.8)$$

The effect of the lineshape correction is shown in Figure 8.10 while the result of resolution improvement can be seen in the focal plane position spectrum as a result of the correction is shown in Figure 8.11.

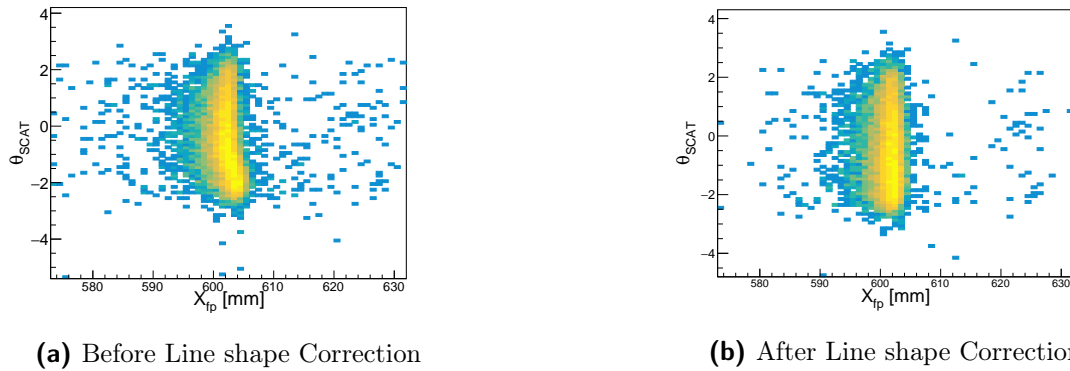


Figure 8.10: Lineshape Correction implementation to factor out dependence of θ_{scat} and Y_{fp} on X_{fp} .

8.6 Energy Calibration

The large number of states in ^{35}S are well established hence there was no need to use a calibration target. Using the information from Ref. [41] states could preliminary be

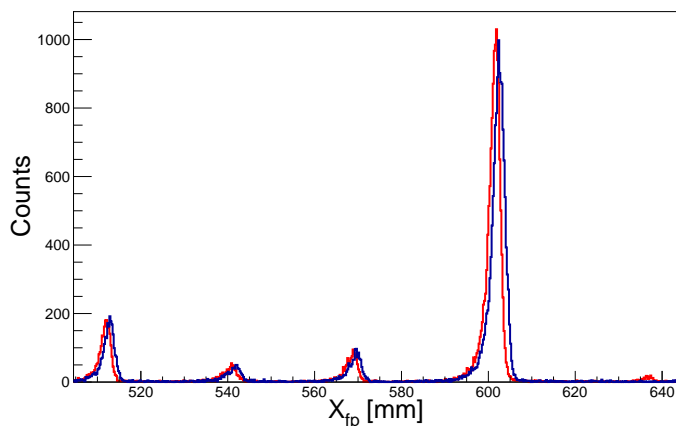


Figure 8.11: Focal position spectrum showing the resolution improvement. The blue (uncorrected) spectrum peak resolution corresponds to $\sigma = 1.4$ mm and the red (corrected) spectrum has a peak resolution of $\sigma = 1.2$ mm .

assigned to the different focal plane positions as indicated in Figure 8.12. The energy calibration involves two steps:

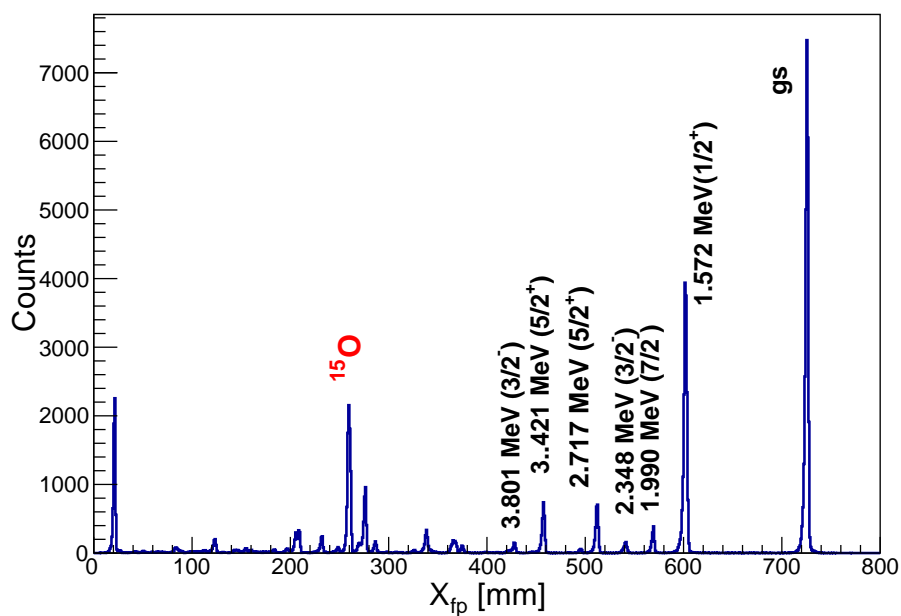


Figure 8.12: Focal position spectrum indicating the states were used for the energy calibration.

- **Rigidity Calibration:** Even though the states in ^{35}S will be used in the calibration, rigidity calibration has the advantage of allowing one to use contaminant peaks (e.g. ^{15}O) as calibration points, and is helpful in the identification of reactions on other sulfur isotopes. The rigidity ($B\rho$) was calculated using the two-body kinematics reaction code *Relkin*. The resulting rigidity values were associated with respective focal plane positions. There is a quadratic relation between the rigidity and focal plane position. The obtained rigidity values were plotted against the focal plane position and fitted with a second order polynomial:

$$B\rho = aX_c^2 + bX_c + d, \quad (8.9)$$

where $B\rho$ refers to the rigidity, X_c is the lineshape corrected focal plane position and a, b, d are the resulting parameters. The states used to calibrate are at $E_x = 0, 1.572, 1.991, 2.717, 3.421$ and 3.801 MeV. The choice of the states used to calibrate was motivated by the fact that they can be identified with certainty: through the pattern of excitation energy and absence of other states closeby (this is the case for the ground state and first five excited states) or states where the spin-parity and excitation energy are well known. In order to ensure the calibration holds for higher excitation energies, the state at $X_{fp} \approx 260$ mm, corresponding to the $^{16}\text{O}(\text{p,d})^{15}\text{O}$ ground state was used. The graph with the resulting fit is shown in Figure 8.13.

- **Kinematics Calculation:** The relation between the momentum and excitation energy is given by [81]:

$$E_x = E_0 + m_t + \sqrt{p_E^2 - m_E^2} - (p_p^2 + p_E^2 - 2p_p^2 p_E^2 \cos\theta + m_3^2)^{\frac{1}{2}}, \quad (8.10)$$

where the projectile, target, ejectile and recoil are represented by the subscripts

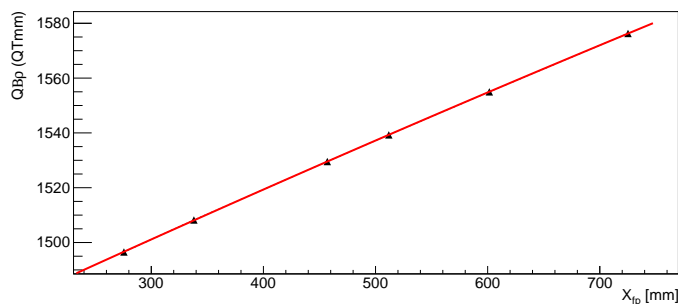


Figure 8.13: Second order polynomial fit of the rigidity as a function of the focal plane position X_{fp} for the measurement of the $^{36}\text{S}(p,d)$ reaction at $\theta_{lab} = 7^\circ$.

p, t, E and r , respectively. Through equation 8.10 a specific state can thus be associated with a rigidity value. From equation 8.2 we know that for $Z = 1$ particles, $B\rho = R = p$, so that equation 8.10 can be used to associate a value of E_x for every focal plane position.

The calibration was done per K600 angle setting and the resulting parameters obtained are shown in Table 8.1. For the well known states the difference between the values listed in Ref. [41] and the resulting extracted peak centroids differ at most by 10 keV.

Table 8.1: Rigidity calibration parameters for each angle setting.

Order	4°	7°	10°	15°	21°	28°
0	1437.8	1437.3	1436.8	1435.7	1433.1	1431.0
1	0.19286	0.19329	0.19322	0.19248	0.19303	0.19097
2	-1.5167e-5	-1.5254e-5	-1.5197e-5	-1.4617e-5	-1.4488e-5	-1.3888e-5

8.7 Differential Cross section

In order to determine the spin and parity of states in ^{35}S , it was necessary to compute differential cross sections at different angles for these states. It follows that the experimental differential cross section for a state is proportional to the ratio of the counts under the peak of interest and the target areal density. The experimental differential cross section in [mb/sr], related to a specific angle θ in the laboratory frame, was computed as:

$$\frac{d\sigma(\theta)}{d\Omega} = \left(\frac{10^{27}}{\rho} \right) \frac{N_c}{\epsilon N_0 \Delta\Omega}, \quad (8.11)$$

where:

- N_c represents the yield for a specific peak related to a state determined from focal plane spectra. For the free standing peaks without any significant background contributions (up to the state at 2.717 MeV), the number of counts in the peak was obtained from intergrated counts of the excitation energy histogram. For all the other states the number of counts in a peak of interest N_c was obtained by fitting the peak of interest with a convolution of a Gaussian and Landau function. The Gaussian function is given by:

$$G(x) = \frac{1}{\sigma\sqrt{2\pi}} e^{-\frac{x-\mu}{2\sigma^2}}, \quad (8.12)$$

where σ represents the standard deviation determined from the fit, and μ is the mean centroid of the peak. The Landau function [82] is given by:

$$L(x) = \frac{1}{\pi c} \int_{-\infty}^{\infty} e^{-t} \cos \left[t - \frac{x - \mu}{c} + \frac{2t}{\pi} \log \left(\frac{t}{c} \right) \right] dt, \quad (8.13)$$

where c is the scale parameter.

- The number of incident protons N_0 was determined using the total number of charge collected from the beam stop, which is obtained from the current integrator (CII) scaler reading using only inhibited events corrected for dead time:

$$N_0 = \frac{CII.R}{1000.Q_e}, \quad (8.14)$$

where CII represents the scaler readout events, R is the range set on the current integrator [in nA] and Q_e is the charge of an electron 1.602×10^{-10} nC.

- ϵ represents the VDC efficiency. The efficiency of the VDC is characterized by its ability to detect charged particles crossing the wire plane. If it is assumed that the scintillator is 100% efficient for focal plane charged particle collection, then for example the X1 wireplane, one has:

$$\epsilon_{X1} = \frac{\text{number of good events seen in X1}}{\text{number of PID selected events in scintillator}}. \quad (8.15)$$

where ϵ_{X1} is the efficiency corresponding to the individual wire in the X plane in one VDC. If the experiment makes use of more than one VDC then the resulting efficiency is a product of all the efficiencies in the individual wire planes.

- ρ refers to the total number of target nuclei per unit area. The target areal density was computed as follows:

$$\rho = \frac{N_A t_\rho}{A}, \quad (8.16)$$

where t_ρ is the target thickness in g/cm², N_A refers to the Avogadro constant and A is the mass number of the target nucleus.

- $\Delta\Omega$ is the solid angle of the K600 in *sr*.

The differential cross sections were calculated for each of the scattering angles, 4°, 7°, 10°, 15°, 21° and 28°. For strongly populated states each angle divided into 4 angular bins.

In the next chapters the experimental differential cross sections will be compared to the theoretical calculations. For a comparison between theory and experiment it is required that the cross section must be in the same frame of reference. For conversion from the laboratory frame to the center-of-mass frame, the following equations were used [83]:

$$\theta_{CM} = \sin^{-1}(\gamma \sin(\theta_{lab})) + \theta_{lab}, \quad (8.17)$$

$$\left(\frac{d\sigma(\theta)}{d\Omega} \right)_{CM} = \left(\frac{d\sigma(\theta)}{d\Omega} \right)_{LAB} \left(\frac{1 + \gamma \cos(\theta_{CM})}{(1 + 2\gamma \cos\theta_{CM} + \gamma^2)^{3/2}} \right), \quad (8.18)$$

where γ is obtained using:

$$\gamma = \sqrt{\frac{m_p m_E}{m_t m_r} \left(\frac{1}{1 + \frac{Q}{E_x}} \right)}, \quad (8.19)$$

where m_p, m_t, m_E, m_r correspond to the mass of the projectile, target, ejectile and recoil, respectively, while Q and E_x refer to the Q value of the reaction and excitation of the state, respectively.

8.7.1 Target thickness normalization

It is important to highlight that the $^{36}\text{S}(p,d)$ experiment made use of an unusual target setup. Assuming a target thickness for cross section calculations was a challenge due to the following factors:

- Throughout the measurement the target moved to a new position every 60 seconds. The movement covered an area slightly bigger than the actual size of the ^{36}S target material. Consequently the effective target thickness changed all the time from maximum thickness of ^{36}S all the way to only Mylar. This effect is shown in Figure 8.14.
- The target was getting slowly depleted over time and as a result the thickness decreased with time: the thickness measured at the end of the experiment through alpha energy loss was different from the thickness at the start of the weekend (1 mg/cm^2 compared to 0.6 mg/cm^2).
- For the $\theta_{lab} = 4^\circ$ K600 angle setting, a different target was used whose thickness varied differently from the first target used for all the other angle settings.

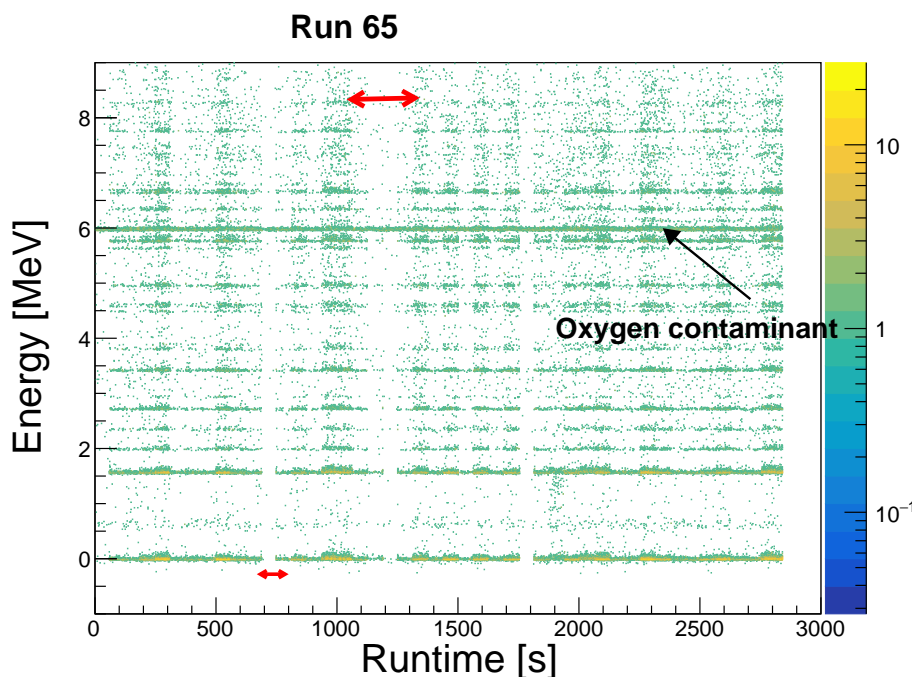


Figure 8.14: Excitation energy as a function of the runtime for one run. The red arrows indicate examples of regions where the beam is either on only Mylar foils or a region with only a small amount of ^{36}S .

The above mentioned problems were addressed by computing a normalization factor for each angle setting, to account for the varying target thickness. As an indication of the extent to which the target thickness varied, see Figure 8.15 which shows the CII normalized count rate as a function of time during a run, for the case of the ground state.

The method of extracting normalization factors was based on the assumption that the beam interacted with the maximum target thickness at those times when the CI corrected count rate is at a maximum. Therefore it is possible to calculate the ratio of the “actual” cross section (using only the data from the short time window where the rate is at a maximum) relative to the “average” cross section, where the data from the whole run is used.

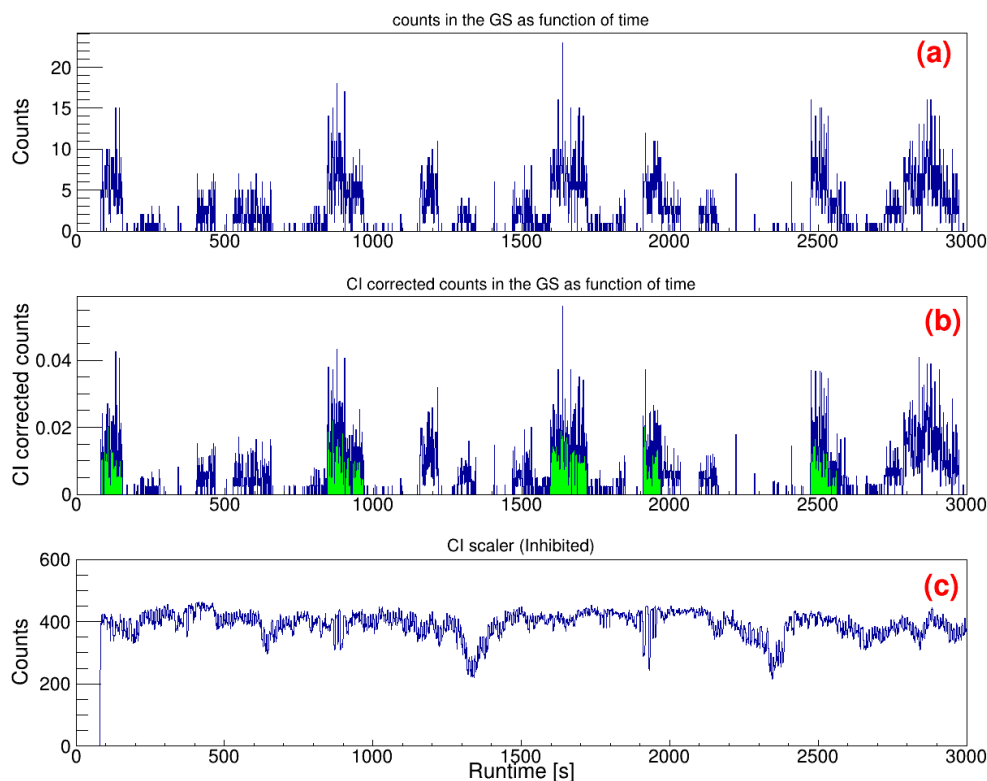


Figure 8.15: Spectra used to select regions where count rate was at maximum where (a) represents the counts for the groundstate (GS) as a function of time, (b) is the CI corrected spectra obtained by dividing the spectrum in panel (a) by the spectrum in panel (c). The spectrum in panel (c) represents the CI counts as a function of time. These regions are indicated in green and are associated with the maximum target thickness.

For each experiment run, a selection was made of up to 5 times during the run when the count rate is at or close to a maximum. The spectrum used in the selection is shown in Figure 8.15 panel (b). The selected times represent periods where it can be assumed that the beam was on maximum target thickness and therefore represents the actual cross section. For each of these the ratio of the counts divided by the summed CI value for that time period (approximately 55 seconds) is obtained. This reflects a value proportional to the actual cross section. This is then compared to the total counts during a run for that given state, divided by the corresponding CI value. As a result for each run an average

scaling factor is obtained (the 5 scaling factors divided by 5), and the standard deviation of the 5 scaling factors. The cross section values obtained for different angle settings are then normalized relative to the scaling factor of the 4° data set, and are as follows:

Table 8.2: Normalization factors

K600 angle	4°	7°	10°	15°	21°	28°
Scaling	1	1.91	1.92	2.63	2.48	2.62

The resulting standard deviation of these normalization factors is approximately 10% of the cross section. The 10% systematic error due to the target thickness complications was included in the error bar for the extracted cross section together with the statistical error, as will be detailed in the following section.

The largest contributors to the total error in cross section is that associated with the target thickness. The maximum error associated with the K600 spectrometer is 0.05° which is deduced by taking half of the smallest division unit. The statistical error is related to counts under a peak and is equal to $1/\sqrt{N}$. The statistical error is more significant at larger angles i.e 15°, 21° and 28° where lower statistics prevails and the cross section is relatively low.

9 | Results

In the following chapter the results of the $^{36}\text{S}(p,d)^{35}\text{S}$ one neutron pickup reaction experiment are presented and discussed. In addition the analysis results of a $^{40}\text{Ca}(p,d)^{39}\text{Ca}$ reaction from a previous study by Matoba *et.al*, [1] is presented. In particular for both nuclei, the identification of states, together with spin and parity assignments from comparisons with theoretical calculations are shown. In the last section the summed $s_{1/2}$, $p_{3/2}$, $d_{5/2}$, $d_{3/2}$, and $f_{7/2}$ strength and C^2S weighted energy values are discussed from the identified $\ell = 0, 1, 2, 3$ states. A comparison is presented between the two nuclei to characterize the Fermi surface (which of the nuclei ^{40}Ca or ^{36}S is the most magic and has the least $np - nh$ excitations into the fp shells), and the variation of the neutron $d_{3/2} - d_{5/2}$ spin-orbit splitting between the two nuclei mainly due to tensor forces.

9.1 Identification of ^{35}S states

In Figure 9.1 the energy calibrated spectra are shown for the $^{36}\text{S}(p,d)^{35}\text{S}$ reaction at 6 spectrometer angle settings available during the experiment. It is possible to subdivide the angular ranges into four subranges and still determine the intensities of the strongest peaks as shown in Figure 9.2. Before the cross section for these and the higher excitation energy states can be extracted, it is necessary to identify all the potential contaminant

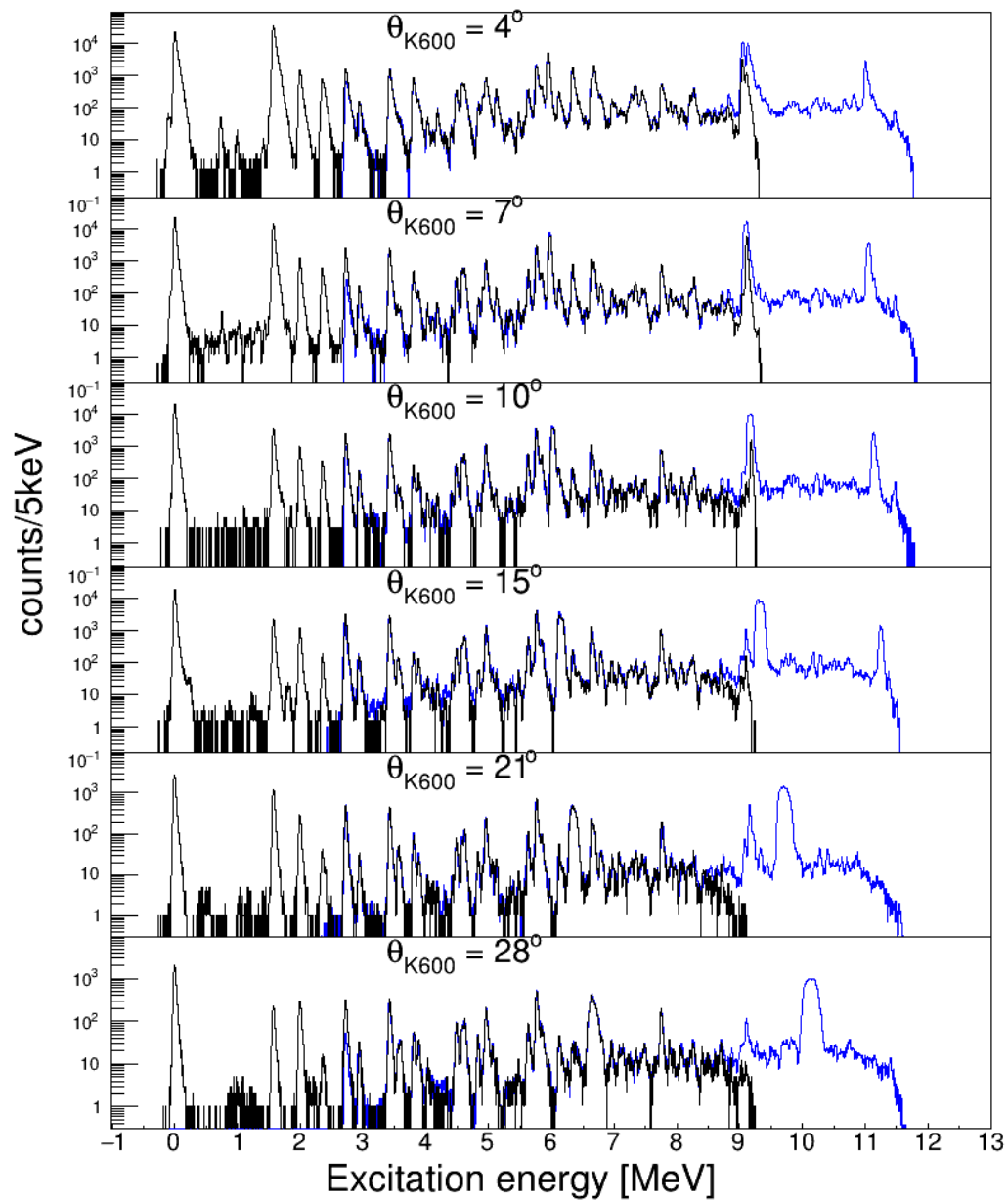


Figure 9.1: Excitation energy spectra for the $^{36}\text{S}(p,d)^{35}\text{S}$ reaction for the data collected at all K600 angle settings i.e. $\theta_{lab} = 4^\circ, 7^\circ, 10^\circ, 15^\circ, 21^\circ$ and 28° . In the black is the data collected at higher field setting and in blue is the data collected at lower field settings.

peaks.

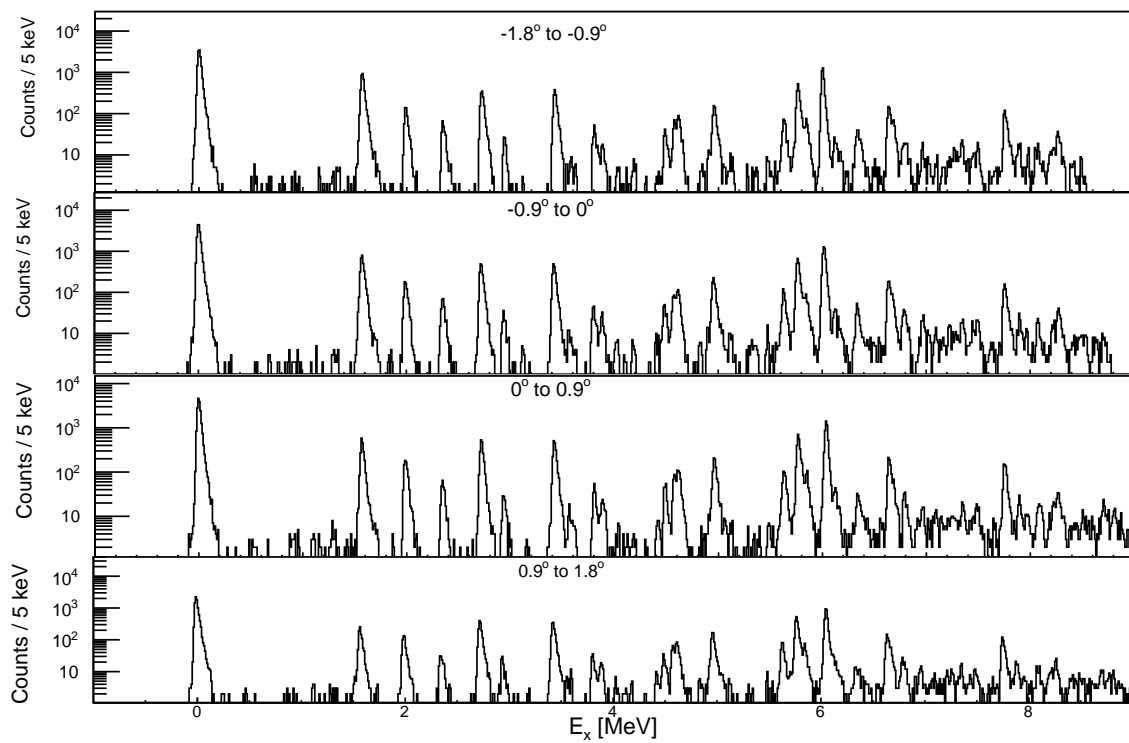


Figure 9.2: Excitation energy spectra representing data collected at one K600 angle $\theta = 10^\circ$ for the different 4 angle cuts made for each angle $[-1.8^\circ:-0.9^\circ]$, $[-0.9^\circ:0^\circ]$, $[0^\circ:0.9^\circ]$ and $[0.9^\circ:1.8^\circ]$.

Two different targets were used to investigate the background in the ^{35}S excitation energy spectra. A natural sulfur target with the same thickness (1 mg/cm^2) as the ^{36}S enriched target, also encapsulated in Mylar foils ($0.5\ \mu\text{m}$ thick), was used to identify states from $^{31,32,33}\text{S}$. Measurements for the $^{nat}\text{S}(p,d)$ reaction were taken at 7° and 15° . In addition data for Mylar only were also acquired at 7° and 15° . Excitation energy spectra for the ^{nat}S used and Mylar targets are shown in Figure 9.3 for the $\theta_{lab} = 7^\circ$ measurement. The excitation energies are given for the ^{35}S kinematics. The first two states of ^{35}S are observed and indicated in magenta. States for all sulfur isotopes are clearly observed: $^{31,32,33}\text{S}$.

The prominent states observed in Mylar are from (p,d) reaction with ^{12}C , ^{13}C and ^{16}O . It can be seen that the shape of the ^{15}O peak has a different shape in the Mylar spectrum as compared to the ^{nat}S spectrum. This is due to the fact that in the Mylar target there was no material in-between the foils that induced additional energy loss for either the protons or the deuterons escaping the target material.

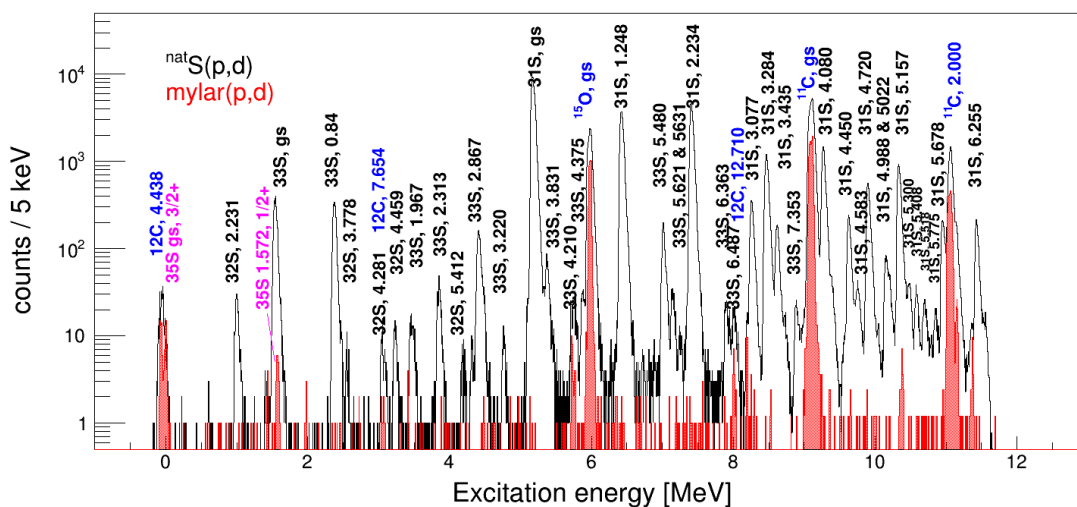


Figure 9.3: Spectrum representing states identified from a (p,d) reaction on Mylar (shown in red) and compared to the $^{nat}\text{S}(p,d)$ spectrum (black).

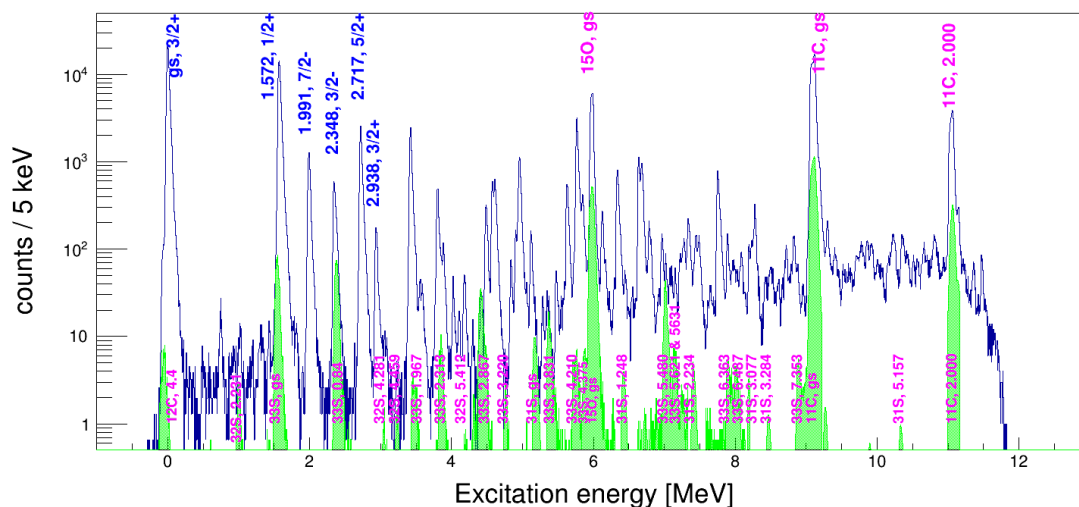
As discussed in section 7.3.2 the ^{36}S material was highly enriched. Consequently, we

expect a relatively low content of other sulfur isotopes in the ^{35}S spectrum. The only contaminant sulfur states that are free standing peaks in the ^{35}S excitation energy spectrum are the two ^{33}S states at 2.867 and 3.831 MeV. In order to account for contaminants from $^{31,32,33}\text{S}$, the ^{nat}S excitation energy spectrum was superimposed on the ^{35}S excitation energy spectrum. The ^{31}S and ^{32}S peaks were scaled to take account of the natural abundances of $^{31,32,33}\text{S}$ as reported by the manufacturer specifications. The resulting comparison is shown in Figure 9.4. We conclude that $^{31,32,33}\text{S}$ contaminants do not have a big influence on the extraction of ^{35}S information.

9.2 Cross section extraction

Now that the contaminant peaks are clearly identified, all the remaining peaks can now be assigned to E_x values and the process of extracting cross sections can be started. These cross sections are essential to provide angular distributions which will be used to assign spin and parity quantum numbers to these states. For the strongly populated states, angular distributions of each angle setting was subdivided into 4 angular bins and the respective spectra analyzed separately. Figure 9.2 shows a spectrum obtained as a result of dividing each of the $\theta_{lab}=10^\circ$ spectra into 4 angular bins by applying a gate condition on θ_{scat} . Figure 9.4 shows the ^{35}S excitation energy and all identified ^{35}S states. They are identified by the fact that they don't correspond to the Mylar- or $^{32,33,34}\text{S}$ -induced reactions. Otherwise only the few first states are identified with energies given.

It is important to determine the full peak strength with sufficient accuracy in order to obtain precise cross section values. For the first six excited states this can be achieved by integrating the peak. However for all the other states a fit is required to account for the overlapping states. This requires the need of an accurate determination of the canonical shape of the peaks. It can be seen in Figure 9.5 that there is a prominent high-energy



The peak shapes exhibit a dependence on excitation energy and θ_{K600} , as the energy loss will increase with excitation energy and increased target thickness due to larger scattering angles. It is evident that a Gaussian fit is not sufficient in reproducing the peak shape. As a result, in order to adequately account for the peak shape, a fit consisting of the convolution of a Gaussian and Landau function was used to fit states above 2.938 MeV and extract the areas of the peaks. As noted before, this was not necessary for the freestanding peaks below 2.9 MeV because here the density of states was very low and the states are clearly separated. The Gaussian and Landau parameters used for the available angle settings are given in Table 9.1.

For each data set representing a specific K600 angle the peak properties were obtained by fitting the freestanding low-lying excited states at 0, 1.572, 1.991, 2.348 and 2.717 MeV, allowing for small increases in the width of the states as excitation energy increases. At higher excitation energies the density of states is high, and sometimes partly obscures the peaks corresponding to ^{35}S , such that some cross sections could not be extracted. As an example, the peak at 6 MeV corresponding to interactions with the ^{16}O of the Mylar window is by far dominant. As a result some states around 6 MeV were not considered. The 4° data were acquired with a ^{36}S target that was different in thickness from the other measurements.

Table 9.1: Gaussian and Landau parameters obtained from fitting the first five excited states and used in fitting the remaining states above 2.938 MeV.

K600 angle	4°	7°	10°	15°	21°	28°
Gauss sigma	0.01482	0.01039	0.01113	0.01205	0.01258	0.01261
Landau Parameter	0.003139	0.003066	0.003034	0.002054	0.002146	0.002874

When fitting the excited states, excitation energy values were allowed to vary within a 10-20 keV range, and the Gaussian width and Landau spreading parameters could vary by 2% in the fit. A fixed background of 1 count per 5 keV bin was also added to the fit routine. An example of a typical fit for 20 peaks fitted simultaneously is

shown in Figure 9.6. The fit range for one peak was taken to be from 50 keV below the peak centroid, up to 150 keV above the peak centroid, as indicated in Figure 9.7. For consistency the integration range is the same as used for the free standing peaks below 2.9 MeV.

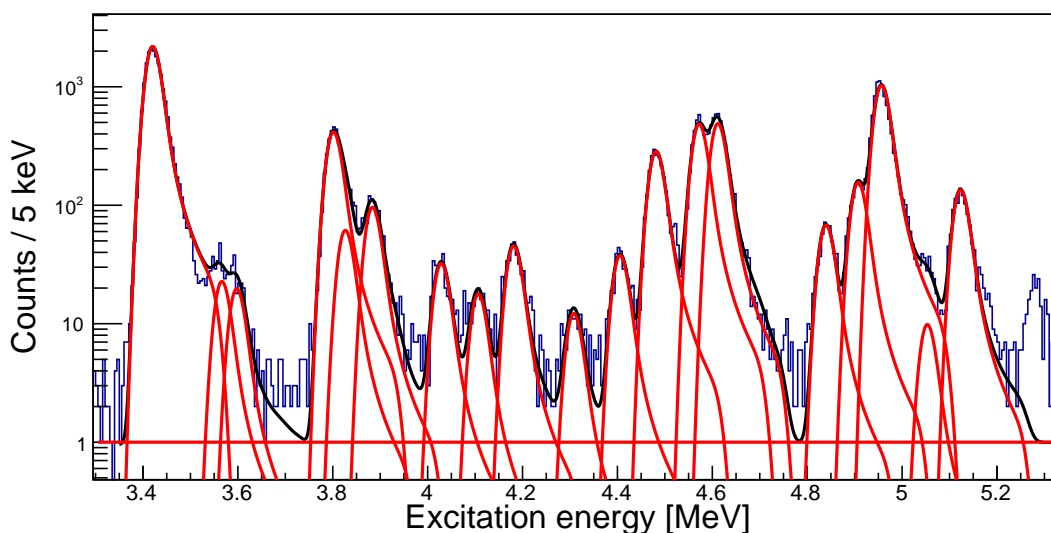


Figure 9.6: Excitation energy spectrum (blue histogram) for the angle region $13.65\text{--}16.35^\circ$, showing the total fit (black line) as well as the fit to the individual peaks and background (red line).

Due to lower statistics the peak strengths of some weaker states were extracted by fitting excitation energy spectra representing the full solid angle range per K600 angle setting, therefore, for these states there is only one data point per angle setting, instead of four.

The cross sections were then calculated assuming a target thickness of 1 mg/cm^2 . The error bars arising in the experimental cross sections represent the statistical error and a 10% systematical error (associated with the uncertainty in extracting the normalization factors) added in quadrature. The centroid value of each state was determined by means of peak fitting. There were three angle settings that contained overlapping angles: the 4° angle setting contains the 5.5° angle, while the 7° angle setting also contains the 5.5°

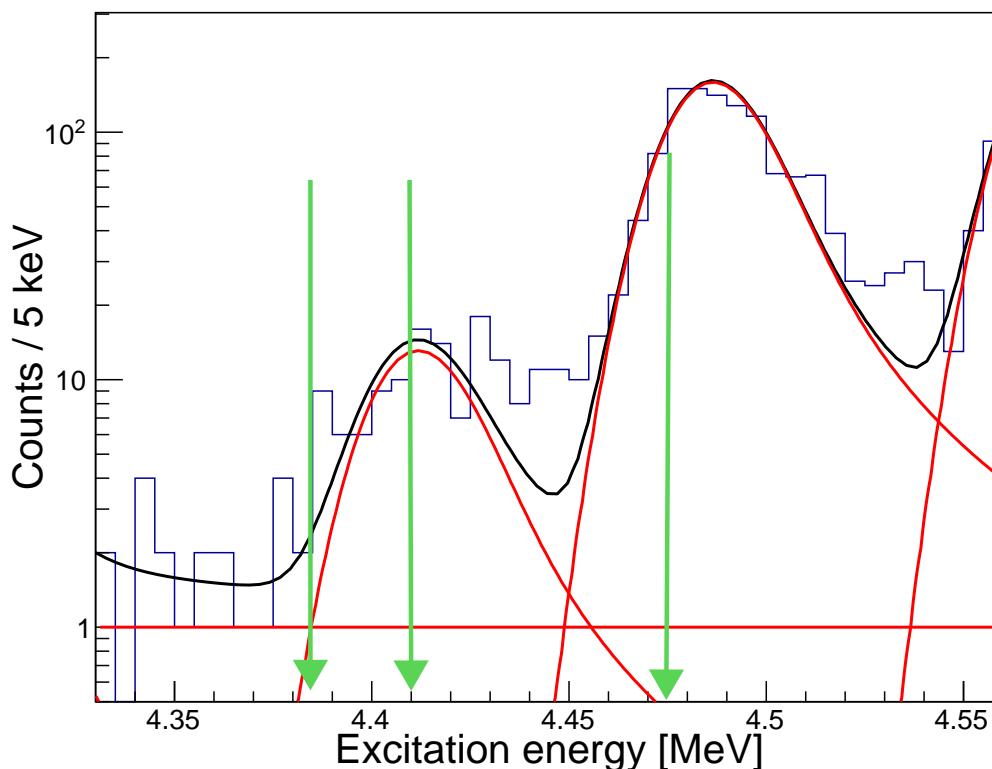


Figure 9.7: Excitation energy fit range for one peak 50 keV below the peak centroid, to 150 keV above the peak centroid. The green arrows represent the lower limit, centroid and upper limit in the range of the fit considered.

angle in its lower part. Similarly the 7° and 10° angle settings have in common the 8.5° angle. This overlap between two angular settings allows a proper relative normalization between them, and gives confidence in the normalization procedure that had to be done due to the target movement complications. It should be noted this was one of the reasons for wanting to divide the data into smaller angle bins, to be sure the different available data sets fit together properly. In plotting the angular distributions, the two data points at the angle overlaps were replaced by a single data point with an averaged value of the cross section.

The 2.348 MeV peak is polluted by the ^{33}S , $\frac{1}{2}^+$ state at $E_x=840$ keV. This is more evident at forward angles i.e 4° , 7° , and 10° and this is because the 840 keV state corresponds to an $\ell=0$ transfer. The contribution of this contaminant was subtracted. The effect of the ^{33}S ground state on the 1.572 MeV state of ^{35}S is negligible, also due to the strength of the 1.572 MeV peak. In the table we show a comparison of the excitation energy values between those obtained in this work and those listed in Ref. [41]. The excitation values listed in this work are accurate to within ± 10 keV of the values listed by Ref. [41]. There are newly identified states at $E_x = 5.620, 8.465, 8.509, 8.557, 8.602, 8.651, 8.707, 8.764, 8.877, 8.946$ and 9.061 MeV. The identified states mainly arise from occupations in the $d_{5/2}$, $d_{3/2}$, $s_{1/2}$, $p_{3/2}$ and $f_{7/2}$ orbits in ^{35}S .

9.3 j^π assignments

In order to make spin and parity assignments the experimental angular distributions have to be compared to the angular distributions from theoretical calculations. The result of these assignments are summarized in the Table 9.2. It should be noted that there were states observed up to 11 MeV not included in the Table 9.2. This is because there a need to investigate missing $d_{5/2}$ strength, which had a lower than expected C^2S value. The angular distributions obtained in this experiment are plotted along with the theoretical calculations and used to identify the ℓ values.

In the following sections a method is proposed to discriminate the j values corresponding to different ℓ values, e.g. $j = \frac{3}{2}$ or $\frac{5}{2}$ for $\ell=2$. The ℓ assignments were made by using the theoretical angular distributions that reproduce best the shape of the experimental data. Fortunately, the first few excited states shown in Figure 9.8, have well defined spin and parities, and the comparisons for these states between theory and experiment were instrumental in final assignments.

From these states with known spin and parity it was noticed that there is a j dependence of the angular distributions that is prominent for the $\ell = 2$ transfers at forward angles. Matoba *et al.*, [1] used spin observable analyzing power to provide a clear signature for the j dependence. As the present experiment was performed with unpolarized beams, such a capability was not available, and in this work we had to rely in subtle differences in the angular distributions, as shown in Figure 9.9. The differences observed in this study has been pointed out for a few decades already see Refs. [84], where it was shown empirically that the j dependence for pickup reactions of an $\ell = 2$ neutron appears mostly at the forward angles. This was shown, among others, for $^{32}\text{S}(p,d)$ reaction at 33.6 MeV.

As alluded to in previous sections the goal is to be able to compare the $\frac{1}{2}$, $\frac{3}{2}$ and $\frac{5}{2}$ states and the shift of their centroids between ^{35}S and ^{39}Ca . Therefore, the theoretical angular distributions had to be computed in a manner similar to the previous study by Matoba *et al.*, [1]. In addition the DWBA analysis of the two nuclei was made similar to make a fair comparison.

Table 9.2: Identification of states

This work		Literature [41]	
Energy [MeV]	j^π	Energy [MeV]	j^π
0.000	$\frac{3}{2}^+$	0.000	$\frac{3}{2}^+$
1.572	$\frac{1}{2}^+$	1.572	$\frac{1}{2}^+$
1.991	$\frac{7}{2}^-$	1.991	$\frac{7}{2}^-$
2.348	$\frac{3}{2}^-$	2.348	$\frac{3}{2}^-$
2.717	$\frac{5}{2}^+$	2.717	$\frac{5}{2}^+$
2.939	$\frac{3}{2}^+$	2.939	$\frac{3}{2}^+$
3.423(1)	$\frac{5}{2}^+$	3.421	$\frac{5}{2}^+$
3.561(3)	$(\frac{3}{2}^+, \frac{5}{2}^+)$	3.558	$(\frac{3}{2}^-, \frac{5}{2}^+)$
3.596(4)	$\frac{7}{2}^-$	3.595	$(\frac{1}{2}^-, \frac{7}{2}^+)$
3.803(1)	$\frac{3}{2}^-$	3.802	$\frac{3}{2}^-$
3.886(3)	$\frac{7}{2}^-$	3.885	$(\frac{3}{2}^-, \frac{5}{2}^-)$
4.024(5)	$\frac{3}{2}^+$	4.026	$(\frac{1}{2}^-, \frac{5}{2}^+)$

Continue on the next page

Table 9.2: (continued.).

Energy [MeV]	j^π	Energy [MeV]	j^π
4.106(6)	$\frac{3}{2}^+$	4.106	$(\frac{1}{2}, \frac{3}{2}, \frac{5}{2})^+$
4.183(3)	$\frac{3}{2}^-$	4.180	$(\frac{1}{2}, \frac{3}{2}, \frac{5}{2}^+)$
4.303(5)	$(\frac{1}{2}^-, \frac{3}{2}^-)$	4.303	$(\frac{1}{2} : \frac{5}{2}, \frac{7}{2}^-)$
4.483(1)	$\frac{7}{2}^-$	4.478	$(\frac{1}{2}, \frac{3}{2}, \frac{5}{2}^+)$
4.573(1)	$\frac{3}{2}^+$	4.576	$(\frac{1}{2} : \frac{5}{2}^+)$
4.614(2)	$\frac{5}{2}^+$	4.617	
4.833(4)	$\frac{1}{2}^+$	4.839	$(\frac{1}{2} : \frac{9}{2}^+)$
4.903(3)	$\frac{1}{2}^-$	4.903	$\frac{1}{2}^-$
4.955(1)	$\frac{5}{2}^+$	4.963	$\frac{3}{2}^-$
5.126(3)	$\frac{1}{2}^+$	5.127	$(\frac{1}{2} : \frac{9}{2}^+)$
5.284(3)	$(\frac{3}{2}^-, \frac{7}{2}^-)$	-	-
5.479(2)	$\frac{3}{2}^+$	5.475	
5.630(2)	$\frac{5}{2}^+$		
5.772(2)	$\frac{5}{2}^+$	5.771	$(\frac{1}{2} : \frac{9}{2}^+)$
5.844(4)	$\frac{5}{2}^+$	5.841	$(\frac{1}{2} : \frac{7}{2}^-)$
6.128(4)	$\frac{3}{2}^+$	6.129	$(\frac{1}{2}, \frac{3}{2}, \frac{5}{2}^+)$
6.222(4)	$\frac{7}{2}^-$		
6.334(3)	$\frac{1}{2}^+$	6.334	
6.437(3)	$\frac{1}{2}^+$	6.446	
6.552(4)	$\frac{3}{2}^+$	6.545	
6.635(4)	$\frac{5}{2}^+$	6.635	
6.684(4)	$\frac{1}{2}^+$	6.684	$(\frac{1}{2} : \frac{9}{2}^+)$
6.790(6)	$\frac{5}{2}^+$		
7.022(6)	$\frac{3}{2}^-$	7.019	
7.101(6)	$\frac{3}{2}^-$	7.101	$\frac{3}{2}$
7.149(6)	$\frac{1}{2}^-$	7.143	
7.215(5)	$\frac{7}{2}^-$	7.218	
7.250(5)	$(\frac{3}{2}^+)$	7.253	
7.276(4)	$\frac{3}{2}^+$	7.276	$\frac{1}{2}^+$
7.331(3)	$\frac{1}{2}^+$	7.331	$\frac{1}{2}^+$
7.344(0)	$\frac{1}{2}^+$	7.344	
7.442(4)	$\frac{3}{2}^-$	7.442	$\frac{1}{2}^+$
7.489(2)	$(\frac{1}{2}^-, \frac{3}{2}^-, \frac{7}{2}^-)$	7.481	$\frac{1}{2}^-$
7.749(3)	$\frac{1}{2}^-$	7.750	
7.887(3)	$\frac{5}{2}^+$	7.889	
7.977(7)	$\frac{5}{2}^+$	7.974	$\frac{3}{2}^-$

Continue on the next page

Table 9.2: (continued.).

Energy [MeV]	j^π	Energy [MeV]	j^π
8.078(3)	$\frac{5}{2}^+$	8.078	
8.103(0)	$\frac{5}{2}^+$	8.093	$\frac{1}{2}^-$
8.220(0)	$\frac{1}{2}^-$	8.224	$\frac{1}{2}^-$
8.265(3)	$(\frac{3}{2}^+, \frac{1}{2}^-)$	8.273	$\frac{1}{2}$
8.409(7)	$(\frac{3}{2}^+, \frac{5}{2}^+)$	8.419	$(\frac{1}{2} : \frac{9}{2}^+)$
8.465(8)	$\frac{5}{2}^+$		
8.509(3)	$\frac{5}{2}^+$		
8.557(8)	$\frac{7}{2}^-$		
8.602(4)	$\frac{7}{2}^-$		
8.651(8)	$\frac{7}{2}^-$		
8.707(3)	$(\frac{3}{2}^+, \frac{5}{2}^+)$	-	-
8.764(8)	$\frac{5}{2}^+$		
8.820(5)	$\frac{1}{2}^-$		
8.877(6)	$\frac{1}{2}^-$		
8.946(6)	$\frac{1}{2}^-$		
9.020(28)	$\frac{3}{2}^-$		
9.060(14)	$\frac{3}{2}^-$		
9.124(7)	$\frac{1}{2}^+$		
9.182(4)	$\frac{1}{2}^+$	9.155	$(\frac{1}{2} : \frac{9}{2}^+)$
9.226(11)	$\frac{1}{2}^+$		
9.291(8)	$\frac{3}{2}^-$		
9.344(7)	$\frac{1}{2}^+$		
9.395(5)	$\frac{3}{2}^-$		
9.445(7)	$\frac{3}{2}^-$		

The theoretical calculations apply the same potential parametrization as in Ref. [1] using the FRESCO code [85] (ADWA type calculation). For protons, the global optical potential parameters of Menet *et al.*, [86] and for deuterons, an adiabatic model deuteron potential was used in the exit channel, which takes into account the deuteron breakup effects in an approximate way [87]. These were constructed with the proton and neutron optical potential parameters of Becchetti and Greenlees [88]. Table 9.3, summarizes the parameters used by Matoba *et al.*, [1] and the current study.

Table 9.3: Details of the theoretical calculations.

Matoba <i>et al.</i> , [1]	Current work
DWBA zero range, local energy approximation + finite range parameter 0.629 Non locality for neutron protons , deuteron potentials(b=0.85,0.85,0.54)	DWBA finite range
p+ ⁴⁰ Ca, global optical potential parameters of Menet et al. [86]	p+ ⁴⁰ Ca, global optical potential parameters Menet et al.[86]
d+ ³⁹ Ca: adiabatic based on Becchetti and Greenlees [88] n and p potentials	d+ ³⁹ Ca: adiabatic based on Becchetti and Greenlees [88] n and p potentials
Reduction by $\frac{2}{3}$ of the V_{so} depth for better reproduction of analyzing powers ($6.2 * \frac{2}{3} = 4$ MeV)	$\frac{V_{so}}{2} = \frac{6.2}{2} = 3.1$ MeV
Bound state wave function for neutrons in ⁴⁰ Ca	Bound state wave function for neutrons in ⁴⁰ Ca
Effective Binding energy method Wood Saxon parameters $r_0=1.27$ fm, $a_0=0.70$ fm adjusted with 25 times the spin-orbit Thomas term to get sum rule of 6 nucleons in $f_{7/2}, s_{1/2}, d_{3/2}$	Separation energy method Wood Saxon parameters $r_0=1.27$ fm, $a_0=0.70$ fm and $V_{so} = 6.2$ MeV

The expected shapes for the different transferred angular momentum for states in ³⁵S and ³⁹Ca are shown in Figure 9.10. The experimental angular distributions for some states are plotted together with the theoretical calculations in Figures 9.14 to 9.16. Depending on how well the DWBA calculations reproduce experimental data, ℓ transfer values can be assigned to the different states. In making the ℓ assignments, we are guided by the

comparisons between the experimental angular distributions and theoretical calculations. Spectroscopic factors were determined by scaling the theoretical calculations to experimental data. The normalizing factors (scaling factors) were determined by means of a least square fit. There is a relatively good agreement between experimental results and DWBA calculations in particular for states that are well separated and have a high cross section. Angular distributions could be extracted for a total of 49 states listed.

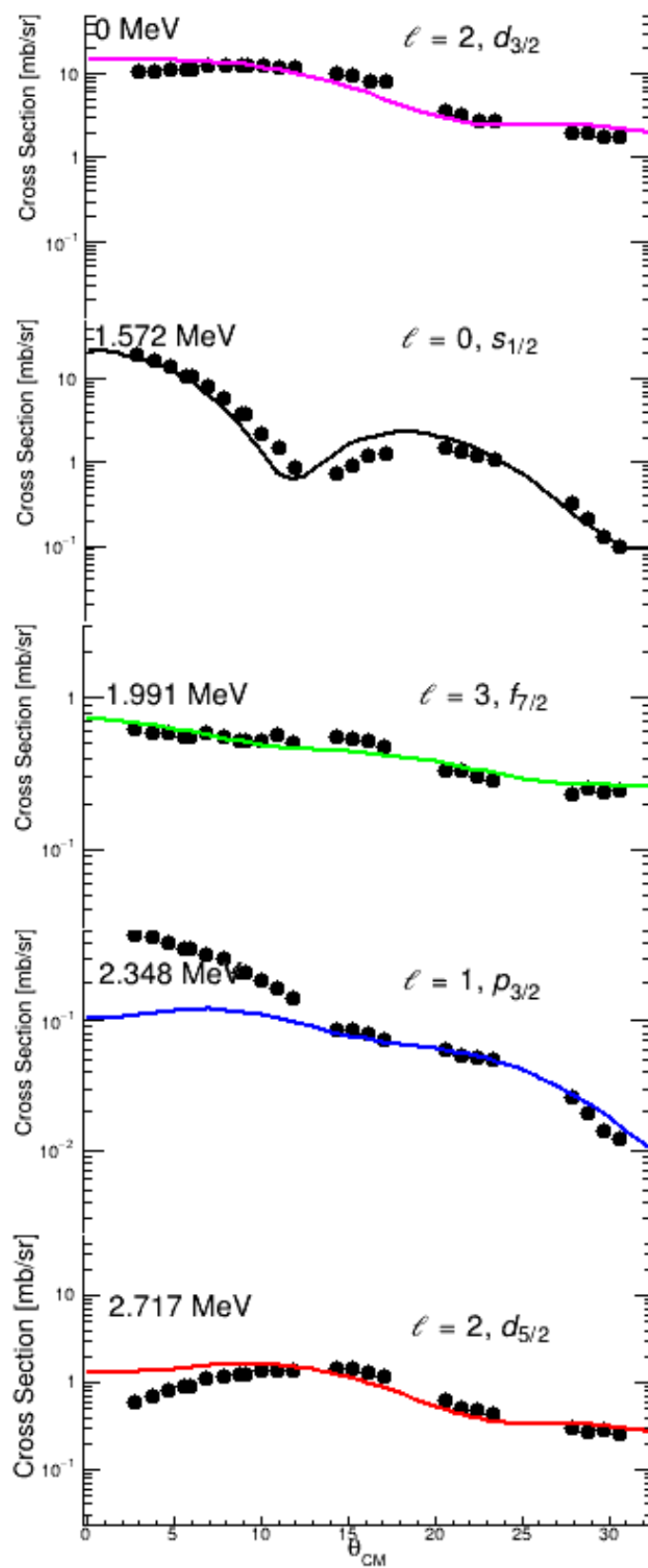


Figure 9.8: Angular distributions for the first five excited states with well known ℓ and j assignments. The (small) error bars, often smaller than the size of the data points, of the experimental cross sections reflect both systematic uncertainties (energy, normalization) and statistical errors.

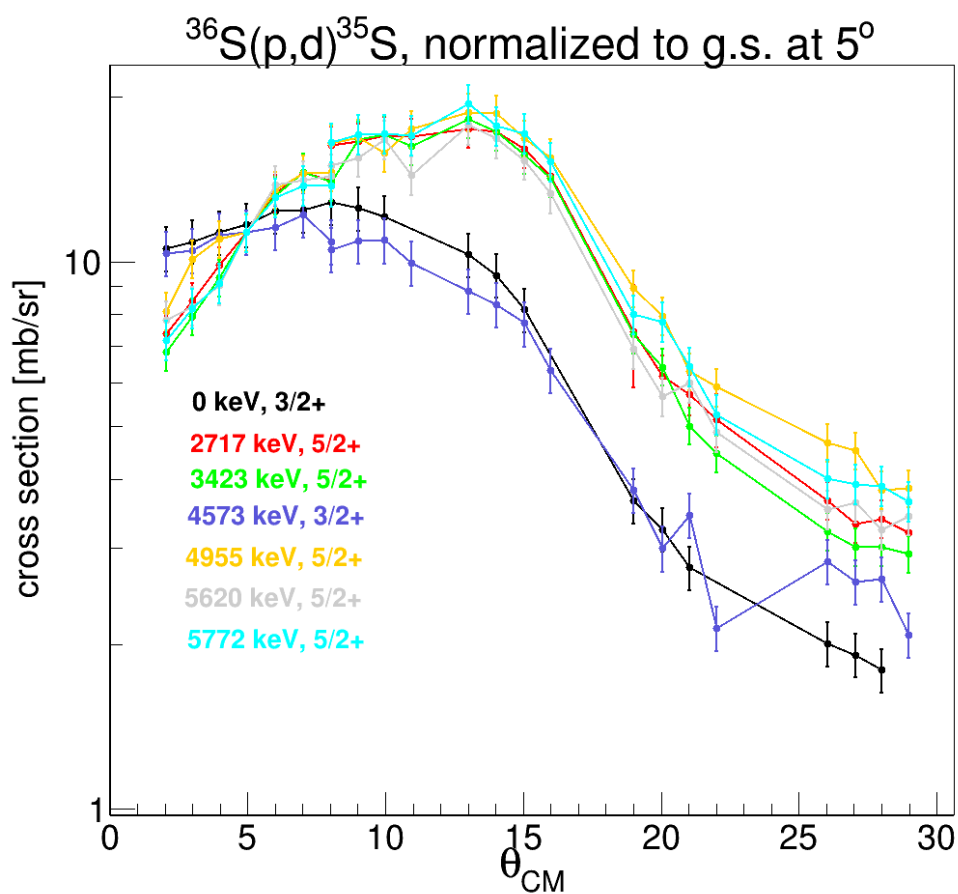


Figure 9.9: Comparison between some $d_{5/2}$ and $d_{3/2}$ states in ^{35}S , indicating the difference in angular pattern of the angular distributions as a result of a j dependence.

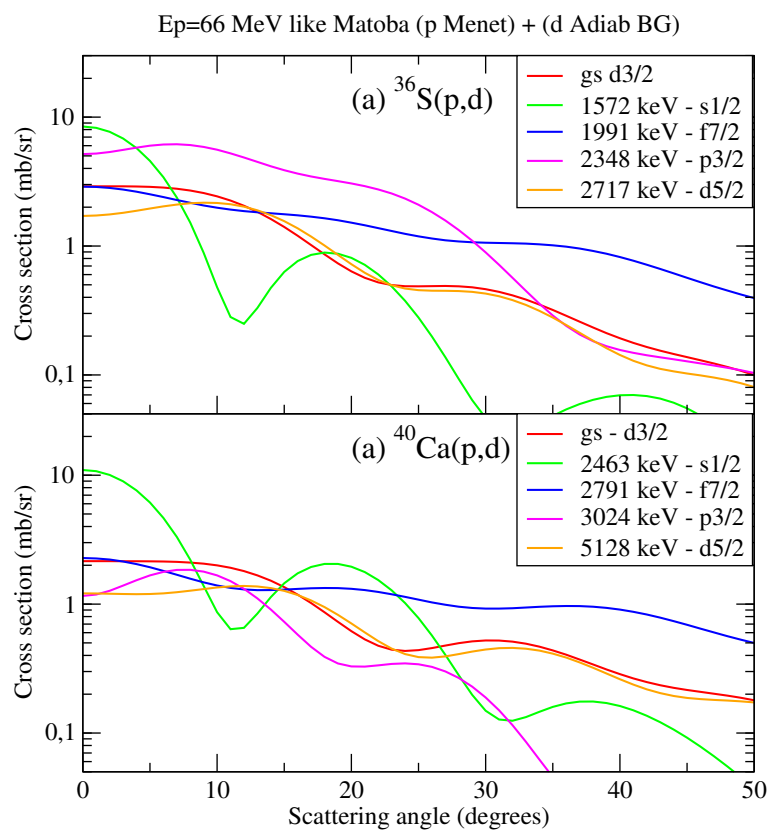


Figure 9.10: A sample selection of typical expected angular distribution shapes for the different ℓ values as calculated for ^{39}Ca and ^{35}S .

- $\ell = 0$ states

From the shape of the angular distribution the state at $E_x = 1.572$ MeV is attributed $\ell = 0$ orbital angular momentum and this is the strongest $\ell = 0$ state. This assignment is also consistent with what is known in literature [41]. These states are distinguished by an angular distribution with a distinct minimum between 10° and 15° and the cross section peaks at $\theta_{lab} = 4^\circ$ as shown in Figure 9.11. The following other states have clearly been assigned $\ell = 0$ orbital momentum transfer: 4.833, 5.126, 6.334, 6.437, 6.684, 7.331, 7.344, 9.124, 9.182, 9.226 and 9.334 MeV.

- $\ell = 1$ states

The fits to the $\ell = 1$ transferred angular momentum are poor and the shape of the experimental angular distributions are not well reproduced by the theoretical calculations. Such an effect was also observed in the study by Matoba *et al.*, [1] for ^{39}Ca . However, the $\ell = 1, \frac{1}{2}^-$ states are better fitted than the $\frac{3}{2}^-$ states. This could possibly be due to the nature of the states (hole and particle, respectively), or to the number of particle hole states. In literature there are 19 states that are firmly assigned $\ell = 1, \frac{3}{2}^-$ or $\ell = 1, \frac{1}{2}^-$ in ^{35}S . We observed three states in common with what is found in literature for the $\ell = 1, \frac{3}{2}^-$ assignment (see Table 9.2). In this work, a total of 11 states have been identified as having $\ell = 1, \frac{3}{2}^-$ assignment with the first being at 2.348 MeV. The remaining states identified as $\ell = 1$ states are at 3.803, 4.183, 7.022, 7.101, 7.442, 9.020, 9.060, 9.261, 9.395 and 9.445 MeV. Some states were firmly assigned $\ell = 1, \frac{1}{2}^-$ and these are at 4.903, 7.149, 7.749, 8.220, 8.820, 8.877 and 8.946 MeV

In principle the $\frac{3}{2}^-$ states should not be observed from this reaction, unless the $p_{3/2}$ orbital is significantly populated by $2p2h$ configurations in the ^{36}S ground state. Conversely, $\frac{3}{2}^-$ states are well populated in $^{34}\text{S}(d,p)^{35}\text{S}$ reaction, from which most of the $\frac{3}{2}^-$ states were identified. There should exist $\frac{1}{2}^-$ states from the $2p_{1/2}$ orbital that should be even less populated than the $2p_{3/2}$ states as the $2p_{1/2}$ lies at higher

excitation energy, but also $\frac{1}{2}^-$ hole states arising from the $1p_{1/2}$ orbital that are favorably populated in the (p,d) reaction. These are probably these states that are observed in the present experiment.

- $\ell = 2$ states

As for the j assignment there are 2 possibilities: $\ell = 2$ ($d_{3/2}$), and $\ell = 2$ ($d_{5/2}$). A total of 9 states have been identified having $\ell = 2$ ($d_{3/2}$) and these are the states at $E_x = 0, 2.939, 4.025, 4.106, 4.573, 5.479, 6.128, 6.552$ and 7.276 MeV. The states firmly assigned to $\ell = 2$ ($d_{5/2}$) are: $2.717, 3.423, 4.614, 4.955, 5.630, 5.772, 5.844, 6.635, 6.790, 7.887, 7.997, 8.078, 8.103, 8.465, 8.509$ and 8.764 MeV. There is a huge discrepancy in the j^π assignment of the 5.844 MeV state in literature where it was assigned negative parity. In the current this state is clearly not a candidate for any of the negative parity orbital if considering the angular pattern. The states we tentatively assign as $\ell = 2$, ($d_{5/2}$) or ($d_{3/2}$) are at $E_x = 3.561, 8.409$ and 8.707 MeV. Many $5/2^+$ states were anticipated at high excitation energy from the fragmentation of the $d_{5/2}$ hole state. Less fragmentation is expected and found for the $3/2^+$ states.

- $\ell = 3$ states

A total of 9 states are consistent with an $\ell = 3$ assignment and these are at $E_x = 1.991, 3.886, 4.483, 6.222, 7.215, 8.557, 8.602$ and 8.651 MeV. We are in agreement with the assignment found in literature for the 1.991 state only.

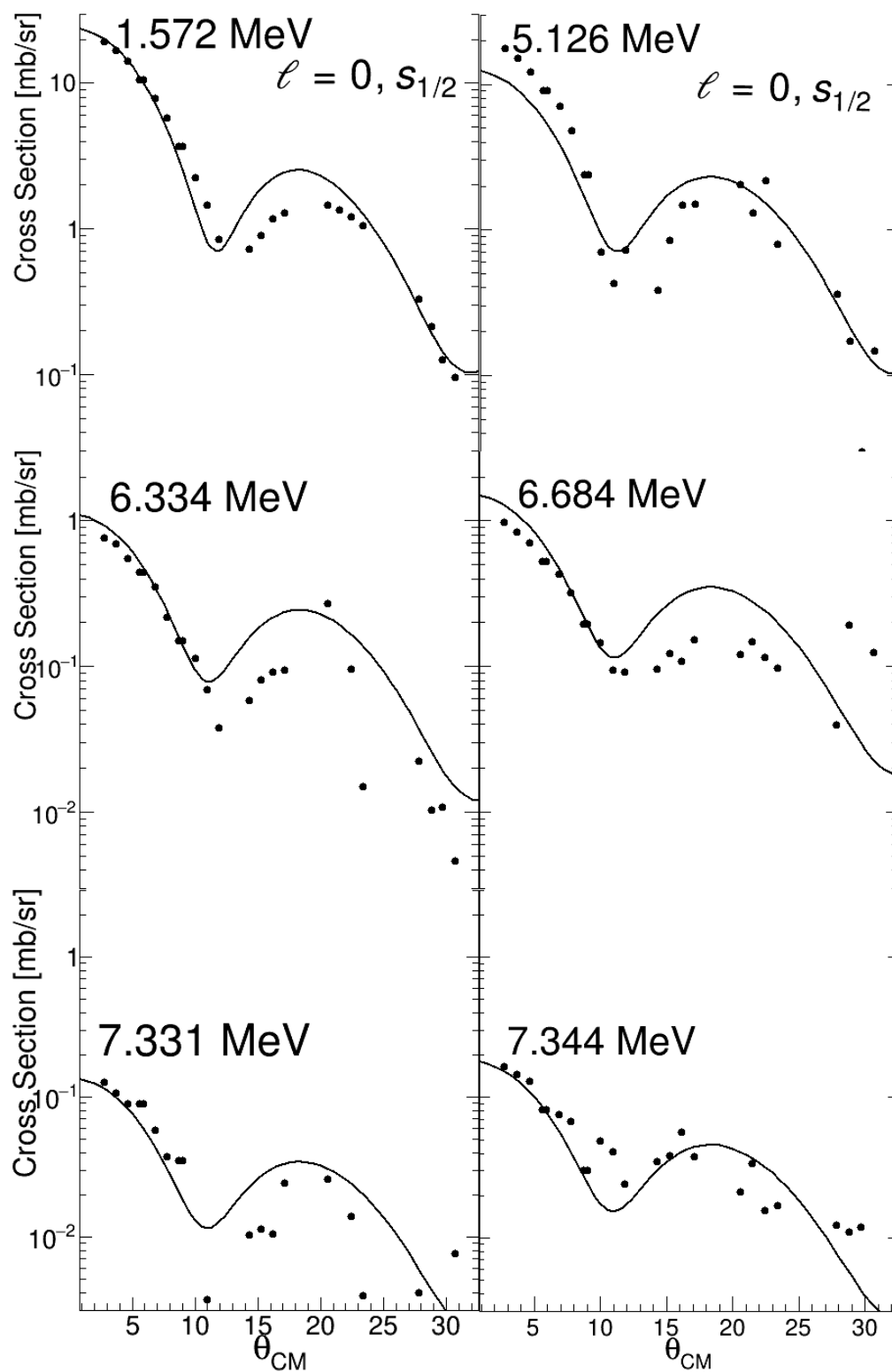


Figure 9.11: Angular distributions for $\ell=0$ ($s_{1/2}$) transferred angular momentum.

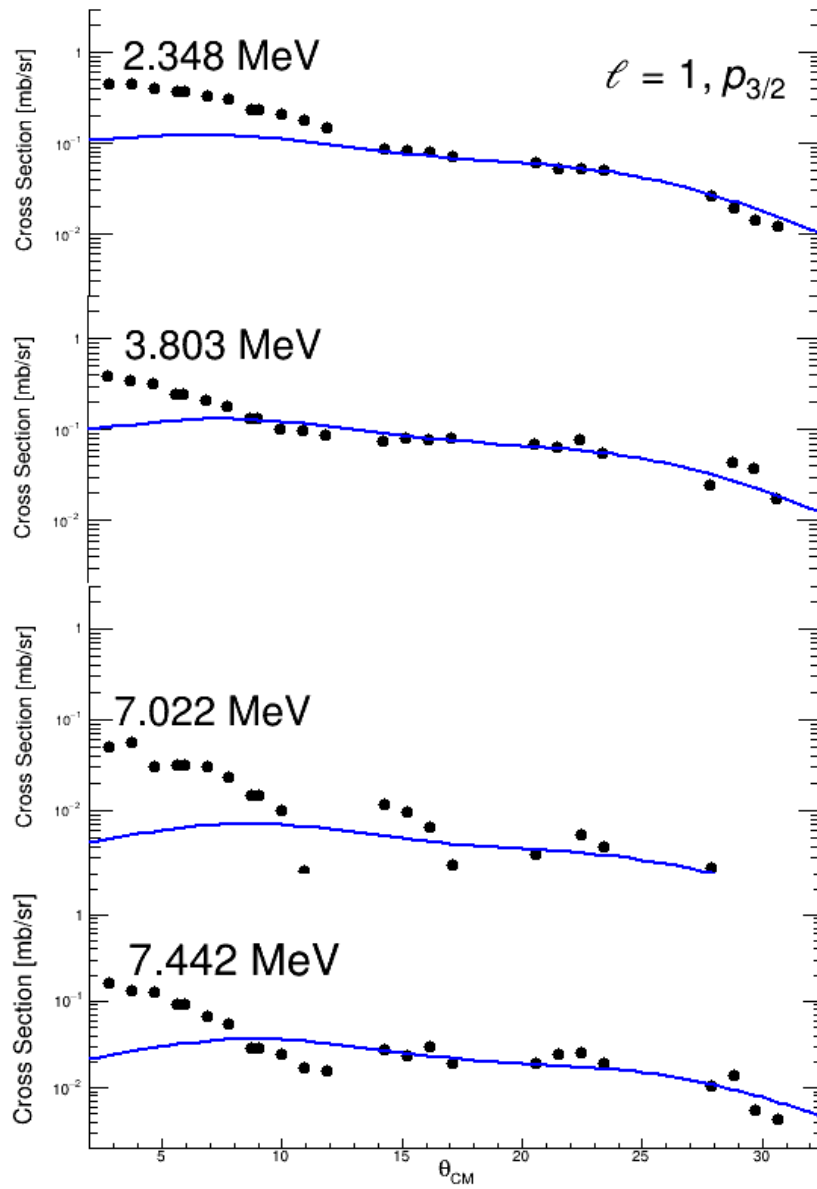


Figure 9.12: Angular distributions for $\ell=1$ ($p_{3/2}$) transferred angular momentum.

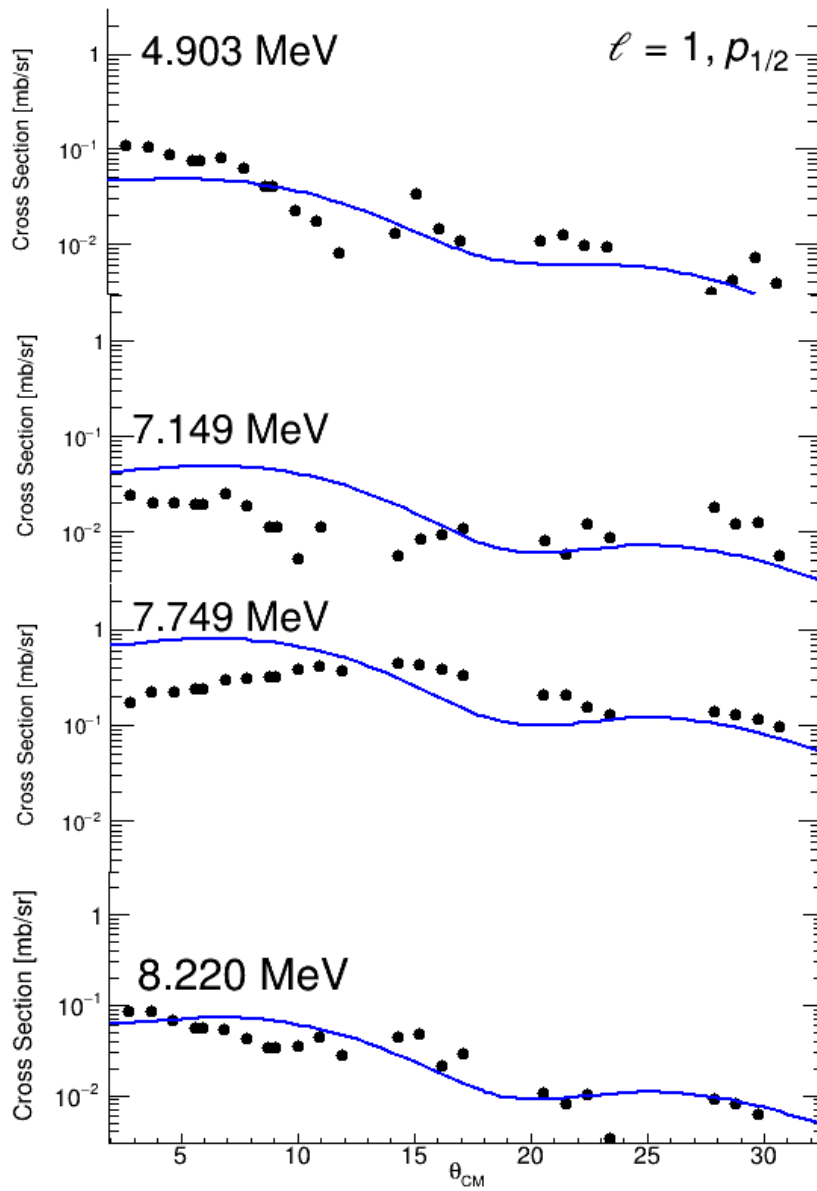


Figure 9.13: Angular distributions for $\ell = 1$ ($p_{1/2}$) transferred angular momentum.

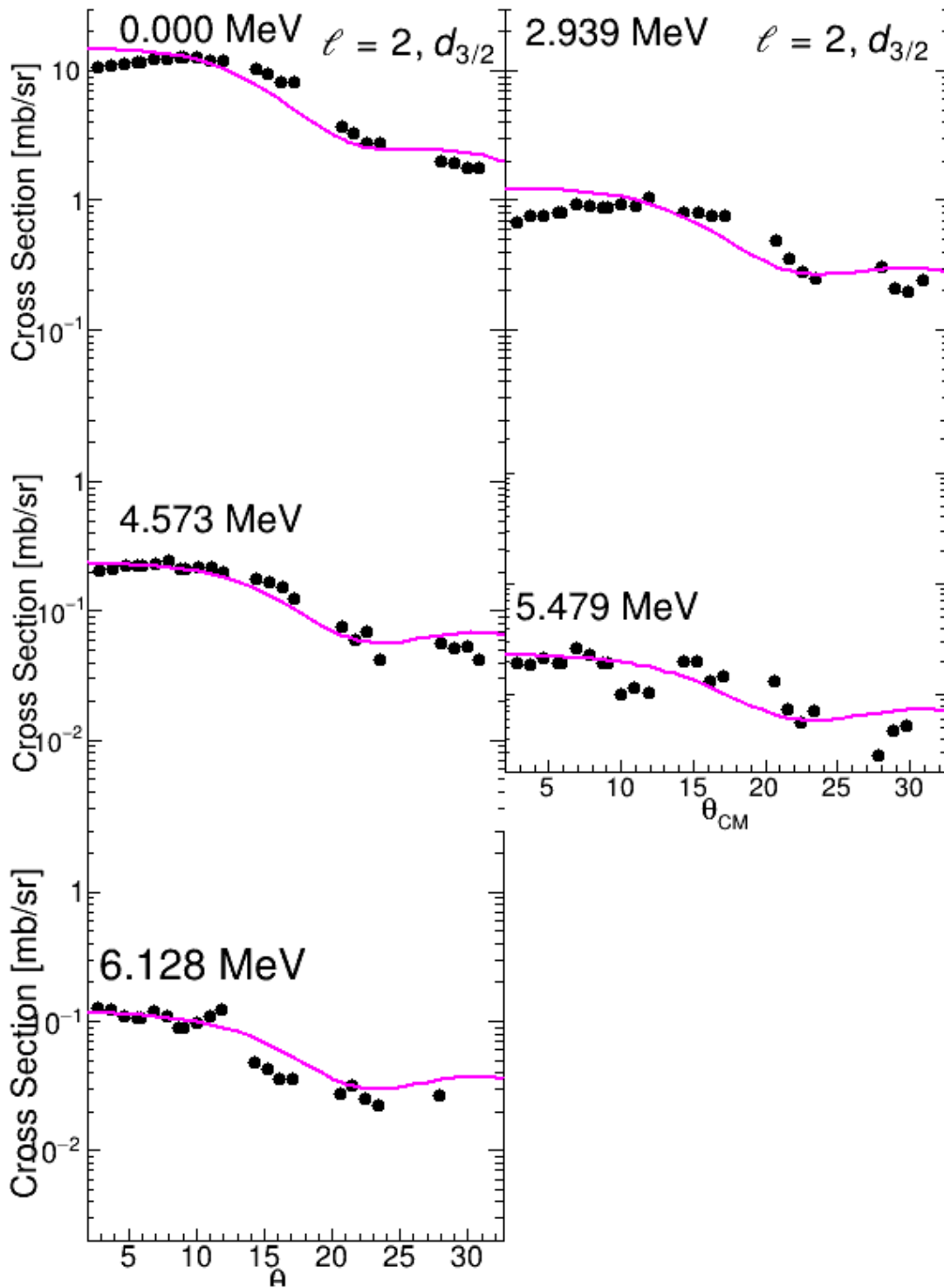


Figure 9.14: Angular distributions for $\ell = 2$ ($d_{3/2}$) transferred angular momentum.

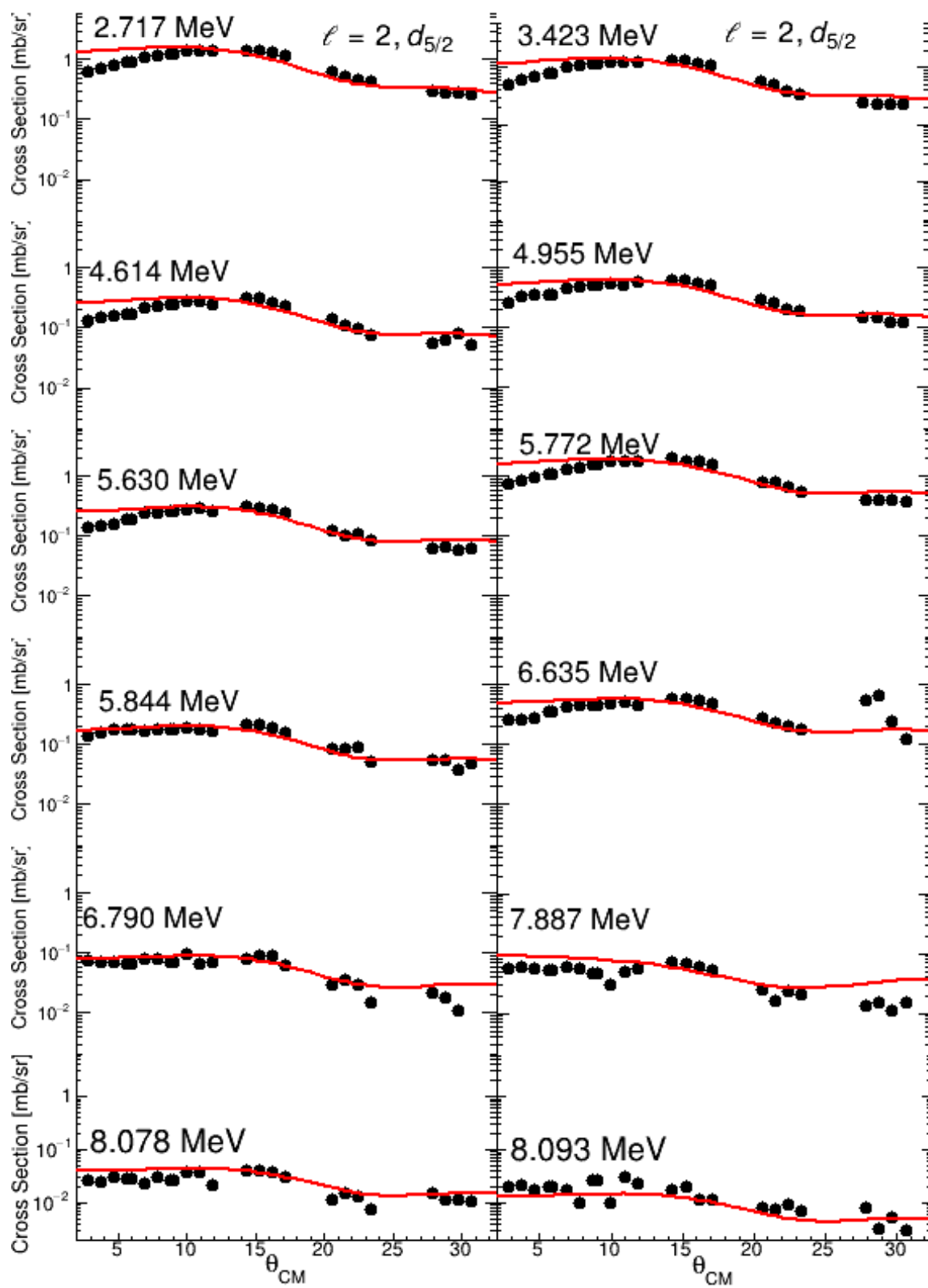


Figure 9.15: Angular distributions for $\ell=2$ ($d_{5/2}$) transferred angular momentum.

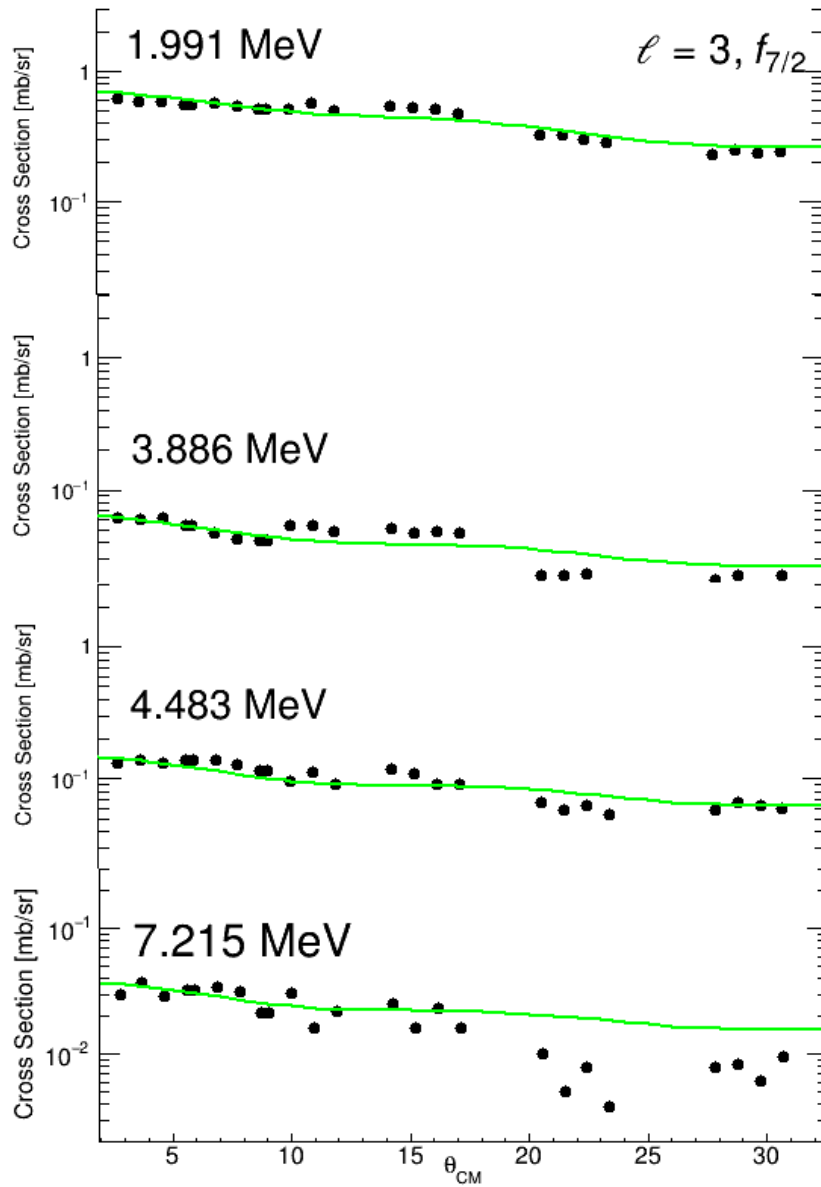


Figure 9.16: Angular distributions for $\ell = 3$ ($f_{7/2}$) transferred angular momentum.

9.4 $^{40}\text{Ca}(\text{p,d})^{39}\text{Ca}$ Analysis

We recall the work of Matoba *et al.*, [1] because we wish to compare the two nuclei using similar optical model potential analysis, thus having a consistent determination of the C^2S values. The previous study of the $^{40}\text{Ca}(\text{p,d})^{39}\text{Ca}$ reaction was performed using a polarized proton beam at an incident energy of 65 MeV. A new set of theoretical angular distributions was calculated. The resulting angular distributions from these theoretical calculations is shown in Figures 9.17 and 9.18. Similarly in ^{39}Ca , we notice, much like ^{35}S , that the $\frac{3}{2}^+$ and $\frac{5}{2}^+$ angular distributions differ, as shown in Figure 9.19. The $d_{5/2}$ strength is also fragmented just like in the case of ^{35}S . However the $d_{3/2}$ strength is not fragmented and there are more $j^\pi = \frac{3}{2}^+$ states in ^{35}S , as compared to ^{39}Ca . If we compare the summed C^2S values from Matoba *et al.*, with the current work for ^{39}Ca , we obtain an average standard deviation of 0.05 which is consistent with a systematic difference of 8% in the values. Therefore, we can say there is a relatively good agreement in the C^2S values, also indicated in Table 9.4.

Table 9.4: Comparison in C^2S values between previous study by Ref. [1] and the values obtained using the new set of theoretical angular distributions.

	$\frac{3}{2}^+$	$\frac{1}{2}^+$	$\frac{5}{2}^+$	$\frac{7}{2}^-$	$\frac{3}{2}^-$
Matoba <i>et al.</i> , [1]	3.74	1.79	4.67	0.26	0.02
Current work	3.78	1.82	4.84	0.39	0.02

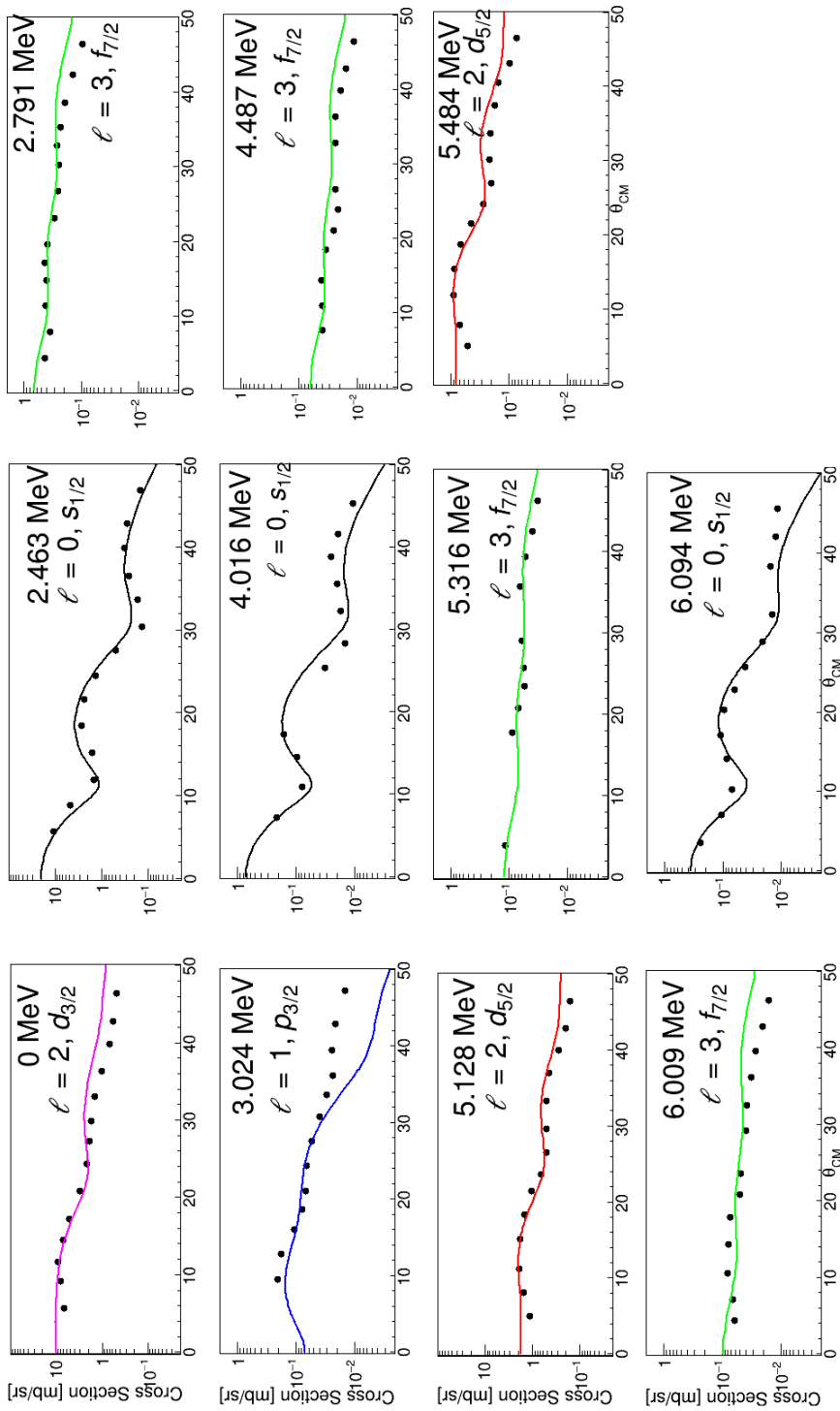


Figure 9.17: Experimental angular distributions superimposed with DWBA calculations from this work for different states in ^{39}Ca in the range $E_x=0-6$ MeV. Experimental data was obtained from Ref. [1].

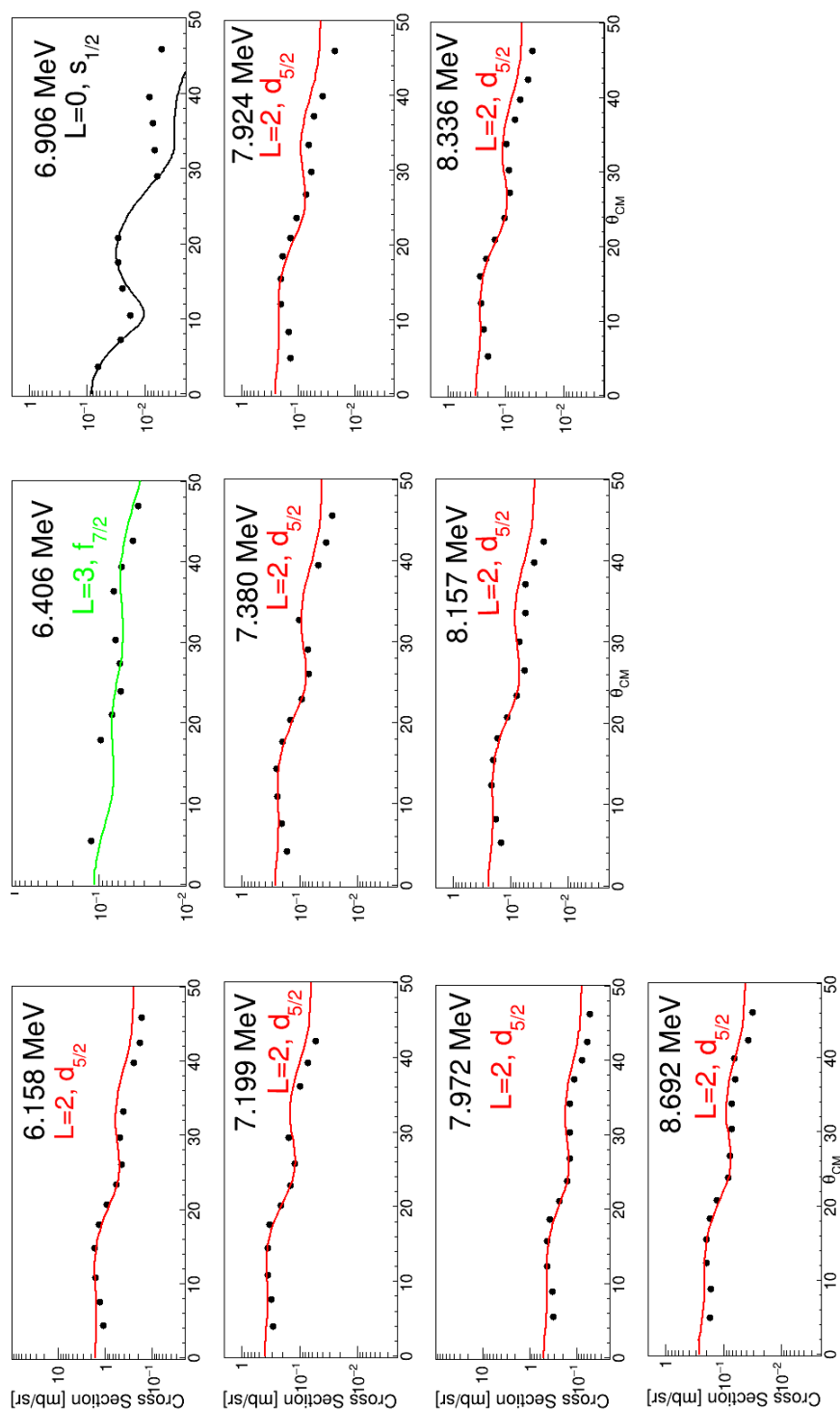


Figure 9.18: Experimental angular distributions superimposed with DWBA calculations from this work for different states in ^{39}Ca in the range $E_x = 6-8.7$ MeV. Experimental data was obtained from Ref. [1].

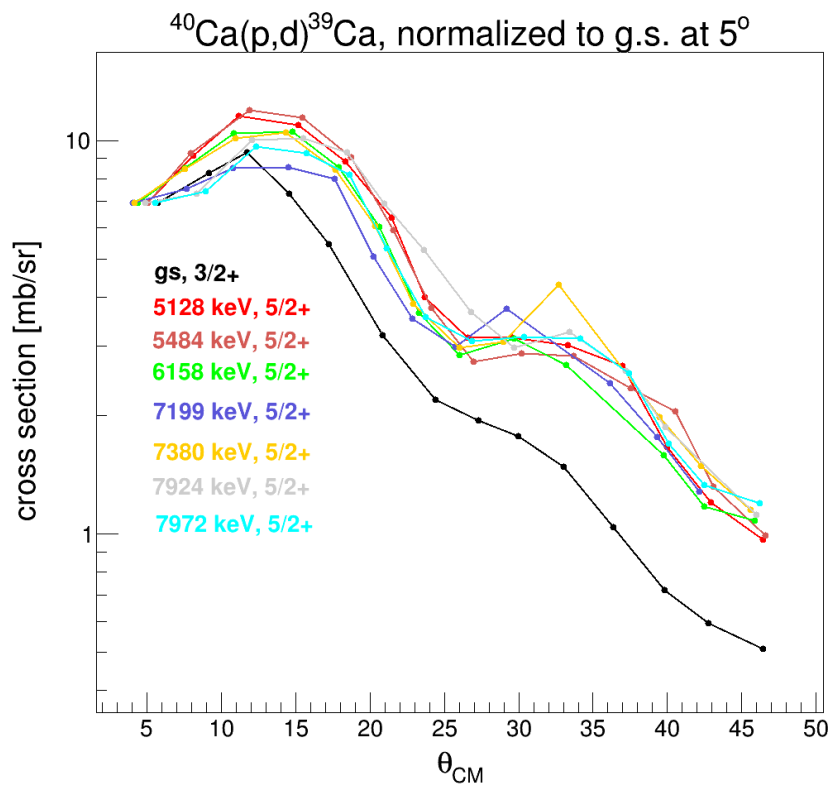


Figure 9.19: Comparison between some $d_{5/2}$ and $d_{3/2}$ states in ^{39}Ca , indicating the difference in angular character of the angular distributions as a result of a j dependence.

10 | Discussion

In this chapter I provide a global discussion of the thesis considering the results from the knockout and transfer reactions. It is intended here to investigate the evolution of the $1d_{3/2}$, $2s_{1/2}$ and $1d_{5/2}$ neutron hole states between ^{36}S and ^{40}Ca , with a special emphasis on the evolution of the $1d$ spin-orbit splitting as 4 neutrons are added to the $1d_{3/2}$ orbital. A comparison between the two different experimental approaches is discussed.

10.1 Single hole states in ^{39}Ca

The resulting summed C^2S values, C^2S weighted mean energies and centroid $\langle \epsilon_j \rangle$ energy values are listed in Table 10.1. There are several $\ell = 0, \frac{1}{2}^+$ states in ^{39}Ca [1]. These are at $E_x = 2.463$ MeV ($C^2S=1.697$), 4.016 MeV ($C^2S=0.0591$), 6.094 MeV ($C^2S=0.0337$) and 6.906 MeV ($C^2S=0.008$). Most of the $s_{1/2}$ strength is from the first $\frac{1}{2}^+$ excited state at 2.463 MeV. The resulting C^2S -weighted mean energy value of the $\frac{1}{2}^+$ states is $\frac{1}{2}^+ = 2.48$ MeV. The summed spectroscopic strength is $\sum C^2S (\frac{1}{2}^+) = 1.798$, which is within reasonable agreement with the expected full occupancy. There is also a small fraction of $\frac{1}{2}^+$ states found in the neutron-adding $^{40}\text{Ca}(d,p)^{41}\text{Ca}$ [89] reaction with $C^2S=0.03$ at 2.670 MeV, 0.03 at 3.399 MeV and 0.01 at 3.845 MeV, with a summed C^2S of 0.08. Altogether, this corresponds to a C^2S value of 0.5 for the vacancy of the $s_{1/2}$

and $d_{3/2}$ orbitals found from the neutron-adding experiment. This is to be compared to the ^{39}Ca value obtained in this study of $0.022+0.386=0.408$, that correspond to the scattering, to in principle, not occupied fp state. The agreement between the two values, given that the optical model potential used are not the same for neutron-adding and neutron-removal reactions, is very good.

Table 10.1: Summed C^2S , C^2S weighted mean energy and the binding energy $\langle \epsilon_j \rangle$ values in ^{39}Ca .

Orbit	$\sum C^2S$	\bar{E} [MeV]	$\langle \epsilon_j \rangle$ [MeV]
$s_{1/2}$	1.798(90)	2.478	-18.108
$d_{3/2}$	3.776(19)	0	-15.635
$d_{5/2}$	4.844(24)	6.202	-21.837
$p_{3/2}$	0.022(1)	3.500	-11.311
$f_{7/2}$	0.386(19)	3.689	-11.748

For ^{39}Ca some of the $d_{3/2}$ strength is found in the stripping reaction $^{40}\text{Ca}(d,p)^{41}\text{Ca}$ [89], at $E_x = 2.009$ MeV, 4.418 MeV, 5.095 MeV and 5.411 MeV leading to a summed C^2S^+ value of 0.42. Despite the small value of 0.42 this is indicative of a vacancy for neutrons in the $d_{3/2}$ orbital in ^{40}Ca . This would mean that some particles are scattered into the upper shells being the $p_{3/2}$ and $f_{7/2}$, in agreement with the fact that these neutrons could be removed through the (p,d) reaction, as observed in our experiment. If we include all $\frac{3}{2}^+$ C^2S values from the (d,p) reaction, this shifts the centroid of $\frac{3}{2}^+$ centroid energy to positive values. Therefore, instead of $\bar{E}=0$ for the C^2S , we obtain 1.345 MeV.

10.2 Single hole states in ^{35}S populated from the $^{36}\text{S}(p, d)$ reaction

For consistency with the analysis from Ref. [1] the $\sum C^2S(d_{3/2}) + \sum C^2S(f_{7/2}) + \sum C^2S(s_{1/2}) + \sum C^2S(p_{3/2}) = 6$, normalization was used. The resulting spectroscopic factors for the various states are listed in Table 10.2. The C^2S , weighted mean energy for each orbit was obtained using:

$$\bar{E}(j) = \frac{\sum E_x(j)C^2S(j)}{\sum C^2S}. \quad (10.1)$$

The centroid binding energy of a positive-parity j orbital is then obtained using:

$$\langle \epsilon_j \rangle = -S_n(^{36}\text{S}) - \bar{E}(j), \quad (10.2)$$

while for the negative-parity orbitals it is:

$$\langle \epsilon_j \rangle = -S_n(^{36}\text{S}) + \bar{E}(j), \quad (10.3)$$

where $S_n(^{36}\text{S})$ is the neutron binding energy in ^{36}S and is equal to 9.89 MeV [41]. The resulting summed C^2S values, C^2S weighted mean energies and centroid $\langle \epsilon_j \rangle$ energy values are listed in Table 10.3.

Table 10.2: Spectroscopic factors and comparison between results from the $^{36}\text{S}(-1n)^{35}\text{S}$ and $^{36}\text{S}(p, d)^{35}\text{S}$ reactions. Blank entries indicate the absence of data. The uncertainties in the C^2S values for the (p, d) reaction only include the error in the target thickness and the statistical contribution. The systematic error associated with the choice of optical model is not included.

$^{36}\text{S}(p, d)^{35}\text{S}$				$^{36}\text{S}(-1n)$ Knockout		
Energy [MeV]	j^π	ℓ	C^2S	$C^2S_{(-1n)}$	j^π	ℓ
Energy	j^π	ℓ	C^2S	$C^2S_{(-1n)}$	j^π	ℓ
0.000	$\frac{3}{2}^+$	2	3.32(40)	3.13(7)	$\frac{3}{2}^+$	2
1.572	$\frac{1}{2}^+$	0	1.88(90)	1.19(2)	$\frac{1}{2}^+$	0
1.991	$\frac{7}{2}^-$	3	0.180(19)	0.10	$\frac{7}{2}^-$	3
2.348	$\frac{3}{2}^-$	1	0.036(4)	0.32(1)	$\frac{3}{2}^-$	1
2.717	$\frac{5}{2}^+$	2	0.539(56)	0.53(4)	$\frac{5}{2}^+$	2
2.939	$\frac{3}{2}^+$	2	0.038(3)	0.29(3)	$\frac{3}{2}^+$	2
3.423(1)	$\frac{5}{2}^+$	2	0.503(51)	0.46(5)	$\frac{5}{2}^+$	2
3.561(3)	$\frac{7}{2}^-$	3	0.017(6)			
3.596(4)	$\frac{7}{2}^-$	3	0.0060(6)			
3.803(1)	$\frac{3}{2}^-$	1	0.025(3)			
3.818				0.35(4)	$\frac{7}{2}^-$	3
3.886(3)	$\frac{7}{2}^-$	3	0.018(2)	0.23(3)	$\frac{1}{2}^+$	0
4.024(5)	$\frac{3}{2}^+$	2	0.0060(7)	0.28(5)		2
4.106(6)	$\frac{3}{2}^+$	2	0.0030(4)			
4.183(3)	$\frac{3}{2}^-$	1	0.0010(1)			
4.303(5)	$\frac{1}{2}^-$	1	0.0014(2)			
4.483(1)	$\frac{7}{2}^-$	3	0.047(5)			
4.573(1)	$\frac{3}{2}^+$	2	0.077(8)			
4.614(2)	$\frac{5}{2}^+$	2	0.123(13)			
4.833(4)	$\frac{1}{2}^+$	0	0.013(1)			
4.903(3)	$\frac{1}{2}^-$	1	0.0181(17)			
4.955(1)	$\frac{5}{2}^+$	2	0.253(28)			
5.126(3)	$\frac{1}{2}^+$	0	0.014(1)			
5.284(3)	$\frac{3}{2}^-$	1	0.0020(2)			
5.479(2)	$\frac{3}{2}^+$	2	0.007(1)			
5.630(2)	$\frac{5}{2}^+$	2	0.123(13)			
5.772(2)	$\frac{5}{2}^+$	2	0.817(90)			
5.844(4)	$\frac{5}{2}^+$	2	0.085(9)			
6.128(4)	$\frac{3}{2}^+$	2	0.008(1)			

Continue on the next page

Table 10.2: (continued.).

Energy [MeV]	j^π	ℓ	C^2S	$C^2S_{(-1n)}$	j^π	ℓ
6.222(4)	$\frac{7}{2}^-$	3	0.001(1)			
6.334(3)	$\frac{1}{2}^+$	0	0.061(5)			
6.437(3)	$\frac{1}{2}^+$	0	0.009(1)			
6.552(4)	$\frac{3}{2}^+$	2	0.006(1)			
6.635(4)	$\frac{5}{2}^+$	2	0.259(20)			
6.684(4)	$\frac{1}{2}^+$	0	0.079(8)			
6.790(6)	$\frac{5}{2}^+$	2	0.036(4)			
7.022(6)	$\frac{3}{2}^-$	1	0.0058(9)			
7.101(6)	$\frac{3}{2}^-$	1	0.0123(25)			
7.149(6)	$\frac{1}{2}^-$	1	0.006(1)			
7.215(5)	$\frac{7}{2}^-$	3	0.011(1)			
7.250(5)	$(\frac{3}{2}^+)$	2	0.019(3)			
7.276(4)	$\frac{3}{2}^+$	2	0.011(5)			
7.331(3)	$\frac{1}{2}^+$	0	0.011(5)			
7.344(0)	$\frac{1}{2}^+$	0	0.011(5)			
7.442(4)	$\frac{3}{2}^-$	1	0.027(5)			
7.489(2)	$(\frac{1}{2}^+)$	0	0.014(2)			
7.749(3)	$\frac{1}{2}^-$	1	0.0397(40)			
7.887(3)	$\frac{5}{2}^+$	2	0.201(21)			
7.977(7)	$\frac{5}{2}^+$	2	0.029(3)			
8.078(3)	$\frac{5}{2}^+$	1	0.030(4)			
8.103(0)	$\frac{5}{2}^+$	2	0.006(1)			
8.220(0)	$\frac{1}{2}^-$	1	0.0332(45)			
8.265(5)	$\frac{1}{2}^-$	1	0.0582(52)			
8.410(6)	$\frac{5}{2}^+$	2	0.009(5)			
8.465(8)	$\frac{5}{2}^+$	2	0.009(1)			
8.509(3)	$\frac{5}{2}^+$	2	0.012(1)			
8.557(8)	$\frac{7}{2}^-$	3	0.009(1)			
8.602(4)	$\frac{7}{2}^-$	3	0.010(1)			
8.707(4)	$\frac{5}{2}^+$	2	0.025(1)			
8.764(8)	$\frac{5}{2}^+$	2	0.002(1)			
8.820(5)	$\frac{1}{2}^-$	1	0.0036(4)			
8.877(6)	$\frac{1}{2}^-$	1	0.0022(4)			
8.946(6)	$\frac{1}{2}^-$	1	0.0058(6)			
9.124(7)	$\frac{1}{2}^+$	0	0.052(6)			
9.182(4)	$\frac{1}{2}^+$	0	0.009(2)			

Continue on the next page

Table 10.2: (continued.).

Energy [MeV]	j^π	ℓ	C^2S	$C^2S_{(-1n)}$	j^π	ℓ
9.226(11)	$\frac{1}{2}^+$	0	0.002(1)			
9.291(11)	$\frac{3}{2}^-$	1	0.027(1)			
9.344(7)	$\frac{1}{2}^+$	0	0.002(1)			
9.395(5)	$\frac{3}{2}^-$	1	0.009(2)			
9.445(7)	$\frac{3}{2}^-$	1	0.002(1)			

- $\ell = 2, \frac{5}{2}^+$ hole states

The $d_{5/2}$ strength is significantly fragmented and the observed strength is distributed between 2.7-9 MeV excitation energy region. The highest $\frac{5}{2}^+$ hole state in ^{35}S was found to be at $E_x = 8.764$ MeV. The summed C^2S for the $d_{5/2}$ is 3.00 and the centroid is found at -14.93 MeV. This missing C^2S strength between ^{35}S (3.00) and ^{39}Ca (4.84) is currently not understood and is still being investigated. However it has been seen that there is a 20% increase in C^2S values for the $\frac{5}{2}^+$ states if the fitting range for the DWBA calculations is limited to 10-17°. As a consequence, for the time being, we will compare the centroids of $\frac{5}{2}^+$ in the two nuclei obtained when integrating the value up to the same excitation energy of 9 MeV.

- $\ell = 2, \frac{3}{2}^+$ hole states

In order to determine the $d_{3/2} - d_{5/2}$ spin-orbit splitting, the $d_{3/2}$ centroid has to be determined as well. In this work, it is observed that the $d_{3/2}$ hole strength is also fragmented. The largest fragment is the ground state with a C^2S value of 3.32 while the other fragments have much smaller C^2S values of 0.045 and less. There is indeed fragmentation, but it differs a lot from that of the $\frac{5}{2}^+$ states where none of them has a C^2S value greater than 0.8. The $d_{3/2}$ hole strength is spread between the 0-7 MeV excitation energy region. The C^2S summed weighted energy for the $d_{3/2}$ strength is 0.243 MeV.

Table 10.3: Summed C^2S , C^2S weighted mean energy and the binding energy $\langle \epsilon_j \rangle$ values in ^{35}S . The $p_{1/2}$ orbit was not included despite the fact that some $p_{1/2}$ strength is being observed, because of the need to maintain consistency with the analysis of the study of Matoba *et al.*, [1], whereby the $p_{1/2}$ orbit was excluded in the normalization.

Orbit	$\sum C^2S$	\bar{E} [MeV]	$\langle \epsilon_j \rangle$ [MeV]
$s_{1/2}$	2.10(24)	2.286	-12.18
$d_{3/2}$	3.41(40)	0.243	-10.13
$d_{5/2}$	3.00(34)	5.042	-14.93
$f_{7/2}$	0.291(37)	3.329	-6.651
$p_{3/2}$	0.144(12)	5.879	-4.011
$p_{1/2}$	0.164(22)	7.640	-2.250

- $\ell = 0, \frac{1}{2}^+$ hole states

An additional physics interest is to find the evolution of the binding energy of the $2s_{1/2}$ orbital. The C^2S weighted energy centroid value for the $\frac{1}{2}^+$ hole state was determined to be 2.286 MeV and the summed strength is close to the expected full occupancy at a value of 2.10.

10.3 Shell evolution in the $N = 19$ isotones

The fraction of $d_{3/2}$ strength present in the upper (valence) shells is deduced by:

$$R = \frac{\sum C^2S(\frac{3}{2}^-) + \sum C^2S(\frac{7}{2}^-)}{\sum C^2S(\frac{3}{2}^+) + \sum C^2S(\frac{3}{2}^-) + \sum C^2S(\frac{7}{2}^-)}, \quad (10.4)$$

and this is equivalent to 11.3 % for ^{35}S . Although small it is indicative of some $np - nh$ excitations into the upper shells. In ^{39}Ca we find a fraction equivalent to 11 %. There

is no evidence of a $\frac{1}{2}^+$ component in the $^{36}\text{S}(d,p)^{37}\text{S}$ neutron-adding experiment [41]. Therefore, the summed $C^2S = 0.33$ for the $\frac{3}{2}^+$ states can directly be compared to that of the $f_{7/2}$ and $p_{3/2}$ occupancy found from the $^{36}\text{S}(p,d)^{35}\text{S}$ reaction of 0.435. Again a good agreement. Taking that into account, the stiffness of the $N = 20$ shell closure can be compared between ^{40}Ca and ^{36}S . It can be deduced from the amount of occupancy of the upper shell. We are inclined to conclude that the $N = 20$ shell closure is a bit weaker in ^{36}S than ^{40}Ca , given the C^2S values of 0.435 and 0.408, respectively. However, the values are very comparable, and probably compatible considering the error bars on all C^2S values of weakly populated states.

The Δ_{SO}^d (spin-orbit) splitting which is the difference between the centroid energies of the 2 orbits is found to be $-10.13 - (-14.93) = 4.9$ MeV. Taking into consideration the usual spin orbit trend, it is expected that the spin orbit splitting in ^{35}S should be larger than that in ^{39}Ca . It unexpectedly goes in the opposite direction to the usual trend, whereby it is 4.9 MeV in ^{35}S and 6.2 MeV in ^{39}Ca , corresponding to a 1.3 MeV increase. A decrease in the spin-orbit splitting is expected due to the fact that the interaction between $d_{3/2}$ protons and $d_{5/2}$ neutrons is attractive. Therefore, as protons are removed from the $d_{3/2}$ orbital, the number of protons decreases, the spin-orbit splitting should become smaller.

10.3.1 Comparison between the (-1n) knockout and (p, d) transfer reactions.

Transfer and knockout reactions are a valuable tool to study the single-particle structure of nuclei. In as much as both reactions provide insightful information on the single particle structure of nuclei, the knockout reaction has some drawbacks. The knockout reaction using radioactive beams, as was done in the first part of this study, makes it possible to study the occupancy values for given orbits (within a certain framework)

for nuclei far away from stability. This is achieved by determining the branching of all states produced by the detection of the decaying γ -rays. In order to determine the partial cross sections associated with each populated state, it is required that the full level scheme be established, which may be hampered by the limited efficiency of γ -ray detection. It is also necessary to correct for the feeding of states from above. This creates large uncertainties for the determination of C^2S values for certain states. In particular, the uncertainty for the ground state is the largest, as it contains the feeding of all states that decay to it. In the case where a γ -ray is omitted then the C^2S is underestimated. Another challenge arises when an isomeric state is produced and the prompt γ decay is not observed. Assignments that are made in a knockout reaction are based on γ -gated momentum distributions, which is not possible for unbound states where neutron emission becomes the dominant decay channel.

The advantage of performing a transfer reaction with a high-resolution magnetic spectrometer, is that there is a unequivocal correspondence between the energy of a transferred particle and a state. In addition, since the identification of states from the transfer reaction is not dependent on detecting γ -rays, therefore, isomer states as well as states above the particle thresholds can be directly measured and accounted for. In order to probe the effectiveness of the closed shell from the occupancy of orbits that bind the $N=20$ gap ($d_{3/2}$, $f_{7/2}$, $p_{3/2}$), it is essential to obtain the C^2S values for the $d_{3/2}$, $f_{7/2}$ and $p_{3/2}$ orbits with sufficient accuracy. For this a transfer reaction was used to factor out the above-mentioned limitations that arise from using a knockout reaction and the associated γ -ray detection requirements.

From the knockout reaction ℓ values could be assigned to ten states at $E_x = 0, 1.572, 1991, 2.348, 2.717, 2.939, 3.421, 3.595, 3.818,$ and 4.025 MeV. These states were all observed in the (p, d) reaction together with many other states. The (p, d) reaction could however access higher excitation energies up to 11 MeV compared to the knockout reaction where at most the highest E_x reached was 6 MeV. The assignments made from

the (-1n) reaction are in agreement with those from the (p, d) reaction, except for the 3.886 MeV state, where the (p, d) reaction assigns $\ell = 3, \frac{7}{2}^-$ and the (-1n) reaction suggests a $\ell = 0, \frac{1}{2}^+$ assignment.

A comparison between the C^2S values for the knockout and (p, d) reaction is shown in Table 10.2. The ground state C^2S value of 3.32 from the (p, d) reaction is well within reasonable agreement with that of the knockout at $C^2S_{-1n} = (3.13)(72)$. The C^2S values for remaining states that are common between the two reactions are in agreement except for the 2.348 MeV and 3.886 MeV state. It is possible that for the 2.348 MeV state the discrepancy which is almost a factor of 10 ($C^2S_{(p,d)} = 0.036(4)$, $C^2S_{(-1n)}=0.32(1)$), could be due to the fact that generally the DWBA calculation does not reproduce well the measured angular distributions for the $p_{3/2}$ state. Therefore the C^2S is probably underestimated because of the poor fit. While the discrepancy in the C^2S value of the 3.886 MeV state ($C^2S_{(p,d)} = 0.018(2)$, $C^2S_{(-1n)}=0.23(3)$) is not understood and should be further investigated.

10.4 Ab-initio calculations

In the present work, a reduction in the neutron $d_{3/2} - d_{5/2}$ spin-orbit splitting has been observed based on experimental results as we remove 4 protons from ^{39}Ca to ^{35}S . Assuming a variation from the spin-orbit force only, a decrease of the $1d$ spin orbit splitting by about 460 keV [90] is expected between ^{39}Ca and ^{35}S . If a significant deviation to this trend is observed, this may be a manifestation of the tensor forces. The observed decrease in spin-orbit splitting can be used to test the predictability of mean field (MF), relativistic mean field (RMF) functionals and more generally to any model such as shell-model and ab-initio calculations.

Previous studies [91, 2] postulated that the reduction in splitting between spin-orbit partners, is indicative of the presence of a central depletion in the center of a light nucleus. This corresponds to the results shown Figure 10.1. What is particularly interesting is that for this case the effect is of pure spin-orbit origin as there is no tensor force when an $\ell = 0$ orbital is involved. Figures 10.1 and 10.3 show ab-initio calculations performed within the framework of the Gorkov Self-Consistent Green's functions (GSCGF) [92]. There are two types of interactions that have been used which are the next-to-next-to leading order (NNLO_{sat}) three body [93] and the next-to-next-to-next-to leading order (N3LO_{lnl}) [94, 95]. The NNLO_{sat} interaction includes the effect of the tensor force, takes into account a central depletion and reproduces the charge radii very well. It reproduces the experimental data well. The N3LO_{lnl} interaction includes a potential whose low-energy constants have been adjusted to fit the triton binding energy.

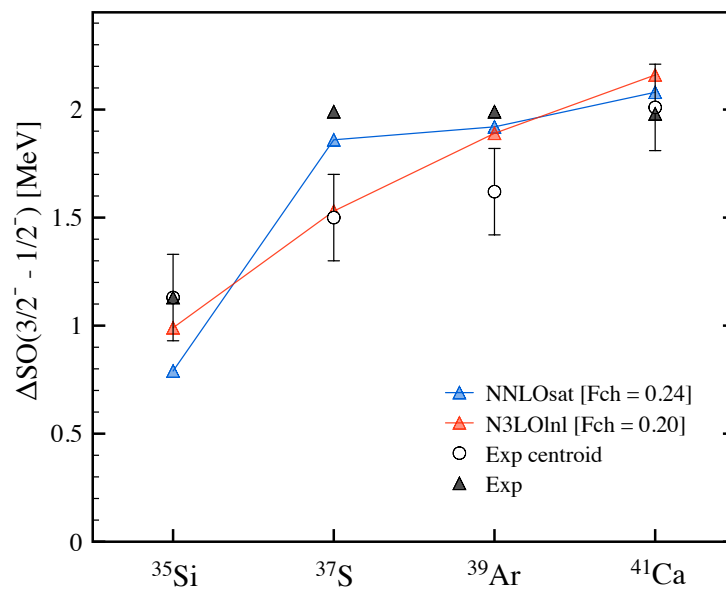


Figure 10.1: The sudden reduction of the neutron $2p_{3/2} - p_{1/2}$ spin-orbit splitting between ³⁷S and ³⁵Si, as protons are removed from the $2s_{1/2}$ orbital. The triangles represent the differences in energy between the $\frac{1}{2}^-$ and $\frac{3}{2}^-$ states having the largest C^2S value. The open circles were obtained by Kay et al., [96] who determined the differences of centroids obtained from transfer data.

Figure 10.3 summarizes the results for the $d_{5/2} - d_{3/2}$ spin orbit splitting. In general, a $j^\pi = \frac{3}{2}^+$ ground state is obtained with a high spectroscopic factor, around 75%. As was observed experimentally, likewise in all the nuclei, the $\frac{5}{2}^+$ state is fragmented, with several fragments associated with comparable spectroscopic strength. In Figure 10.3 it can be seen that in ^{35}S the strength is separated in two parts, with half of it at around 4 MeV. This is consistent with what is observed from experiment as indicated in Figure 10.2, where the two parts are around 3 and 6 MeV, compared to 4 and 5 MeV from the theory calculations. For ^{39}Ca , such a double component of the strength is observed as well but around 5.5 and 8 MeV.

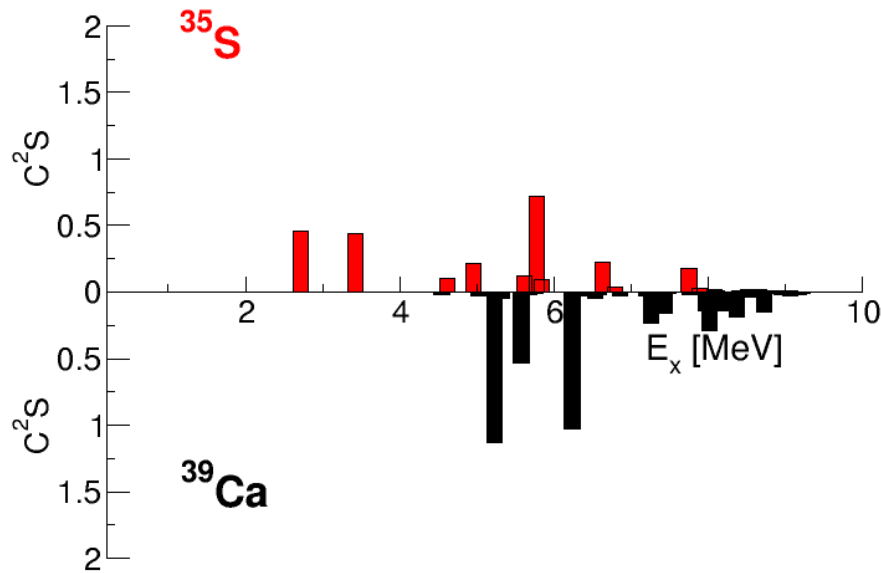


Figure 10.2: Illustration of the distribution of the $d_{5/2}$ hole strength in ^{35}S (red) and ^{39}Ca (black) as a function of excitation energy.

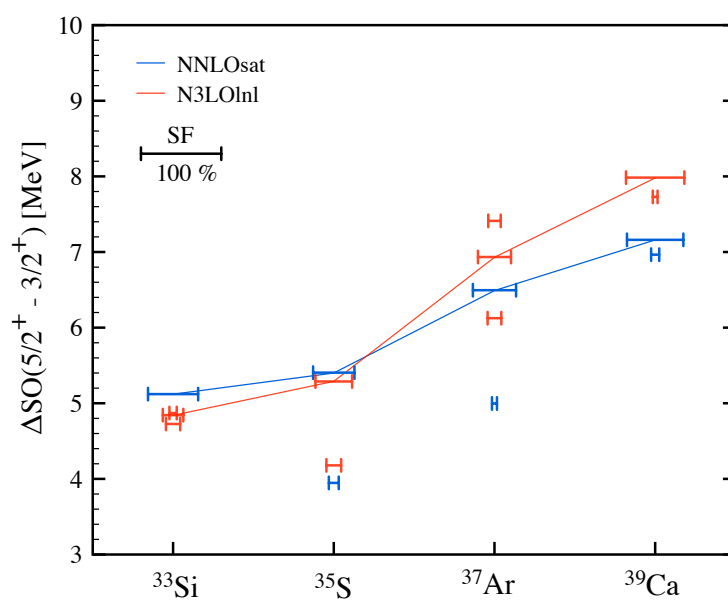


Figure 10.3: Predictions of the evolution of the $d_{5/2} - d_{3/2}$ splitting using ab-initio Gorkov Self-Consistent Green's functions [92]. The different fragmentation of the $d_{5/2}$ orbit is shown and the horizontal bars are indicative of the magnitude of the C^2S values.

10.5 N=20 Fermi surfaces

10.5.1 Fermi surface analysis from the $^{34}\text{Si}, ^{36}\text{S}(-1n)$ knockout reactions

Using the spectroscopic factors we are able to deduce the occupancy of the $s_{1/2}$ and $d_{3/2}$ orbitals using the relation [97]:

$$n_{j\pi} = \frac{1}{2j_{\pi} + 1} \sum_{i=j\pi} (C^2 S^{exp})_i. \quad (10.5)$$

The associated binding energies for the positive-parity orbitals are computed as indicated in equation 10.2:

The resulting occupancies and centroid binding energies are shown in Table 10.4 for the $^{34}\text{Si}(-1n)$ and $^{36}\text{S}(-1n)$ reactions in this work and in Table 10.5 from a previous study $^{34}\text{Si}(d, p)$ [2].

Table 10.4: Neutron occupations for the positive-parity orbitals obtained from the $^{34}\text{Si}(-1n)^{33}\text{Si}$ and $^{36}\text{S}(-1n)^{35}\text{S}$ reactions.

Nucleus	Orbital	E_x [MeV]	ℓ	$C^2 S_{exp}^{norm}$	$n_{j\pi}$ [%]	$\langle \epsilon_j \rangle$ [MeV]
^{34}Si	$s_{1/2}$	1.010	0	1.34(4)	67.0	-8.524
	$d_{3/2}$	0	2	3.90(42)	97.5	-7.514
^{36}S	$s_{1/2}$	1.572	0	1.26(25)	63.0	-12.99
		3.890	0	0.29(9)	14.5	
	$d_{3/2}$	0	2	3.33(76)	83.3	-10.80
		2.939	2	0.31(6)	15.5	

The spectroscopic factors obtained from the (d, p) transfer reactions on ^{35}Si and ^{37}S

Table 10.5: $^{34}\text{Si}(d,p)^{35}\text{Si}$ and $^{36}\text{S}(d,p)^{37}\text{S}$ reaction data obtained from Ref. [2].

Nucleus	Orbital	E_x [MeV]	L	C^2S_{exp}	$C^2S_{exp}^{norm}$	$n_{j\pi}$ [%]	$\langle \epsilon_j \rangle$ [MeV]
^{34}Si	$f_{7/2}$	0	3	0.56(6)	0.80(8)	20	-2.510
	$p_{3/2}$	0.910	1	0.69(10)	0.99(14)	1	-1.600
	$p_{1/2}$	2.040	1	0.73(10)	1.05(14)	0	-0.470
^{36}S	$f_{7/2}$	0	3	0.69(14)	0.99(20)	1	-4.303
	$p_{3/2}$	0.645	1	0.53(10)	0.76(14)	24	-3.655
	$p_{1/2}$	2.640	1	0.68(13)	0.97(18)	3	-1.660

Table 10.6: Neutron occupations for the negative-parity orbitals obtained from the $^{34}\text{Si}(-1n)^{33}\text{Si}$ and $^{36}\text{S}(-1n)^{35}\text{S}$ reactions.

Nucleus	Orbital	j^π	E_x [MeV]	C^2S_{exp}	$n_{j\pi}$ [%]
^{34}Si	$f_{7/2}$	$\frac{7}{2}^-$	1.435	0.72(43)	9
^{36}S	$f_{7/2}$	$\frac{7}{2}^-$	1.990	0.11(20)	1
			3.818	0.25(7)	3
^{36}S	$p_{3/2}$	$\frac{3}{2}^-$	2.348	0.34(1)	9

in the previous work of Burgunder *et al.*, [98], make it possible to obtain the centroid binding energies of the $f_{7/2}$, $p_{3/2}$ and $p_{1/2}$ orbitals. However, it was not possible to obtain the centroid binding energies for the negative-parity orbitals using the $^{34}\text{Si}(-1n)$ and $^{36}\text{S}(-1n)$ reactions. This is due to the fact that the $np - nh$ negative-parity states populated by knockout reactions are of complex configurations and are not single-hole or single particle, hence it is not possible to obtain the binding energies. However using the spectroscopic factor values obtained we were able to deduce the occupancy values of the $f_{7/2}$ and $p_{3/2}$ orbitals. The occupancy values for the "particle" type states populated from the (d,p) reactions were computed as follows:

$$n_{j\pi} = 1 - \sum_{i=j\pi} (C^2 S_{norm}^{(d,p)})_i. \quad (10.6)$$

It should be noted that the spectroscopic factors obtained from Ref. [98] do not include a systematic reduction factor of $R_s = 0.7$, hence the respective values were normalized using:

$$C^2 S_{norm}^{(d,p)} = \frac{C^2 S^{(d,p)}}{0.7}. \quad (10.7)$$

The systematics for the increasing body of reactions indicate a trend in R_s , the ratio of measured to theoretical inclusive cross sections. The suppressions observed indicate that the shell models used, plus the reaction model, overestimate the cross section (spectroscopic strength) leading to bound final states. The value of 0.7 used for the reduction factor is consistent with systematics for rare isotopes studied using ${}^9\text{Be}$ -target-induced knockout reactions [99].

10.5.1.1 Rigidity of N=20 shell gap

The Fermi surface plots obtained by incooperating the occupancy values from the ${}^{34}\text{Si}$, ${}^{36}\text{S}$ neutron knockout reactions are shown in Figure 10.4. The data points were fitted with the Bardeen–Cooper–Schrieffer (BCS) function [100]:

$$y = \frac{100}{2} \left(1 - \frac{x - \epsilon_f}{\sqrt{(x - \epsilon_f)^2 + \Delta^2}} \right). \quad (10.8)$$

where x refers to the excitation energies in the final nucleus, ϵ_f is the Fermi energy and

Δ represents the diffuseness parameter. The values of ϵ_f and Δ should be obtained as parameters resulting from fitting. For ^{34}Si we find $\epsilon_f = -5.14$ MeV and $\Delta = 2.55$ MeV. In ^{36}S $\epsilon_f = -8.32$ MeV and $\Delta = 3.18$ MeV. There is a conventional 20% error bar that is assumed which emanates from the use of optical potentials [101]. The error bar is not included in the Fermi surface plots because what is shown are relative occupation values and not absolute. The error bar being included would mean the slope of the Fermi surface plot can change completely. It would imply that the measurement is accurate to the extent that a maximum value for the binding energy can be deduced, which is not true. The Fermi energy and diffuseness should not change regardless of the choice of the optical model used. Comparing the Δ values in ^{34}Si and ^{36}S , it appears that ^{34}Si is more magic compared to ^{36}S .

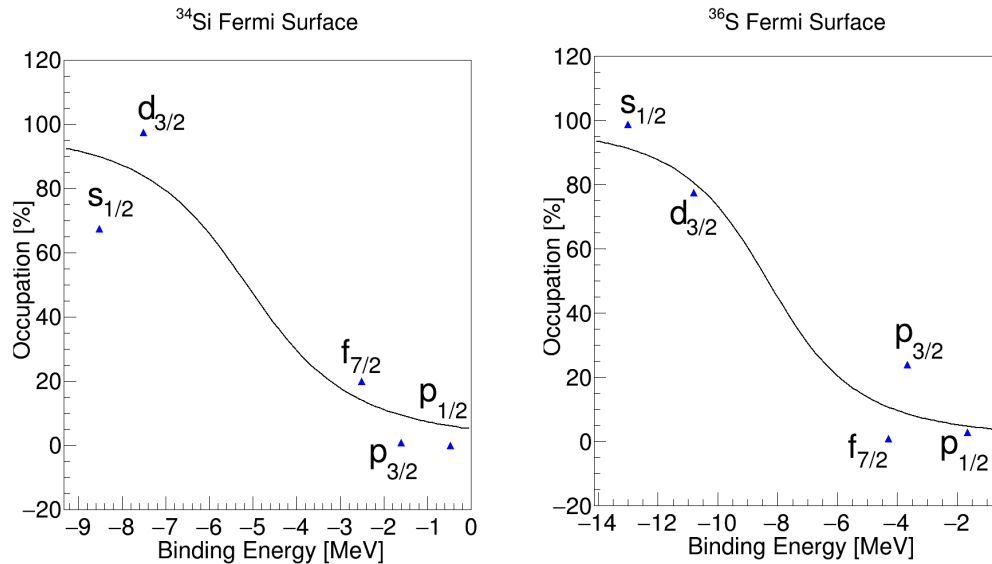


Figure 10.4: Fermi surface plot for neutron shells indicating occupation probabilities as a function of binding energies. From above: 1) Using combined data from the current work $^{34}\text{Si}(-1n)$ reaction with the $^{34}\text{Si}(d,p)$ reaction Ref. [2], 2) current work $^{36}\text{S}(-1n)$ reaction with the $^{36}\text{S}(d,p)$ reaction Ref. [2].

Through comparisons of the occupancy in the ^{34}Si , ^{36}S and ^{40}Ca we can deduce the difference in rigidity of the $N = 20$ shell gap and magicity of the nuclei. From the Fermi

surface analysis using the knockout reaction we compare ^{34}Si and ^{36}S . Both ^{34}Si and ^{36}S have similar diffuseness of the Fermi surface with occupancies of the negative-parity orbitals ($f_{7/2}, p_{3/2}$) as 9% and 13% respectively. However both these nuclei appear to be more magic compared to ^{40}Ca .

10.5.2 Fermi surface analysis from the ^{36}S , $^{40}\text{Ca}(p, d)$ reactions

In the analysis of the Fermi surface we used data points from both stripping (d, p) [25, 2] and pickup (p, d) reactions. For ^{36}S we find $\epsilon_f = -8.76$ MeV and $\Delta = 1.32$ MeV while in ^{40}Ca $\epsilon_f = -13.8$ MeV and $\Delta = 1.20$ MeV. Taking into account the diffuseness, ^{40}Ca appears to be slightly less magic compared to ^{36}S , however the values are very comparable. For both nuclei we find that the vacancy of the $d_{3/2}$ orbital is approximately equal to the occupancy of the fp states.

The ^{36}S Fermi surface deduced from the knockout reaction Figure 10.4 as compared to the one from the transfer reaction Figure 10.5 exhibit some differences. The former appears to have a more diffuse Fermi surface compared to the latter. This may be due to the different experimental techniques employed. In particular, the knockout reaction relies on γ -ray detection and as discussed in Section 10.3.1, the identification of weak γ -ray branches may affect the results.

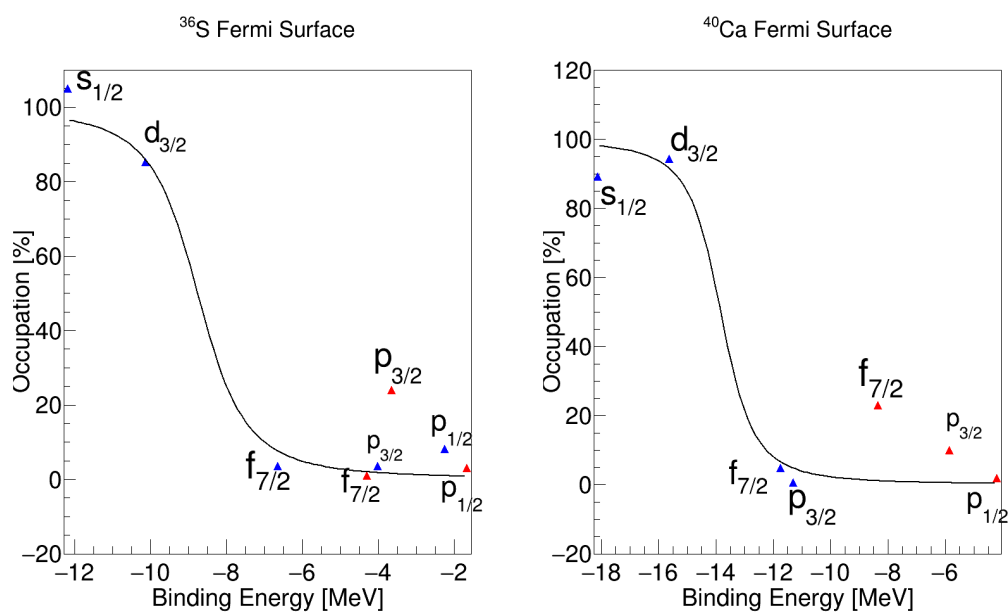


Figure 10.5: Fermi surface of ^{36}S neutrons (left) and ^{40}Ca neutrons (right). The data indicated in blue is from (p, d) reactions while the data indicated in red is from the (d, p) reaction. A general uncertainty (not shown) of 20% was assumed as explained in subsection 10.5.1.1.

11 | Conclusion

In the first part of this study we investigated the nuclear structure to understand the evolution of the $N = 20$ shell closure between ^{34}Si and ^{36}S . These aspects were explored using the $^9\text{Be}(^{36}\text{S}, ^{35}\text{S}+\gamma)\text{X}$ and $^9\text{Be}(^{34}\text{Si}, ^{33}\text{Si}+\gamma)\text{X}$ neutron knockout reactions performed at the NSCL facility with the GRETINA array coupled to the S800 spectrometer. The data were used to probe the Fermi surfaces of ^{34}Si and ^{36}S . Spectroscopic factors were extracted for the neutron single-particle orbits binding the $N = 20$ shell gap. In the knockout reaction, spectroscopic information was obtained by measuring γ rays using the GRETINA array in coincidence with particles detected in the S800 spectrometer. We were able to confirm spin assignments from the analysis of comparing experimental exclusive parallel momentum distribution to theoretical predictions within the framework of the Eikonal-model. The C^2S values of the ground states in ^{34}Si and ^{36}S are indicative of ^{34}Si having a larger $N=20$ shell gap than ^{36}S . This is consistent with the conclusion that ^{34}Si exhibits more magic behavior. However, it should be noted that the uncertainty for the ground state of ^{34}Si is too large to make such a conclusion with enough confidence.

The second part of this study focused on the evolution of the $d_{3/2}$ - $d_{5/2}$ spin orbit splitting between ^{36}S and ^{40}Ca . For this purpose a $^{36}\text{S}(p, d)^{35}\text{S}$ transfer reaction experiment was performed using the K600 spectrometer at the iThemba LABS facility. A novel

mechanical method of producing enriched ^{36}S targets was developed and the success of this method made it possible to perform the $^{36}\text{S}(p,d)^{35}\text{S}$ reaction. This method, which also proved to be cost effective, makes it possible to produce enriched ^{36}S for energetic light ion beam experiments using direct reaction measurements, also for future purposes. The (p,d) reaction was performed to overcome the limitations encountered with the knockout reactions and it allowed for the identification of states in ^{35}S up to an excitation energy of 11 MeV. In addition to identifying new states, spin-parity assignments were made to already known states. From the (p,d) reaction an interesting observation was noted whereby we found a clear j dependence of the experimental angular distributions. This ability was also confirmed by theoretical calculations. DWBA calculations were performed which were in turn used to compare with the experimental differential cross sections, allowing the assignment of spin and parities. The data from a previous $^{40}\text{Ca}(p,d)^{39}\text{Ca}$ experiment [1], was reanalyzed using the current DWBA calculations.

The centroid energies, summed C^2S values and C^2S weighted energies were obtained for ^{35}S and ^{39}Ca . The obtained results point to a significant increase in spin-orbit splitting as we move from ^{35}S to ^{39}Ca , which contradicts the expected trend. This observation was interpreted to be due to the effect of the tensor forces. The observed missing strength of the $d_{5/2}$ orbit in ^{35}S is not fully understood at the time of writing this document. There were no possible $\ell = 2$ states found at higher energies. In addition, the normalization procedure was confirmed by theorists within the collaboration who are performing and optimize DWBA calculations based on the results presented here. During the K600 experiment additional magnetic field settings were used to explore deep-hole states in the excitation energy regions between 14 and 23 MeV at two angle (7° and 15°). These measurements may now also be utilized to investigate the possible missing $d_{5/2}$ strength, however it is unlikely that the missing strength can be found at such high excitation energies. A Fermi surface analysis was also performed using the analysis from the (p,d) reactions, which suggest a strong $N = 20$ closure in ^{36}S compared to ^{40}Ca . It should be noted that the difference is not significant enough to make such a conclusion. Therefore,

in order to compare the shell closure there are in principle several factors that can be investigated such as the decrease in S_{2n} , from which the gap is usually derived, and the $B(E2)$ values. Despite this, it still remains that the information obtained from the transfer reaction is the most sensitive, because, the amplitude of the $N = 20$ shell gap can be derived in all isotones using the $\frac{3}{2}^+$ and $\frac{7}{2}^-$ centroids obtained from neutron-removal and neutron-adding information.

Appendices

A | Publications stemming from this study

A.1 Peer Reviewed Journal

The Structure of ^{33}Si and the magicity of the $N = 20$ gap at $Z = 14$. Jongile, S., Lemasson, A., Sorlin, O., Wiedeking, M., Papka, P., Bazin, D., Borcea, C., Borcea, R., Gade, A., Iwasaki, H. et al (2020) Physical Review C, 102 (2), 024321. <https://doi.org/10.1103/PhysRevC.102.024321>.

A.2 Conference proceeding

Encapsulated Sulfur targets for light ion beam experiments. Jongile, S. and Kheswa, N. and Papka, P. and Sorlin, O. and Lemasson, A. and Wiedeking, M. et al EPJ Web Conf. (2020). <https://doi.org/10.1051/epjconf/202022903004>.

Bibliography

- [1] M. Matoba, O. Iwamoto, Y. Uozumi, T. Sakae, N. Koori, T. Fujiki, H. Ohgaki, H. Ijiri, T. Maki, and M. Nakano, Phys. Rev. C **48**, 95 (1993), URL <https://link.aps.org/doi/10.1103/PhysRevC.48.95>.
- [2] G. Burgunder, O. Sorlin, F. Nowacki, S. Giron, F. Hammache, M. Moukaddam, N. de Séréville, D. Beaumel, L. Caceres, E. Clément, et al., Phys. Rev. Lett. **112**, 042502 (2014), URL <https://link.aps.org/doi/10.1103/PhysRevLett.112.042502>.
- [3] S. Jongile, N. Kheswa, P. Papka, O. Sorlin, A. Lemasson, and M. Wiedeking, EPJ Web Conf. **229** (2020), URL <https://doi.org/10.1051/epjconf/202022903004>.
- [4] E. Rutherford, The London, Edinburgh, and Dublin Philosophical Magazine and Journal of Science **21**, 669 (1911), URL <https://doi.org/10.1080/14786440508637080>.
- [5] J. Chadwick, Nature **192**, 312 (1932), URL <https://doi.org/10.1038/129798d0>.
- [6] R. B. Wiringa, V. G. J. Stoks, and R. Schiavilla, Phys. Rev. C **51**, 38 (1995), URL <https://link.aps.org/doi/10.1103/PhysRevC.51.38>.
- [7] B. Brown, Progress in Particle and Nuclear Physics **47**, 517 (2001),

- ISSN 0146-6410, URL <https://www.sciencedirect.com/science/article/pii/S0146641001001594>.
- [8] M. Bender, P. Heenen, and P. Reinhard, *Rev. Mod. Phys.* **75**, 121 (2003), URL <https://link.aps.org/doi/10.1103/RevModPhys.75.121>.
- [9] O. Sorlin and M.-G. Porquet, *Progress in Particle and Nuclear Physics* **61**, 602 (2008), ISSN 0146-6410, URL <http://www.sciencedirect.com/science/article/pii/S0146641008000380>.
- [10] *Lindau Nobel Laureate Meetings*, URL <https://www.mediatheque.lindau-nobel.org/research-profile/laureate-yukawa#page=4>.
- [11] *The nucleon-nucleon potential*, URL https://www.researchgate.net/figure/The-nucleon-nucleon-potential-At-distances-of-a-few-fermi-the-force-between-two_fig2_6617685/actions#reference.
- [12] K. Moghrabi, *The nucleon-nucleon interaction, Ph.D. Thesis, Univ. Paris XI* (2013).
- [13] C. M. G. Lattes, G. P. S. Occhialini, and C. F. Powell, *Nature* **160**, 486 (1947).
- [14] G. Breit and M. Hull, *Nuclear Physics* **15**, 216 (1960), URL <https://www.sciencedirect.com/science/article/pii/0029558260903035>.
- [15] A. Vértes, S. Nagy, Z. Klencsár, R. Lovas, and F. Rösch, *Handbook of Nuclear Chemistry* (Springer US, 2011), ISBN 9781441907219, URL <https://books.google.com.ec/books?id=FmYtnwEACAAJ>.
- [16] R. W. Ibbotson, T. Glasmacher, B. A. Brown, L. Chen, M. J. Chromik, P. D. Cottle, M. Fauerbach, K. W. Kemper, D. J. Morrissey, H. Scheit, et al., *Phys. Rev. Lett.* **80**, 2081 (1998), URL <https://link.aps.org/doi/10.1103/PhysRevLett.80.2081>.
- [17] T. Otsuka, T. Suzuki, R. Fujimoto, H. Grawe, and Y. Akaishi, *Phys. Rev. Lett.* **95**, 232502 (2005), URL <https://link.aps.org/doi/10.1103/PhysRevLett.95.232502>.

-
- [18] G. Mairle, Physics Letters B **304**, 39 (1993), ISSN 0370-2693, URL <https://www.sciencedirect.com/science/article/pii/0370269393913965>.
- [19] O. Sorlin, F. de Oliveira Santos, and J. Ebran, Physics Letters B **809**, 135740 (2020), ISSN 0370-2693, URL <https://www.sciencedirect.com/science/article/pii/S0370269320305438>.
- [20] K. L. Jones, Nature **465** (2010), ISSN 0370-2693, URL <https://doi.org/10.1038/nature09048>.
- [21] R. Orlandi, S. Pain, S. Ahn, A. Jungclaus, K. Schmitt, D. Bardayan, W. Catford, R. Chapman, K. Chipps, J. Cizewski, et al., Physics Letters B **785**, 615 (2018), ISSN 0370-2693, URL <https://www.sciencedirect.com/science/article/pii/S0370269318306087>.
- [22] J. Taprogge, A. Jungclaus, H. Grawe, S. Nishimura, P. Doornenbal, G. Lorusso, G. S. Simpson, P.-A. Söderström, T. Sumikama, Z. Y. Xu, et al., Phys. Rev. Lett. **112**, 132501 (2014), URL <https://link.aps.org/doi/10.1103/PhysRevLett.112.132501>.
- [23] A. Mutschler, *Le noyau-bulle de ^{34}Si :Un outil expérimental pour étudier l'interaction spin-orbite? Ph.D. Thesis, Univ. Paris XI* (2015).
- [24] R. Brun and F. Rademakers, Nuclear Instruments Methods in Physics Research Section Accelerators Spectrometers Detectors and Associated Equipment **389**, 81 (1997).
- [25] Y. Uozumi, Phys. Rev. C **50**, 263 (1994), URL <https://link.aps.org/doi/10.1103/PhysRevC.50.263>.
- [26] Y. Uozumi, O. Iwamoto, S. Widodo, A. Nohtomi, T. Sakae, M. Matoba, M. Nakano, T. Maki, and N. Koori, Nuclear Physics A **576**, 123 (1994), ISSN 0375-9474, URL <https://www.sciencedirect.com/science/article/pii/0375947494907404>.

-
- [27] J. Tostevin, Nuclear Physics A **682**, 320 (2001), ISSN 0375-9474, URL <http://www.sciencedirect.com/science/article/pii/S0375947400006564>.
- [28] R. Glauber, *Lectures in theoretical physics*, ed. WE Brittin and LG Dunham, vol. 1 (Interscience, New York, 1959).
- [29] D. Cortina, *Knockout reactions: experimental aspects*, Joliot-Curie School, France (2007).
- [30] C. Bertulani and A. Gade, Computer Physics Communications **175**, 372 (2006), ISSN 0010-4655, URL <https://www.sciencedirect.com/science/article/pii/S0010465506001937>.
- [31] B. A. Brown, *Lecture notes in nuclear structure physics*. (2010), URL <https://people.nsc.lmsu.edu/~brown/Jina-workshop/BAB-lecture-notes.pdf>.
- [32] A. Gade, P. Adrich, D. Bazin, M. D. Bowen, B. A. Brown, C. M. Campbell, J. M. Cook, T. Glasmacher, P. G. Hansen, K. Hosier, et al., Phys. Rev. C **77**, 044306 (2008), URL <https://link.aps.org/doi/10.1103/PhysRevC.77.044306>.
- [33] K. Wimmer, Journal of Physics G: Nuclear and Particle Physics **45**, 033002 (2018), URL <https://doi.org/10.1088%2F1361-6471%2Faaa2bf>.
- [34] M. G. Mayer, Phys. Rev. **74**, 235 (1948), URL <https://link.aps.org/doi/10.1103/PhysRev.74.235>.
- [35] M. G. Mayer, Phys. Rev. **75**, 1969 (1949), URL <https://link.aps.org/doi/10.1103/PhysRev.75.1969>.
- [36] O. Haxel, J. H. D. Jensen, and H. E. Suess, Phys. Rev. **75**, 1766 (1949), URL <https://link.aps.org/doi/10.1103/PhysRev.75.1766.2>.
- [37] K. L. G. Heyde, *The Nuclear Shell Model* (Springer Berlin Heidelberg, Berlin, Heidelberg, 1994), ISBN 978-3-642-79052-2, URL https://doi.org/10.1007/978-3-642-79052-2_4.

- [38] G. Potel, *Exotic Beam Summer School Lecture Notes* (2009).
- [39] I. J. Thompson and F. M. Nunes, *Nuclear Reactions for Astrophysics: Principles, Calculation and Applications of Low-Energy Reactions* (Cambridge University Press, 2009).
- [40] H. Paetz, *Nuclear Reactions: An Introduction. Lecture Notes in Physics, Springer, Berlin, Heidelberg* (2014).
- [41] ENSDF, *Evaluated Nuclear Structure Data File (ENSDF)*, URL <https://www.nndc.bnl.gov/ensdf>.
- [42] A. Stolz, Nuclear Instruments and Methods in Physics Research Section B: Beam Interactions with Materials and Atoms **241**, 858 (2005), ISSN 0168-583X, the Application of Accelerators in Research and Industry, URL <http://www.sciencedirect.com/science/article/pii/S0168583X0501339X>.
- [43] D. Morrissey, Nuclear Instruments and Methods in Physics Research Section B: Beam Interactions with Materials and Atoms **204**, 90 (2003), ISSN 0168-583X, 14th International Conference on Electromagnetic Isotope Separators and Techniques Related to their Applications, URL <http://www.sciencedirect.com/science/article/pii/S0168583X02018955>.
- [44] G. F. Knoll, *Radiation detection and measurement* (Wiley, 2000).
- [45] Z. Meisel, Phys. Rev. C **93**, 035805 (2016), URL <https://link.aps.org/doi/10.1103/PhysRevC.93.035805>.
- [46] D. Bazin, Nuclear Instruments and Methods in Physics Research Section B: Beam Interactions with Materials and Atoms **204**, 629 (2003), ISSN 0168-583X, URL <http://www.sciencedirect.com/science/article/pii/S0168583X02021420>.
- [47] J. Yurkon, D. Bazin, W. Benenson, D. Morrissey, B. Sherrill, D. Swan, and R. Swanson, Nuclear Instruments and Methods in Physics Research Section A: Accelerators, Spectrometers, Detectors and Associated Equipment **422**, 291 (1999),

- ISSN 0168-9002, URL <http://www.sciencedirect.com/science/article/pii/S0168900298009607>.
- [48] M. Berz and K. Joh, Phys. Rev. C **47**, 537 (1993), URL <https://link.aps.org/doi/10.1103/PhysRevC.47.537>.
- [49] S. Paschalis, I. Y. Lee, A. O. Macchiavelli, C. M. Campbell, M. Cromaz, S. Gros, J. Pavan, J. Qian, R. M. Clark, H. L. Crawford, et al., Nuclear Instruments and Methods in Physics Research Section A: Accelerators, Spectrometers, Detectors and Associated Equipment **709**, 44 (2013), ISSN 0168-9002, URL <https://www.sciencedirect.com/science/article/pii/S0168900213000508>.
- [50] *GRETINA Lawrence Berkeley National Laboratory*, URL <http://gretina.lbl.gov/>.
- [51] G. Schmid, M. Deleplanque, I. Lee, F. Stephens, K. Vetter, R. Clark, R. Diamond, P. Fallon, A. Macchiavelli, and R. MacLeod, Nuclear Instruments and Methods in Physics Research Section A: Accelerators, Spectrometers, Detectors and Associated Equipment **430**, 69 (1999), ISSN 0168-9002, URL <https://www.sciencedirect.com/science/article/pii/S0168900299001886>.
- [52] K. Wimmer, *GrRoot Data Analysis software package, NSCL S800 root data analysis, (unpublished)* (2013).
- [53] S. Agostinelli, J. Allison, K. Amako, J. Apostolakis, H. Araujo, P. Arce, M. Asai, D. Axen, S. Banerjee, G. Barrand, et al., Nuclear Instruments and Methods in Physics Research Section A: Accelerators, Spectrometers, Detectors and Associated Equipment **506**, 250 (2003), ISSN 0168-9002, URL <http://www.sciencedirect.com/science/article/pii/S0168900203013688>.
- [54] R. B. Firestone, *The 8th edition of the Table of Isotopes* (Springer, 1997).
- [55] D. Weisshaar, D. Bazin, P. Bender, C. Campbell, F. Recchia, V. Bader, T. Baugher, J. Belarge, M. Carpenter, H. Crawford, et al., Nuclear Instruments and Methods in

- Physics Research Section A: Accelerators, Spectrometers, Detectors and Associated Equipment **847**, 187 (2017), ISSN 0168-9002, URL <https://www.sciencedirect.com/science/article/pii/S0168900216312402>.
- [56] W. R. Leo, *Techniques for Nuclear and Particle Physics Experiments: A How-to Approach* (Springer-Verlag, 1994, 2nd Ed) (Springer-Verlag Berlin Heidelberg, 1994), URL <https://www.springer.com/gp/book/9783540572800>.
- [57] D. Weisshaar, D. Bazin, P. C. Bender, C. M. Campbell, F. Recchia, V. Bader, T. Baugher, J. Belarge, M. P. Carpenter, H. L. Crawford, et al., Nuclear Instruments and Methods in Physics Research. Section A, Accelerators, Spectrometers, Detectors and Associated Equipment **847** (2016), ISSN 0168-9002, URL <https://www.osti.gov/biblio/1372693>.
- [58] J. Enders, A. Bauer, D. Bazin, A. Bonaccorso, B. A. Brown, T. Glasmacher, P. G. Hansen, V. Maddalena, K. L. Miller, A. Navin, et al., Phys. Rev. C **65**, 034318 (2002), URL <https://link.aps.org/doi/10.1103/PhysRevC.65.034318>.
- [59] B. Fornal, Phys. Rev. C **49**, 2413 (1994), URL <https://link.aps.org/doi/10.1103/PhysRevC.49.2413>.
- [60] Z. M. Wang, R. Chapman, X. Liang, F. Haas, M. Bouhelal, F. Azaiez, B. R. Behera, M. Burns, E. Caurier, L. Corradi, et al., Phys. Rev. C **81**, 064301 (2010), URL <https://link.aps.org/doi/10.1103/PhysRevC.81.064301>.
- [61] A. Morton, P. Mantica, B. Brown, A. Davies, D. Groh, P. Hosmer, S. Liddick, J. Prisciandaro, H. Schatz, M. Steiner, et al., Physics Letters B **544**, 274 (2002), ISSN 0370-2693, URL <http://www.sciencedirect.com/science/article/pii/S0370269302025443>.
- [62] L. Fifield, Nuclear Physics A **440**, 531 (1985), ISSN 0375-9474, URL <http://www.sciencedirect.com/science/article/pii/0375947485902441>.

-
- [63] L. Fifield, Nuclear Physics A **453**, 497 (1986), ISSN 0375-9474, URL <http://www.sciencedirect.com/science/article/pii/0375947486904495>.
- [64] Z. M. Wang, Phys. Rev. C **81**, 064301 (2010), URL <https://link.aps.org/doi/10.1103/PhysRevC.81.064301>.
- [65] S. R. Stroberg, A. Gade, J. A. Tostevin, V. M. Bader, T. Baugher, D. Bazin, J. S. Berryman, B. A. Brown, C. M. Campbell, K. W. Kemper, et al., Phys. Rev. C **90**, 034301 (2014), URL <https://link.aps.org/doi/10.1103/PhysRevC.90.034301>.
- [66] J. Enders, Phys. Rev. C **67**, 064301 (2003), URL <https://link.aps.org/doi/10.1103/PhysRevC.67.064301>.
- [67] E. K. Warburton, J. A. Becker, and B. A. Brown, Phys. Rev. C **41**, 1147 (1990), URL <https://link.aps.org/doi/10.1103/PhysRevC.41.1147>.
- [68] E. K. Warburton, J. W. Olness, G. A. P. Engelbertink, and T. K. Alexander, Phys. Rev. C **7**, 1120 (1973), URL <https://link.aps.org/doi/10.1103/PhysRevC.7.1120>.
- [69] S. Raman, R. F. Carlton, J. C. Wells, E. T. Journey, and J. E. Lynn, Phys. Rev. C **32**, 18 (1985), URL <https://link.aps.org/doi/10.1103/PhysRevC.32.18>.
- [70] R. Abegg and S. Datta, Nuclear Physics A **287**, 94 (1977), ISSN 0375-9474, URL <https://www.sciencedirect.com/science/article/pii/0375947477905656>.
- [71] C. Moss, Nuclear Physics A **131**, 235 (1969), ISSN 0375-9474, URL <http://www.sciencedirect.com/science/article/pii/0375947469908215>.
- [72] R. Freeman, R. Faerber, M. Toulemonde, and A. Gallmann, Nuclear Physics A **197**, 529 (1972), ISSN 0375-9474, URL <http://www.sciencedirect.com/science/article/pii/0375947472910275>.
- [73] A. Guichard, H. Nann, and B. H. Wildenthal, Phys. Rev. C **12**, 1109 (1975), URL <https://link.aps.org/doi/10.1103/PhysRevC.12.1109>.

-
- [74] R. Neveling, H. Fujita, F. Smit, and T. Adachi, Nuclear Instruments and Methods in Physics Research Section A: Accelerators, Spectrometers, Detectors and Associated Equipment **654**, 29 (2011), ISSN 0168-9002, URL <https://www.sciencedirect.com/science/article/pii/S0168900211012460>.
- [75] A. H. Botha, H. Jungwirth, F. Smit, and T. Adachi, Proceedings of the 10th International Conference on Cyclotrons and their Applications, Michigan, IEEE, New York p. 263 (1984).
- [76] R. Neveling, F. D. Smit, H. Fujita, and R. T. Newman, *A Guide to the K600 Magnetic Spectrometer*, unpublished (2011).
- [77] T. Wakasa, G. Berg, H. Fujita, Y. Fujita, K. Hatanaka, K. Hara, M. Itoh, J. Kamiya, T. Kawabata, K. Nagayama, et al., Nuclear Physics A **721**, C1099 (2003), ISSN 0375-9474, URL <https://www.sciencedirect.com/science/article/pii/S0375947403012946>.
- [78] L. Fifield and N. Orr, Nuclear Instruments and Methods in Physics Research Section A: Accelerators, Spectrometers, Detectors and Associated Equipment **288**, 360 (1990), ISSN 0168-9002, URL <http://www.sciencedirect.com/science/article/pii/016890029090125P>.
- [79] M. Mayer, AIP Conference Proceedings **475** (1999).
- [80] J. F. Ziegler, M. D. Ziegler, and J. P. Biersack, Nuclear Instruments and Methods in Physics Research B **268**, 1818 (2010).
- [81] C. Wheldon, *Derivations for two-body kinematics (both relativistic and non-relativistic (unpublished))* (2014).
- [82] L. D. Landau, J. Phys. **8**, 201 (1944), URL <https://cds.cern.ch/record/216256>.
- [83] G. R. Satchler, *Introduction to nuclear reactions. the macmillan press ltd.* (1980).

-
- [84] R. L. Kozub, Phys. Rev. **172**, 1078 (1968), URL <https://link.aps.org/doi/10.1103/PhysRev.172.1078>.
- [85] I. J. Thompson, Computer Physics Reports **7**, 167 (1988), ISSN 0167-7977, URL <https://www.sciencedirect.com/science/article/pii/0167797788900056>.
- [86] J. J. H. Menet, E. E. Gross, J. J. Malanify, and A. Zucker, Phys. Rev. C **4**, 1114 (1971), URL <https://link.aps.org/doi/10.1103/PhysRevC.4.1114>.
- [87] R. C. Johnson and P. J. R. Soper, Phys. Rev. C **1**, 976 (1970), URL <https://link.aps.org/doi/10.1103/PhysRevC.1.976>.
- [88] F. D. Becchetti and G. W. Greenlees, Phys. Rev. **182**, 1190 (1969), URL <https://link.aps.org/doi/10.1103/PhysRev.182.1190>.
- [89] F. Eckle, H. Lenske, G. Eckle, G. Graw, R. Hertenberg, H. Kader, H. Maier, F. Merz, H. Nann, P. Schiemenz, et al., Nuclear Physics A **506**, 159 (1990), ISSN 0375-9474, URL <https://www.sciencedirect.com/science/article/pii/037594749090382V>.
- [90] G. Mairle, Physics Letters B **304**, 39 (1993), ISSN 0370-2693, URL <https://www.sciencedirect.com/science/article/pii/0370269393913965>.
- [91] A. Mutschler, A. Lemasson, O. Sorlin, D. Bazin, C. Borcea, R. Borcea, Z. Dombrádi, J. P. Ebran, A. Gade, H. Iwasaki, et al., Nature Physics **13**, 152 (2017), URL <https://doi.org/10.1038/nphys3916>.
- [92] V. Somà, T. Duguet, and C. Barbieri, Phys. Rev. C **84**, 064317 (2011), URL <https://link.aps.org/doi/10.1103/PhysRevC.84.064317>.
- [93] A. Ekström, G. R. Jansen, K. A. Wendt, G. Hagen, T. Papenbrock, B. D. Carlsson, C. Forssén, M. Hjorth-Jensen, P. Navrátil, and W. Nazarewicz, Phys. Rev. C **91**, 051301 (2015), URL <https://link.aps.org/doi/10.1103/PhysRevC.91.051301>.

-
- [94] D. R. Entem and R. Machleidt, Phys. Rev. C **68**, 041001 (2003), URL <https://link.aps.org/doi/10.1103/PhysRevC.68.041001>.
- [95] R. Roth, S. Binder, K. Vobig, A. Calci, J. Langhammer, and P. Navrátil, Phys. Rev. Lett. **109**, 052501 (2012), URL <https://link.aps.org/doi/10.1103/PhysRevLett.109.052501>.
- [96] B. P. Kay, C. R. Hoffman, and A. O. Macchiavelli, Phys. Rev. Lett. **119**, 182502 (2017), URL <https://link.aps.org/doi/10.1103/PhysRevLett.119.182502>.
- [97] E. Khan, Nuclear Physics A **800**, 37 (2008), ISSN 0375-9474, URL <http://www.sciencedirect.com/science/article/pii/S0375947407008020>.
- [98] G. Burgunder, *Étude de l'interaction nucléaire spin-orbite par réactions de transfert $^{36}\text{S}(d,p)^{37}\text{S}$ et $^{34}\text{Si}(d,p)^{35}\text{Si}$* , University of Caen Normandy Ph.D. Thesis (2012).
- [99] J. A. Tostevin and A. Gade, Phys. Rev. C **90**, 057602 (2014), URL <https://link.aps.org/doi/10.1103/PhysRevC.90.057602>.
- [100] J. Bardeen, L. N. Cooper, and J. R. Schrieffer, Phys. Rev. **108**, 1175 (1957), URL <https://link.aps.org/doi/10.1103/PhysRev.108.1175>.
- [101] O. Sorlin, *Private communication* (2018).